DEVELOPMENT AND EVALUATION OF ALTERNATIVE METHODS FOR FUNCTIONAL MAGNETIC RESONANCE IMAGING AT 7 TESLA

By

JOHN ANDREW SEXTON

Dissertation

Submitted to the Faculty of the

Graduate School of Vanderbilt University

in partial fulfillment of the requirements

for the degree of

DOCTOR OF PHILOSOPHY

in

Biomedical Engineering

May, 2010

Nashville, TN

Approved

John C. Gore

J. Christopher Gatenby

Adam W. Anderson

Rene M. Marois

Victoria L. Morgan

ACKNOWLEDGEMENTS

Many individuals in both my professional and personal life have played a significant role in my graduate school experience. I would like to first thank my academic advisor, Dr. John Gore, who has consistently helped me to see the big picture and pushed me toward the most relevant areas of study. He has taught me to be more precise writer, a more disciplined thinker, and a better problem solver. He has always been understanding and supportive in personal matters, and was especially gracious in allowing me to finish my dissertation remotely so I could start a life with my fiance in Richmond, Virginia.

Next I thank Dr. Chris Gatenby, who has kindly answered my many questions and emails and who has given me invaluable hands-on experience in operating the 3T and 7T scanners. Dr. Gatenby has often helped me to think carefully about the details of my work and has patiently offered numerous explanations -- and sometimes the same ones over and over -- when I needed it.

In addition, I wish to acknowledge Victoria Morgan, Adam Anderson, Rene Marois as other members of my Ph.D. committee who have provided insightful feedback on my experiments, this dissertation, and everything in between. They have diligently responded to my emails and have been friendly and accommodating when I gather them into a room to listen to me talk for an hour.

Many other colleagues have played important roles in my development at Vanderbilt. Baxter Rogers in particular has been a constant and reliable source of information, feedback, and camaraderie. I think he also appreciated my

enthusiasm for using Basecamp, which helped me to feel less like a productivity-software-obsessed weirdo. Brian Welch has often come to me with new ideas and has even helped me to make professional connections. Brian has been patient and has given generously of his time.

Though I only started working with Jascha Swisher toward the end of my time at Vanderbilt, he has been a great colleague. He was indispensable in completing the retinotopic mapping studies which became Chapter V of this work, and provided me with a wealth of information on that topic. He also generated the retinotopic maps that appear in Chapter V. Other notable colleagues include Robert Barry and Allen Newton, both of whom have been quite helpful in both administrative and scientific matters.

I further thank Nancy Hagans for providing answers to my administrative questions, and Robin Avison for keeping life exciting at the scanner.

On a personal level, my parents have always encouraged me persevere and to do my best, even when it meant extra work or taking extra time. They have been with me every step of the way on my academic and personal development, and I want them to know that I never would have made it this far without their support and understanding.

I want to give special thanks to my fiance, Mandy Butler. To say she has been patient with me through this process would be like saying the body contains a few water molecules. She has lifted my spirits when I was overwhelmed, forced me to take breaks when I needed to, and has made me be a better person by providing valuable perspective on matters of life, work, and family. She has also

introduced me to the two greatest animals in the world, Oliver Pupfriend and PajamasCat, who have kept my feet warm and the mood light. I am proud to have the opportunity to see Mandy pursue her own passion in graduate school today.

Finally, I acknowledge the National Science Foundation, from which I was fortunate enough to receive the Graduate Research Fellowship award to fund my first three years of graduate school, and the National Institute of Health, which provided grant R01EB00461 which funded the experiments presented here as well as the remainder of my time at Vanderbilt.

TABLE OF CONTENTS

LIST OF TABLES

Page

LIST OF FIGURES

Page

CHAPTER I

INTRODUCTION

If Paul Lauterbur had listened to the editors of *Nature*, magnetic resonance imaging (MRI) as it is known today might never have developed. Initially rejected because it lacked "wide significance," Lauterbur's two-page manuscript describing a method for spatially localizing the nuclear magnetic resonance (NMR) signal with magnetic field gradients was reviewed again at Lauterbur's request and was eventually published on March 16th, 1973. In November of that year, Peter Mansfield provided the mathematical formalism for the gradient encoding technique (Mansfield and Grannell, 1973). Two years later, Richard Ernst applied the Fourier transform to convert gradient encoded NMR signals into two dimensional images (Kumar et al., 1975). Now, just over thirty years since its formal introduction, magnetic resonance imaging has become one of the most powerful and flexible medical imaging techniques available.

The NMR phenomenon had originally been studied in chemistry and physics, with research progressing steadily over the preceding half-century. Key experiments included Stern and Gerlach's initial demonstration that atoms possessed intrinsic magnetic fields (1924), Isador Rabi's measurements of the NMR properties of atomic and molecular beams (1938), Bloch and Purcell's independent measurements of the NMR properties of water and paraffin (1946), and Raymond Damadian's discovery that cancerous tissues had different NMR

relaxation properties than normal tissues (1971). Clearly, the field of NMR was alive and well prior to the innovations of Lauterbur, Mansfield, and Ernst. Still, it was the combination of gradient encoding and the Fourier transform that sparked the critical transition from research tool to revolutionary imaging technique[1].

Though MRI technology has advanced tremendously, most MR images created today are obtained with the same gradient encoding and Fourier transform principles proposed in the 1970s. By varying the strength, direction, and duration of weak, linear magnetic field gradients in combination with pulses of radio frequency (RF) energy and a strong, uniform main magnetic field, MRI scanners can produce images in any orientation, at spatial resolutions on the order of 1 x 1 x 1mm^3, and with a variety of contrast mechanisms. MRI is non-invasive, and does not require ionizing radiation or radioactive tracers like many other medical imaging techniques. In most cases MRI utilizes only the magnetic properties of the hydrogen nucleus, found in abundance in the water molecules which comprise the human body. Though MRI excels at measuring soft tissue contrast in the brain, the technique is also capable of imaging any anatomic location containing mobile hydrogen nuclei.

Despite its proliferation, the field of magnetic resonance imaging is still quite young and continues to experience rapid development. Three major topics discussed in this dissertation, functional MRI (fMRI), human imaging at high

[1] For their contributions to what would become this broad and thriving discipline, the Nobel Prize for physics was awarded to Stern in 1943, to Rabi in 1944, and jointly to Bloch and Purcell in 1952. Ernst received the Nobel Prize in Chemistry in 1991, and Lauterbur and Mansfield jointly received the Nobel Prize for physiology and medicine in 2003.

magnetic field strengths, and parallel imaging, have been introduced only within the past two decades.

In 1990, Ogawa et al. showed that blood with varying levels of oxygen content modulated contrast in MR images. Though the relationship between blood oxygenation and NMR relaxation time had been studied previously (e.g., Thulborn et al., 1982), the 1990 Ogawa et al. study is often cited as a foundational work in blood-oxygen-level dependent (BOLD) contrast. BOLD contrast relies on differences in magnetic susceptibility between oxygenated and deoxygenated hemoglobin to measure brain activity in response to simple stimuli, and is the basis of most functional MRI (fMRI) experiments.

fMRI methods have remained largely unchanged since the technique was introduced. Generally a series of relatively low resolution (3 x 3 x 3mm^3) images sensitive to small changes in the intra-voxel variations of magnetic susceptibility (T_2*-weighted) are collected in rapid succession with single-shot, gradient echo echo planar imaging (2D-EPI). This method generally provides high BOLD contrast, high signal-to-noise efficiency, high temporal resolution, and good signal stability (Bandettini, 2007).

Most functional MRI experiments have been performed at magnetic field strengths of 1.5 or 3.0 Tesla (T) and produce generally reliable, if low resolution, results. Within the past ten years, human MRI scanners with field strengths of 7T and above have become available for research. Because both the NMR signal-to-noise ratio (SNR) and BOLD contrast increase at least linearly with field

strength, there has been great interest in leveraging these improvements to image brain function at higher resolutions and with greater sensitivity.

Unfortunately, high field strengths also increase bulk magnetic susceptibility effects which create a number of problems in 2D-EPI images; these include image distortion, which leads to errors in localization of the functional MRI signal to the underlying anatomy; signal loss, which reduces BOLD sensitivity; and blurring, which limits the spatial resolution of activation maps. Also increased are signal fluctuations from physiological processes such as respiration, RF pulse inhomogeneity, and patient safety and comfort concerns (Vaughan et al., 2001; Norris, 2003). These difficulties have thus far limited the practical benefits of high field fMRI with echo planar imaging; therefore much of this dissertation focuses on alternative methods for high field fMRI.

An important recent development in MRI technology is data acquisition with multiple receiver coils in parallel. Parallel imaging methods no longer rely exclusively on gradient fields for encoding of the NMR signal; instead, signal information is partially encoded using the spatially varying reception profiles of the signal detector coils themselves (Pruessmann et al., 1999). The result is accelerated data acquisition and a fundamental shift in MRI methods. Parallel imaging performance improves as field strength and the number of receiver coils increase (Pruessmann et al., 1999; Wiesinger et al., 2004).

Several of the issues that limit high field fMRI performance can be addressed with parallel imaging. In particular, accelerated data acquisition can reduce distortion, blurring, and signal loss in 2D-EPI, increase spatial resolution,

or reduce other unwanted effects such as gradient acoustic noise (de Zwart et al., 2006). Parallel imaging can also reduce the total scan time, meaning some scan archetypes which had previously been too slow or SNR-inefficient to compete with 2D-EPI for fMRI may become viable alternatives. Two such sequences, mult-shot, gradient echo 3D-Fast Field Echo (FFE) and multi-shot, gradient echo 3D-PRESTO (Principles of Echo Shifting with a Train of Observations) are studied here (Liu et al., 1993).

Acceleration with parallel imaging comes at the price of a spatially varying and reduced signal-to-noise ratio which depends on the degree of acceleration and other coil array and scan-specific factors (Pruessmann et al., 1999). The full extent of these penalties on fMRI sensitivity is not yet understood, but appears to depend on the relative contributions of physiological noise to the total signal variance over time (Triantafyllou et al., 2005; de Zwart et al., 2006).

Specific Aims

High magnetic field strengths and parallel imaging methods each offer unique advantages and drawbacks to functional MRI. This dissertation aims to critically examine how these features interact, to evaluate specific imaging sequences that take advantage of the theoretical benefits of functional imaging at 7T, and to develop guidelines for optimizing high resolution fMRI acquisitions in the context of parallel imaging at high field. The specific aims of this work are:

8) to describe quantitatively the interactions between parallel imaging, physiological noise, temporal signal stability and fMRI sensitivity at high field;

9) to quantify the noise enhancement related to parallel imaging for specific 2D and 3D imaging conditions in order to choose optimal acceleration factors and imaging parameters for specific imaging applications;

10) to identify optimal sets of acquisition parameters for high field fMRI experiments in both high-resolution, limited coverage and low resolution, full brain coverage applications;

11) to evaluate the performances of optimized versions of three imaging sequences (2D-EPI, 3D-FFE, and 3D-PRESTO) at multiple resolutions in a retinotopic mapping task at high field;

12) to integrate the findings from aims 1 - 4 to develop a general approach for optimizing high field fMRI acquisitions with parallel imaging.

With these aims in mind, the dissertation is organized as follows:

CHAPTER II: Background

Previous relevant work and background information area presented which are essential for the materials presented in chapters III, IV, and V.

CHAPTER III: Effects of Sensitivity Encoding on Temporal Signal Stability and fMRI at 7T

The relationships between parallel imaging, magnetic susceptibility effects, and physiological noise are explored and quantified in a simple, high resolution fMRI task with 2D-EPI at 7T.

CHAPTER IV: Optimization of Sensitivity Encoded Acquisitions for fMRI at 7T

The relationships between noise enhancement related to parallel imaging, receiver coil array geometry, field of view, and other scan parameters are explored and quantified in 2D-EPI, 3D-FFE, and 3D-PRESTO. Acquisition parameters optimized for high-resolution, limited field of view, as well as low-resolution, full-coverage fMRI applications are identified.

CHAPTER V: Comparison of Imaging Sequences for fMRI at 7T

The performance of sequences developed in chapter IV is compared at four resolutions (1.12 x 1.12 x 1.12mm^3, 1.67 x 1.67 x 1.67mm^3, 2 x 2 x 2mm^3, and 3 x 3 x 3mm^3) in a retinotopic mapping study at 7T, and conclusions are drawn about the relative merits of different approaches.

CHAPTER VI: Summary and Outlook

Findings from Chapters III, IV, and V are reviewed and integrated to develop a procedure for choosing optimal acquisition parameters in fMRI experiments at 7T. Future directions are also suggested.

CHAPTER II

BACKGROUND

1. Overview

This chapter reviews the basic physics, concepts, and methods upon which the original work in this dissertation is based. Specifically, we describe the following: (1) nuclear magnetic resonance and the associated signal; (2) spatial encoding of the NMR signal for magnetic resonance imaging; (3) 2D and 3D gradient echo imaging sequences and their relative strengths and weaknesses; (4) off-resonance effects such as distortion and signal loss; (5) the spatial and temporal signal-to-noise ratios; (6) image characteristics including spatial resolution and contrast; (7) functional magnetic resonance imaging principles and methods; and (8) parallel imaging techniques. Each topic is discussed both in general and with respect to high magnetic field strengths.

2. Nuclear Magnetic Resonance

2.1. Spin Angular Momentum and the Magnetic Dipole Moment

In addition to mass and charge, sub-atomic particles (protons, neutrons, and electrons) posses spin angular momentum ($\boldsymbol{J}$) and a magnetic dipole moment ($\boldsymbol{\mu}$), defined as follows:

$$\boldsymbol{J} = \hbar \boldsymbol{I} \tag{2.1}$$

$$\boldsymbol{\mu} = \gamma \boldsymbol{J} \tag{2.2}$$

Where $\hbar$ is Planck's constant[2], γ is the nucleus-specific gyromagnetic ratio[3], and $\boldsymbol{I}$ is the atom-specific spin quantum number. Particles of the same kind tend to form pairs of opposing spin direction. Atomic nuclei with an even number of both types of nucleons (protons and/or neutrons), (e.g. $^{12}_{6}$C) form complete pairings and therefore have no net spin and no net magnetic moment. Nuclei with an odd number of a given type of nucleon (e.g. $^{1}_{1}$H, $^{2}_{1}$H, $^{13}_{6}$C) form incomplete pairs and therefore possess net $\boldsymbol{J}$ and $\boldsymbol{\mu}$.

The magnetic moment offers a means by which to detect and to interact with spins. If a spin is placed in a magnetic field pointing in the z-direction ($\boldsymbol{B} = B_0\,\hat{z}$), possible values of the *z*-component of its angular momentum are

$$J_z = \hbar\, m_{\boldsymbol{I}} \tag{2.3}$$

where $m_{\boldsymbol{I}} = \boldsymbol{I}, (\boldsymbol{I}-1), (\boldsymbol{I}-2), ..., -\boldsymbol{I}$ has a total of $2\,\boldsymbol{I}+1$ values. For an atom with given $\boldsymbol{J}$, the energy of a magnetic moment $\boldsymbol{\mu}$ in an applied field $\boldsymbol{B}$ is:

$$E = -\boldsymbol{\mu}\cdot\boldsymbol{B} \tag{2.4}$$

The single-proton Hydrogen nucleus ($\boldsymbol{I} = \frac{1}{2}$) is of interest in NMR because of its natural abundance and large magnetic moment. In the presence of an

---

[2] Planck's Constant: $\hbar$ = 1.055 x 10^{-34} Joule-seconds.

[3] For Hydrogen, γ = 2.675 x 10^{8} radians per second per Tesla, or 2 π x 4.26 kHz / Gauss.

applied field $\boldsymbol{B} = B_0\,\hat{z}$, the Hydrogen nucleus has two possible values of J_z, and therefore two possible values of E:

$$J_z = \pm\tfrac{1}{2}\,\hbar \tag{2.5}$$

$$E = \pm\,\tfrac{1}{2}\,\hbar\,\gamma\,B_0 \tag{2.6}$$

Spins aligned parallel to and antiparallel to the field occupy the lower and higher energy states, respectively. A transition between the two represents a change in energy:

$$\Delta E = E(m_{\boldsymbol{I}} = -\frac{1}{2}) - E(m_{\boldsymbol{I}} = +\frac{1}{2})) \tag{2.7.1}$$

$$= \quad \frac{1}{2}\,\gamma\,\hbar\,B_0 - (-\frac{1}{2}\,\gamma\,\hbar\,B_0) \tag{2.7.2}$$

$$= \quad \gamma\,\hbar\,B_0 \tag{2.7.3}$$

$$= \quad \hbar\,\omega_0 \tag{2.7.4}$$

Where

$$\omega_0 = \gamma B_0 \tag{2.8}$$

This is the Larmor Equation, a central relation of NMR. In particular, ω_0 is the Larmor frequency, the precise frequency of electromagnetic energy that must be absorbed or emitted for a spin to transition energy states in the presence of

B_0. By Eq. 2.8, larger magnetic fields yield larger energy differences and higher resonance frequencies.

2.2. Net Magnetization

In the context of imaging, it is intuitive to consider the net Magnetization (M), which measures the magnetic moment per unit volume of many spins. In the absence of an external field, thermal activity and internal dipole fields orient spins randomly, yielding a zero net magnetization. When a uniform magnetic field is applied, about half of the spins in an ensemble align antiparallel to the field, while a tiny majority[4] align parallel to it in the preferred lower energy state. The result is non-zero M aligned parallel to the field.

The angular momentum of spins which comprise M cause precessional motion of the net magnetization vector about the applied field. This motion is described by the torque between M and B

$$\frac{d\boldsymbol{M}}{dt} = \gamma\, \boldsymbol{M} \times \boldsymbol{B} \tag{2.9}$$

For $\boldsymbol{B} = B_0\hat{z}$, this becomes

$$\frac{dM_x}{dt} = \gamma M_y B_0 \tag{2.10.1}$$

$$\frac{dM_y}{dt} = -\gamma M_x B_0 \tag{2.10.2}$$

$$\frac{dM_z}{dt} = 0 \tag{2.10.3}$$

with solutions

[4] About five spins out per million at a field strength of 1.5 Tesla. The difference in populations is small because the difference in energy levels is small.

$$M_x(t) = M_x(0)\cos\omega_0 t + M_y(0)\sin\omega_0 t \tag{2.11.1}$$

$$M_y(t) = -M_x(0)\sin\omega_0 t + M_y(0)\cos\omega_0 t \tag{2.11.2}$$

$$M_z(t) = M_z(0) \tag{2.11.3}$$

2.3. Excitation

If a magnetic field $\boldsymbol{B_1}$ oscillating at ω_0 is applied perpendicular to B_0 such that

$$\boldsymbol{B}_1(t) = B_1(t)\cos\omega_0 t \cdot \hat{x} - B_1(t)\sin\omega_0 t \cdot \hat{y} \tag{2.12}$$

then equations. 2.10.1 - 2.10.3 become

$$\tfrac{dM_x}{dt} = \gamma[M_y B_0 + M_z B_1 \sin\omega_0 t] \tag{2.13.1}$$

$$\tfrac{dM_y}{dt} = \gamma[M_z B_1 \cos\omega_0 t - M_x B_0] \tag{2.13.2}$$

$$\tfrac{dM_z}{dt} = \gamma[-M_x B_1 \sin\omega_0 t - M_y B_1 \cos\omega_0 t] \tag{2.13.3}$$

Defining an initial condition $\boldsymbol{M}(0) = M_0 \cdot \hat{z}$, solutions for $\boldsymbol{M}(t)$ become

$$M_x(t) = M_0 \sin\omega_1 t \sin\omega_0 t \tag{2.14.1}$$

$$M_y(t) = M_0 \sin\omega_1 t \cos\omega_0 t \tag{2.14.2}$$

$$M_z(t) = M_0 \cos\omega_1 t \tag{2.14.3}$$

where $\omega_1 = \gamma B_1$. Thus in response to an oscillating magnetic field of frequency ω_0, the magnetization simultaneously precesses about B_0 at ω_0 and B_1 at ω_1.

In a fixed frame of reference, the motion of $\boldsymbol{M}$ is complicated and can be difficult to analyze. The situation can be simplified by introducing another frame of reference (x', y', z) which rotates about z in the same direction that $\boldsymbol{M}$ rotates about $\boldsymbol{B_0}$. If the rotating frame has angular velocity $\Omega = \gamma \boldsymbol{B} = \omega_0$, then in the rotating frame $\boldsymbol{M}$ will appear stationary when precessing about B_0.

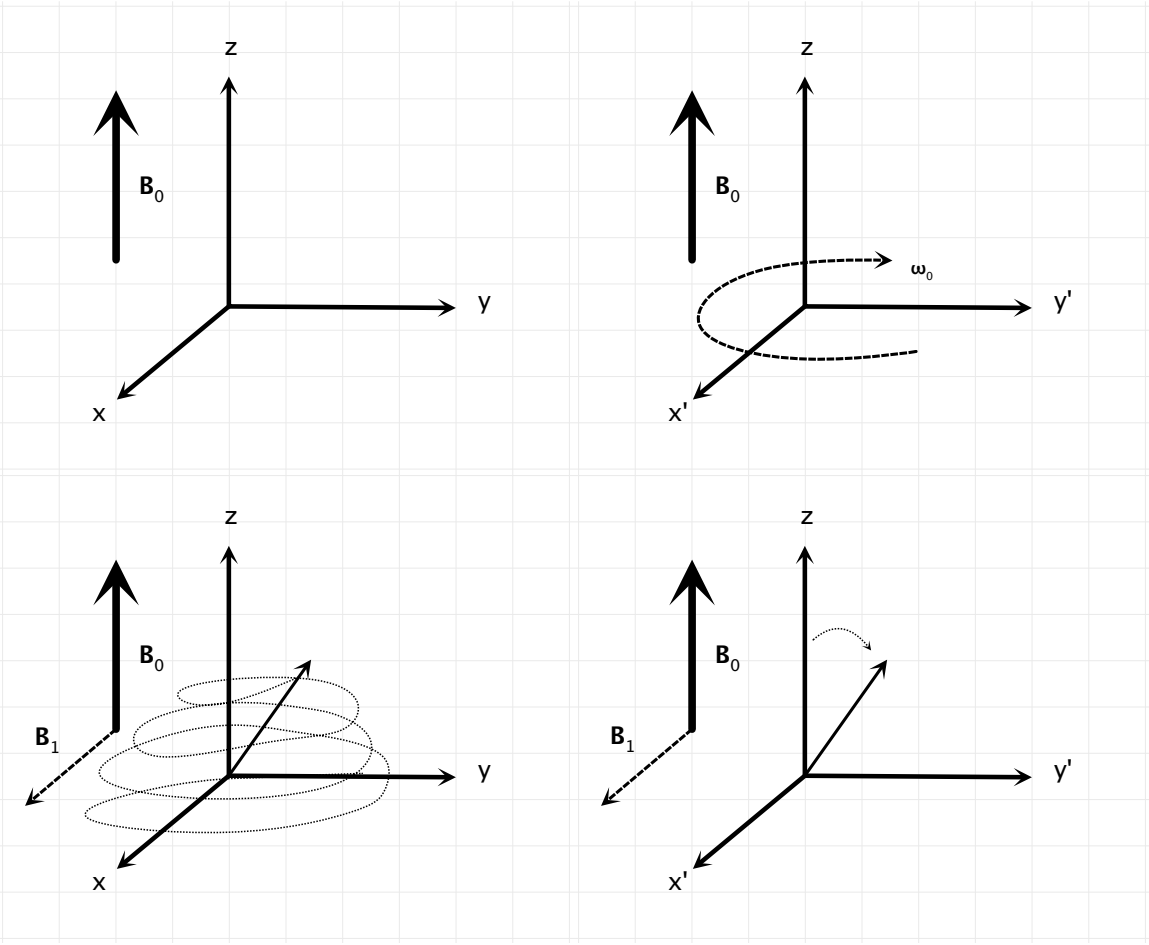

Figure 2.1: (a) The fixed laboratory frame and (b) the rotating frame of reference. B_0 is parallel to z and z' while the x' and y' axes rotate around the z' axis at ω_0. Motion of M in the laboratory frame (c) is complex compared to in the rotating frame (d).

When B_1 is tuned to the Larmor frequency of some target spins and is applied along x' for time *t*, the resulting torque rotates M toward y' by a flip angle $\theta = \gamma B_1 t$. The result is a component of the net magnetization in the y'-direction which precesses in the x'-y' plane at angular frequency ω_0.

2.4. Relaxation

Excited spins tend to release energy and return to equilibrium over time. In NMR this process is called relaxation. For a Hydrogen atom and applied field $\boldsymbol{B}$, time dependent relaxation is described quantitatively by the Bloch equation

$$\frac{d\boldsymbol{M}}{dt} = \gamma \boldsymbol{M} \times \boldsymbol{B} + \frac{1}{T_1}(M_0 - M_z)\hat{z} - \frac{1}{T_2}\boldsymbol{M}_{xy} \tag{2.15}$$

Where $\boldsymbol{M_{xy}}$ (or $\boldsymbol{M}_\perp$) and $\boldsymbol{M_z}$ are the transverse and longitudinal components of $\boldsymbol{M}$, respectively. Time constant T_1 characterizes "spin-lattice" relaxation, the rate at which excited spins exchange energy with their environment, while T_2 characterizes "spin-spin" relaxation, the rate at which excited spins exchange energy with one another. As the strength of the applied field increases, T_1 becomes longer and T_2 becomes shorter. A third parameter T_2^* accounts for signal losses due to magnetic field inhomogeneities (ΔB) in addition to T_2:

$$\frac{1}{T_2^*} = \frac{1}{T_2} + \gamma \Delta B \tag{2.16}$$

In practice, T_2^* can be much shorter than T_2. At high field, T_2^* shortening due to large ΔB is a source both of beneficial image contrast and of serious limitations on some scan techniques.

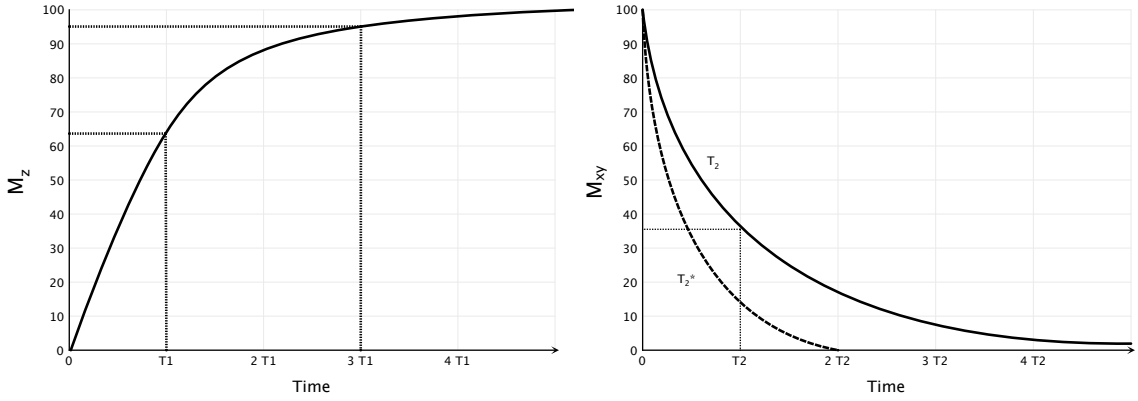

Figure 2.2: Relaxation in NMR. (a) T_1 relaxation describes the recovery rate of longitudinal magnetization. At t = T_1, M_z has regained 63% of its initial value. (b) T_2 and T_2^* relaxation describe the decay rate of transverse magnetization. At t = T_2, M_{xy} has lost 63% of its initial value. T_2^* depends on field inhomogeneities and can be substantially shorter than T_2.

2.5. The Nuclear Magnetic Resonance Signal

As magnetization precesses in the transverse plane, the time-varying magnetic flux $\Phi(t)$ through a nearby receiver coil induces an oscillating voltage $V(t)$ according to Faraday's Law:

$$V(t) = -\frac{d\Phi}{dt} \tag{2.17}$$

The NMR signal is the volume integral of transverse magnetization[5]:

[5] Primed quantities are observed in the rotating frame of reference.

$$S' = \int\int\int \boldsymbol{M'}_{\perp}(x,y,z)\,dx\,dy\,dz \tag{2.18}$$

The transverse magnetization is a complex quantity and therefore can be written in terms of magnitude and phase:

$$\boldsymbol{M'_{\perp}} = M'_x + \boldsymbol{i}\,M'_y \tag{2.19}$$

$$\boldsymbol{M'_{\perp}} = \boldsymbol{\rho}_M \cdot e^{\boldsymbol{i}\phi'} \tag{2.20}$$

$$S' = \int\int\int \boldsymbol{\rho}_M \cdot e^{\boldsymbol{i}\phi'}\,dx\,dy\,dz \tag{2.21}$$

Where $\boldsymbol{\rho}_M$ represents the spatial distribution of transverse magnetization[6] at a given time. As the magnetization relaxes, the measured signal decays according to Eq. 2.15 and is known as a Free Induction Decay (FID).

3. Magnetic Resonance Imaging

3.1. Gradient Encoding

Magnetic resonance imaging (MRI) aims to map resonance frequency (ω) to spatial location ($\boldsymbol{r}$). To make resonance frequency vary over space in a predictable way, linear gradient fields $\boldsymbol{G}(\boldsymbol{r})$ are applied along $\hat{x}$, $\hat{y}$, and $\hat{z}$ in addition to the main field B_0:

[6] The quantity $\boldsymbol{\rho}_M$ is sometimes called the Proton Density. However this term is not strictly accurate because often the spatial distribution of $\boldsymbol{M}_{\perp}$ differs from the distribution of protons, and because all nuclei contain protons but most MRI studies only image Hydrogen.

$$\boldsymbol{B}(\boldsymbol{r}) = \boldsymbol{B_0} + \boldsymbol{G} \cdot \boldsymbol{r} \tag{2.22}$$

$$\omega(\boldsymbol{r}) = \gamma B(\boldsymbol{r}) = \gamma \boldsymbol{B_0} + \gamma \boldsymbol{G} \cdot \boldsymbol{r} \tag{2.23}$$

To create an image, a specific frequency range is chosen based on a region of interest (i.e., the head for human imaging). Then one or more groups of spins are excited and encoded based on their resonance frequencies. Finally, a Fourier transform is applied to convert the frequency information into a spatial distribution of transverse magnetization: an image. The remarkable flexibility of MRI owes in part to the fact that linear gradients can be combined to image any plane at any orientation without moving either the subject or the magnet.

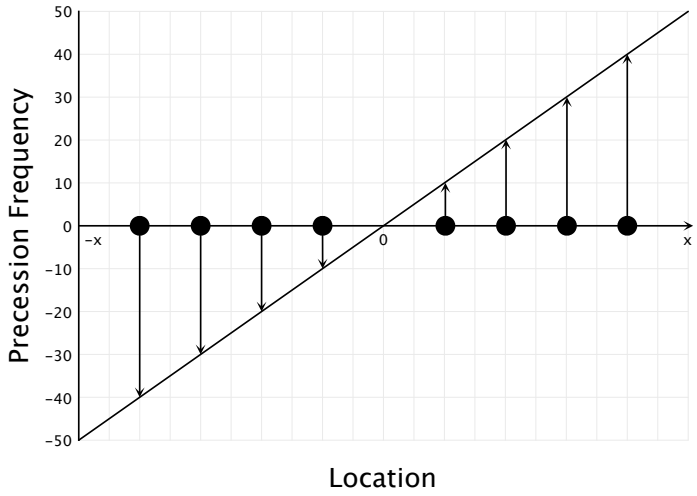

Figure 2.3: Gradient field localization of precession frequency. Gradient fields are imposed on top of B_0, causing precession frequency to vary with position. Larger arrows indicate larger precession frequencies.

3.2. Slice Selection

Many MRI experiments encode magnetization information from only one slice of the volume of interest at a time. Slice selection is achieved by applying a radio frequency pulse with bandwidth $\Delta\omega$ (centered on the resonance frequency of the target slice ω) to excite spins within a slice of thickness Δz, along with a gradient field G_z to determine slice position:

$$G_z = \frac{\Delta\omega}{\gamma\Delta z} \tag{2.24}$$

Once G_z is determined, the carrier frequency of the excitation pulse may be calculated from Eq. 2.23. Spins with resonance frequencies within the bandwidth of the slice select pulse ($\Delta\omega$) are excited to the transverse plane and behave according to the Bloch equation. The task then becomes encoding the signal within the excited region before the magnetization decays.

3.3. Frequency and Phase Encoding

If no other gradients are applied, spins in a narrow excited slice will precess at the same frequency and produce a homogeneous signal. To create an image, the resonance frequencies of these spins must be differentiated with additional gradients. According to the complex representation of the MR signal in Eq. 2.21, the spatial dimensions in an excited slice may be encoded in terms of local frequency and phase. Applying a linear gradient $\boldsymbol{G_x}$ along $\hat{x}$ yields:

$$\omega(x) = \omega_0 + \gamma G_x \cdot x \tag{2.25}$$

Now spins further along the x-axis have higher precession frequencies (as seen in Fig. 2.3), and the signal is frequency encoded[7]:

$$S'(x,t) = \int \rho_M(x)\, e^{-\boldsymbol{i}\,\gamma\, G_x \cdot x \cdot t}\, dx \tag{2.26}$$

Similarly if a gradient $\boldsymbol{G_y}$ is applied along $\hat{y}$ for a short period τ_{pe} and then turned off, spins accumulate relative phase based on their position along y during the time interval [0, τ_{pe}].

$$\phi(y) = -\,\gamma\, G_y \cdot\ y\ \cdot \tau_{pe} \tag{2.27}$$

The received signal is now phase encoded[8]:

$$S'(y,t) = \int \rho_M(y)\, e^{-\boldsymbol{i}\,\gamma\, G_y \cdot y \cdot \tau_{pe}}\, dy \tag{2.28}$$

Thus for an axial image centered on z_0 with slice thickness Δz, the signal measured at location $\boldsymbol{r}$ at time t may be written:

[7, 6] Here we have neglected relaxation effects for clarity.

$$S'(\boldsymbol{r},t) = \int\int\int_{z_0-\frac{\Delta z}{2}}^{z_0+\frac{\Delta z}{2}} \rho_M(\boldsymbol{r})\, e^{-\boldsymbol{i}\,\gamma\,(G_x\cdot x\cdot t + G_y\cdot y\cdot \tau_{pe})}\, dx\, dy\, dz \qquad (2.29)$$

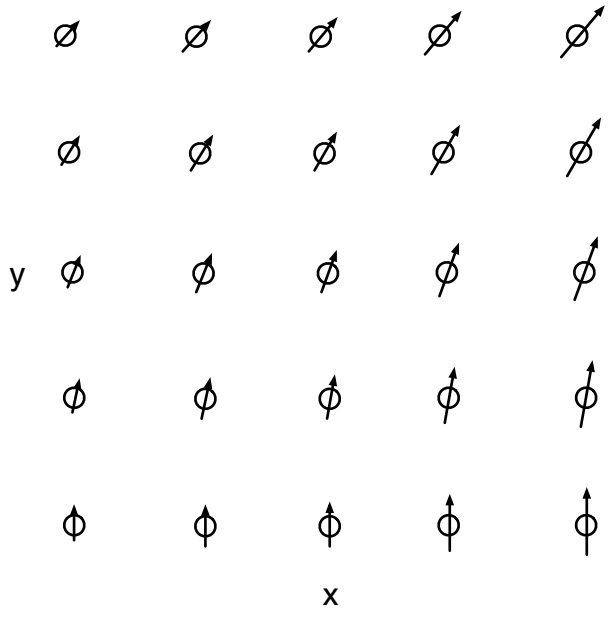

Figure 2.4: Frequency and Phase encoding. Each spin has a unique combination of frequency and phase. Precession frequency increases from left to right, while phase increases from bottom to top.

Gradient encoding may be thought of as plane-wave modulation of the transverse magnetization such that each combination of G_x and G_y corresponds to a specific resonance frequency and specific location (Pruessmann, 2006). Only one such modulation can be applied and encoded at a time. This places fundamental limits on the speed at which MR data may be sampled with standard gradient encoding schemes. Increasing the data acquisition rate in conventional Fourier MRI requires increasing the speed at which distinct gradient modulation states can be achieved and encoded. Later we discuss Parallel Imaging (PI)

methods, which use hybrid encoding techniques to accelerate MR acquisitions without requiring faster gradients.

3.4. Sampling in k-space

Here it is convenient to introduce k_x and k_y:

$$k_x = \gamma \int_0^t G_x(\tau) d\tau \tag{2.30.1}$$

$$k_y = \gamma \int_0^t G_y(\tau) d\tau \tag{2.30.2}$$

These parameters describe how precession frequency (k_x) and spin phase (k_y) vary over space - that is, spatial frequency in the frequency and phase encoding directions. This concept is central to data sampling in MRI. Ignoring relaxation, the signal in an excited slice can be written:

$$S'(k_x, k_y) = \int \int \rho_M(x, y)\, e^{-\boldsymbol{i}[k_x \cdot x + k_y \cdot y]} dx\, dy \tag{2.31}$$

This is a Fourier transform with $e^{-\boldsymbol{i}[k_x \cdot x + k_y \cdot y]}$ as the Fourier kernel. Hence equation 2.30 states that the signal measured in a receiver coil at a given time is the Fourier transform of $\rho_M(x, y)$, which has been sampled in "k-space" at spatial frequency (k_x, k_y). In practice it is possible to sample only a finite number of points in k-space during a scan. Performing an inverse 2D discrete

Fourier transform (DFT) on the sampled values of (k_x, k_y) yields $\rho_M(x, y)$, a two-dimensional map of the transverse magnetization (Eq. 2.32). This is the so-called "magnitude image" and is the end product of many MRI studies.

$$\rho_M(x,y) = \Delta k_x \, \Delta k_y \sum_{n=-\frac{N_y}{2}}^{\frac{N_y}{2}-1} \sum_{m=-\frac{N_x}{2}}^{\frac{N_x}{2}-1} S'(m\,\Delta k_x, n\,\Delta k_y)\, e^{i[m\cdot\Delta k_x\cdot x + n\cdot\Delta k_y\cdot y]} \tag{2.32}$$

Where m and n are the number of samples required to span the N_x by N_y data matrix, and $\Delta k_x = \frac{k_x}{m}$ and $\Delta k_y = \frac{k_y}{n}$ are the sampling step sizes in the frequency and phase encoding directions.

3.5. Echoes

Although the FID is the basic response of a spin system after excitation, another type of signal known as an echo is more commonly measured in MRI experiments. The term echo refers to a local maximum of the NMR signal which is achieved when spins in a given area are completely in phase. To form an echo, the transverse magnetization is intentionally de-phased following excitation and then re-phased at a chosen time known as the echo time (TE). Echoes can be formed through the application of additional radio frequency pulses after excitation (*spin echoes*), or through manipulation of the linear gradient fields (*gradient* or *field echoes*).

Refocusing pulses applied to generate spin echoes are advantageous in that they re-phase transverse magnetization lost to local field inhomogeneities (ΔB - see Eq. 2.16) as described by T_2*. The maximum signal amplitude of a spin echo is determined by T_2. By contrast, gradient echoes do not correct phase errors owing to ΔB. Therefore the maximum signal produced by a gradient echo is determined by T_2^* and can be substantially less than a spin echo. However, gradient echoes can be created very quickly and are appropriate for many fast imaging sequences. Since this work focuses on optimizing fast gradient-echo sequences for imaging brain function, we now restrict our discussion to gradient echoes and related methods.

3.6. The Gradient Echo

The linear gradient fields described in section 3.3 can dephase and rephase the signal from a population of spins to create one or more echoes. Figure 2.5 shows the process of generating a gradient echo. After excitation, a negative field gradient causes spins precessing in the transverse plane to dephase relative one another in proportion to the area under the gradient. After de-phasing, the gradient is reversed. When the area under the rephasing gradient equals that under the dephasing gradient, the spins be in phase again and the transverse magnetization reaches its peak value as determined by T_2^*.

The signal resulting from a gradient-echo behaves according to:

$$S_{GE} = M_0 \cdot \sin\theta \cdot \frac{1 - e^{\frac{-TR}{T_1}}}{1 - \cos\theta \cdot e^{\frac{-TR}{T_1}}} \cdot e^{\frac{-TE}{T_2^*}} \tag{2.33}$$

Where M_0 is the initial magnetization, θ is the flip angle, TR is the repetition time, TE is the echo time.

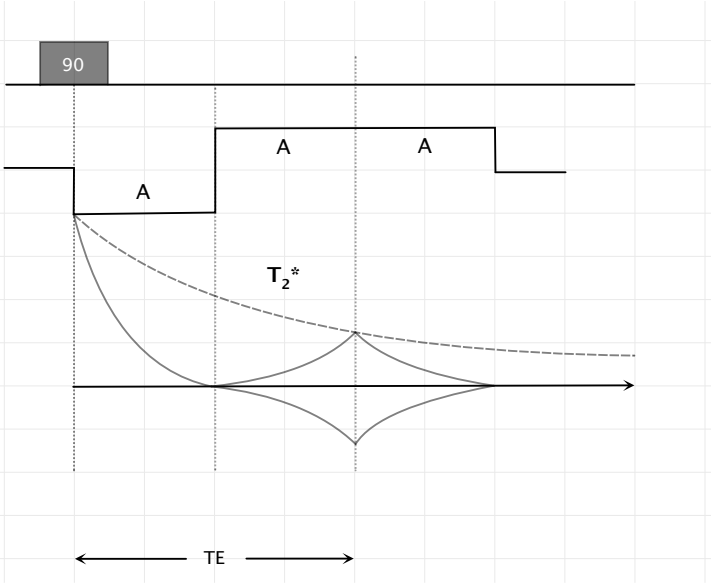

Figure 2.5: Gradient echo formation. After an excitation pulse, a dephasing gradient is activated (with integrated area 'A'), followed by a rephasing gradient of twice the area. Signal amplitude at TE is determined by T_2^*.

4. Imaging Sequences

Prescriptions for creating and encoding transverse magnetization in MR imaging are called pulse sequences. By controlling the manner in which spins are excited and acquired, pulse sequences can be tuned to acquire images based on T1, T2, T2*, proton density, magnetic susceptibility, water diffusion, and more. In this work we focus on sequences geared toward imaging brain function,

which generally requires that a series of T2*-weighted images be acquired with high temporal resolution. The most popular pulse sequence for this type of acquisition, especially at field strengths of 3 Tesla and below, is gradient-echo Echo Planar Imaging (EPI).

4.1. Gradient Echo Echo Planar Imaging

Echo Planar Imaging aims to acquire an entire image following a single excitation pulse. Within an excited plane, all of k-space is sampled with a train of gradient echoes generated by rapidly oscillating frequency encoding gradients and "blipped" phase-encoding gradients. We refer to the specific case of multi-slice gradient echo EPI as 2D-EPI. Figure 2.6 shows a standard 2D-EPI pulse sequence and the associated sampling trajectory in k-space.

Rapid k-space sampling in 2D-EPI effectively freezes motion and allows imaging of dynamic processes in the body with a time series of images. 2D-EPI maximizes the fraction of imaging time devoted to data acquisition and generally provides high SNR per unit time (SNR efficiency). On the other hand, the quality of individual 2D-EPI images is generally quite poor. Because the entire echo train is collected within one T_2^* decay envelope, 2D-EPI is sensitive to magnetic field inhomogeneities which cause neighboring to spins become out of phase during readout. In section 5 we show how off-resonance effects can lead to distortion, blurring, and signal loss in 2D-EPI images. To minimize these effects, 2D-EPI employs rapidly switched gradients and high readout bandwidth.

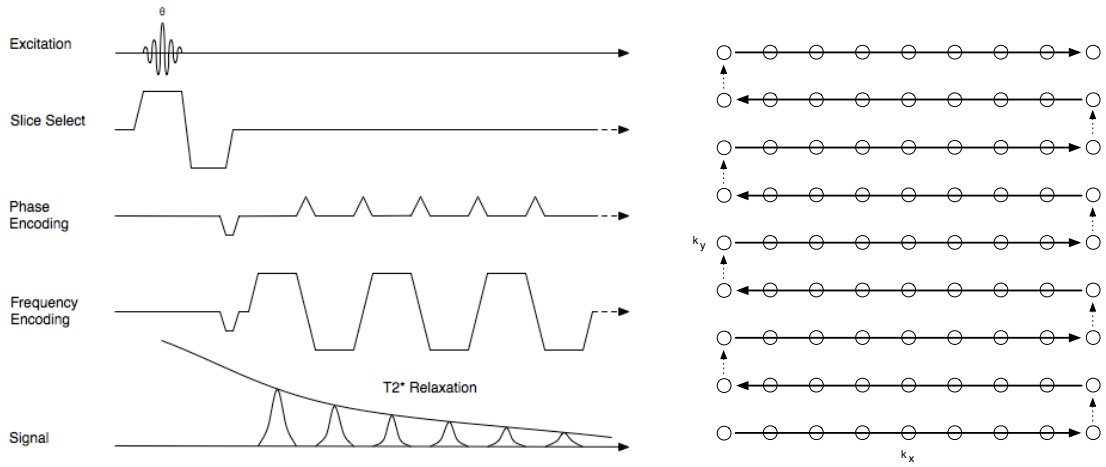

Figure 2.6: (a) Pulse sequence and (b) k-space trajectory for a standard 2D-EPI sequence with Cartesian sampling. k-space sampling begins at the bottom left and travels to the right as the frequency encoding gradient is increased. When the end of one line of k-space is reached, the phase encoding gradient is "blipped" and sampling of a new line in k-space begins when the frequency encoding gradient is reversed. The entire train of gradient echoes is acquired within one T_2^* envelope. This process is repeated for each slice in the volume.

2D-EPI sequences are most useful when a series of images must be acquired in which high temporal resolution is more important than the quality of individual images. At high field strengths, technical limitations on 2D-EPI become severe and alternate imaging sequences may be preferable for certain applications. We now consider two alternatives to 2D-EPI for fast imaging: multi-shot 3D-Fast Field Echo (3D-FFE) and multi-shot 3D-PRESTO (Principles of Echo-Shifting with a Train of Observations).

4.2. Three Dimensional Gradient Echo Imaging: 3D Fast Field Echo

There are several important differences between single-shot 2D-EPI and multi-shot 3D gradient echo sequences. 2D-EPI excites individual slices and then acquires a train of phase encoded gradient echoes for that slice. Multi-shot 3D

gradient echo sequences excite and acquire data along the entire third dimension of the imaging volume (the slab), which is then encoded using a second phase-encoding gradient. The signal in a slab-selective 3D acquisition can be written:

$$S'(k_x, k_y, k_z) = \int\int\int \rho_M(x, y, z)\, e^{-\boldsymbol{i}[k_x \cdot x + k_y \cdot y + k_z \cdot z]} dx\, dy\, dz \qquad (2.34)$$

The magnitude image $\rho_M(x, y, z)$ is now recovered from a 3D inverse DFT. As a gradient-echo, echo-train pulse sequence, the signal in 3D-FFE behaves according to Equation 2.33.

Acquiring data in this way generally requires multiple RF excitations, each followed by a shorter train of echoes, which are combined to form the entire data set. Critically, short echo trains reduce the sensitivity of multi-shot techniques to off-resonance effects compared to single-shot techniques. Figure 2.7 shows a pulse sequence and k-space trajectory for a multi-shot 3D gradient echo acquisition with a short echo train (known as 3D Fast Field Echo, or 3D-FFE). This is identical to the 2D-EPI sequence, except that now phase encoding is applied independently in the *y* and *z* directions (black arrow).

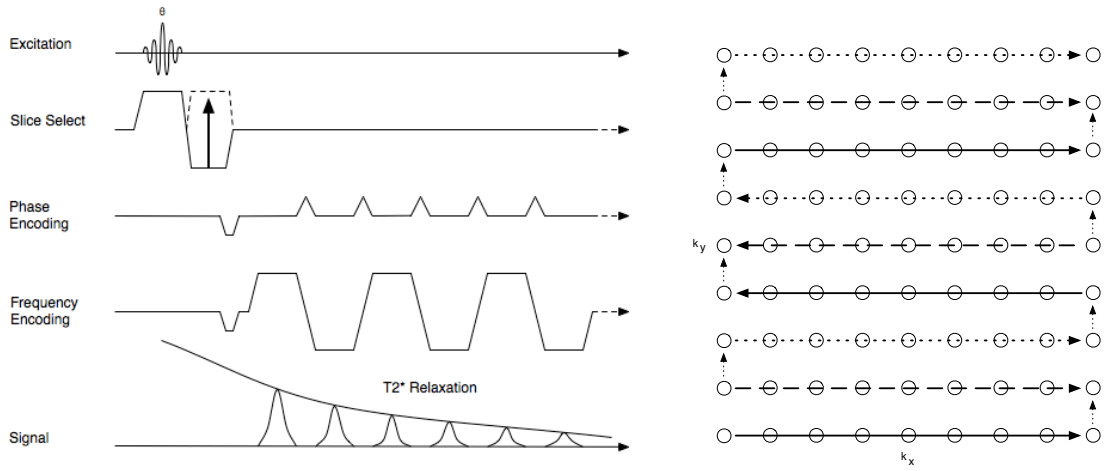

Figure 2.7: (a) Pulse sequence and (b) k-space trajectory for a 3D-FFE sequence with Cartesian sampling. Different shots, corresponding to different echo train readouts, are shown with solid, dotted, and dashed lines. The shorter echo trains experience significantly reduced T_2^* effects compared to 2D-EPI.

Three dimensional acquisition methods have several inherent benefits. Slab-selective excitation reduces sensitivity to blood inflow effects and eliminates issues related to slice timing found in 2D multi-slice sequences. Random thermal noise is also decreased because the signal is averaged over a larger volume in slab-selective 3D methods compared to 2D acquisitions which generally excite only one slice at a time. 3D methods therefore become more favorable as the slab size increases.

On the other hand, multi-shot acquisitions are sensitive to between-shot motion and phase errors because the entire data set is not acquired within one excitation Further, the additional phase encoding steps in 3D techniques lead to significant scan time increases over 2D-EPI. Therefore to achieve temporal resolutions suitable for imaging brain function, 3D sequences commonly utilize shorter TRs and smaller flip angles compared to 2D-EPI. Together, these lead to

less transverse magnetization to generate the NMR signal. Figure 2.8 shows the transverse magnetization created by small and large flip angles.

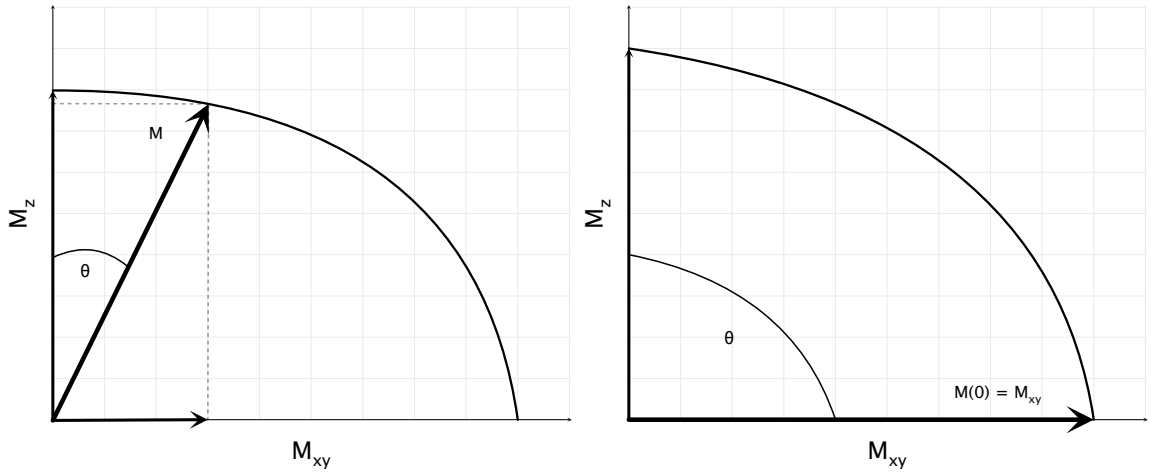

Figure 2.8: Flip angle and transverse magnetization. (a) A small flip angle typical of a 3D gradient echo acquisition. (b) A 90 degree flip angle typical of a 2D-EPI acquisition.

4.3. Principles of Echo Shifting with a Train of Observations (PRESTO)

In standard gradient-echo acquisitions, the time between excitation and signal acquisition at TE is generally unused. 3D-PRESTO acquisitions make optimal use of this time through echo shifting, which delays formation of the gradient echo from one group of excited spins until the excitation pulse for the next group of spins has been issued (Liu et al., 1993). An additional echo-shifting gradient is applied to delay formation of the shifted echo until the *effective* echo time ($TE_{eff} = TE_{nominal} + n \cdot TR$). Figure 2.9 shows a pulse sequence for multi-shot 3D-PRESTO with a short echo-train. Provided the echo train lengths are the same for both sequences, the k-space trajectory for 3D-PRESTO is the same as that of 3D-FFE (Fig 2.8b).

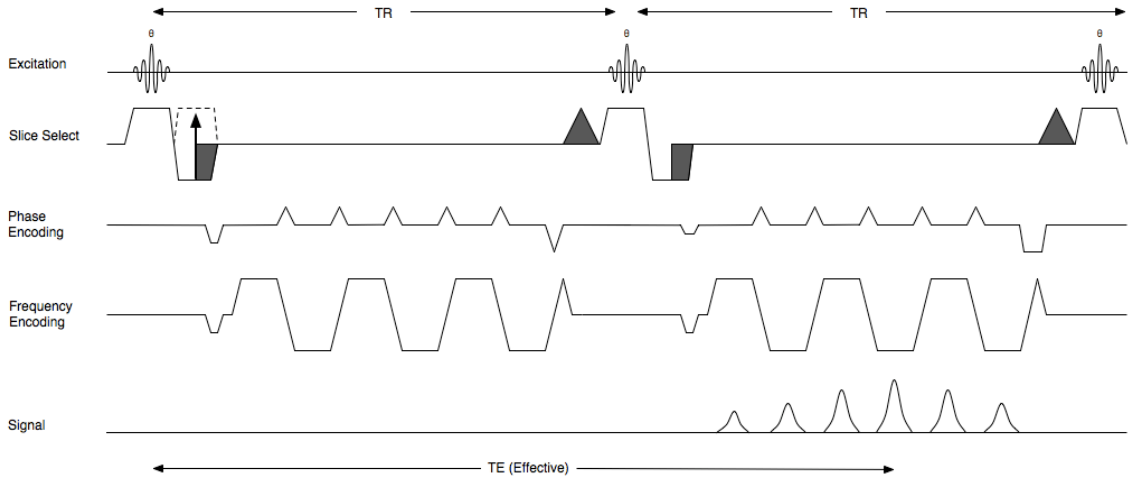

Figure 2.9: Pulse sequence for a 3D-PRESTO with echo train length of six. Shaded blocks are the equal-area gradient lobes for additional dephasing and rephasing necessary to achieve a shifted echo with TE > TR.

3D-PRESTO shows the same basic signal behavior, benefits, and drawbacks as 3D-FFE, with a few significant differences related to echo-shifting. The signal for 3D-PRESTO can be written

$$S_{ES-GE} = S_{GE} \cdot \cos^{2 \cdot n}\left(\frac{\theta}{2}\right) \cdot e^{\frac{-nTR}{T_2^*}} \tag{2.35}$$

Where the cosine term represents destructive interference from RF pulses occurring between excitation and collection of a shifted echo, and the exponential term represents enhanced T_2^* weighting due to the longer effective echo time $TE_{eff} = TE_{nominal} + n \cdot TR$ of the shifted echo[9] (Denolin and Metens, 2004). This signal behavior applies when gradient or RF spoiling is used to prevent

[9] Here *n* is the number of TR periods over which the echo is shifted. This is usually *n* = 1.

accumulation of transverse magnetization over multiple TR periods in an echo-shifted sequence (Moonen et al., 1992; Liu et al., 1993). When echo-shifted scans do not fulfill this condition and transverse magnetization accumulates across TR periods, the signal behavior becomes considerably more complex (Denolin and Metens, 2004; Chung and Duerk, 1999). The 3D-PRESTO sequences studied here use RF spoiling and therefore obey Eq. 2.35.

According to Eq. 2.35, 3D-PRESTO has reduced raw signal compared to 2D-EPI and 3D-FFE. However, the time savings offered by echo shifting can lead to a net gain in signal-to-noise per unit time (SNR efficiency) if the number of images collected within a given TR period is large (Neggers et al., 2008).

5. Off-Resonance Effects

Magnetic Resonance Imaging is based on the assumption that resonance frequency is linearly dependent on position. Additional field variations will cause precession frequencies to deviate from the expected values and will introduce errors into the gradient encoded signal. When the local field differs from the applied field $\boldsymbol{B}$ by ΔB, local spins are said to be off-resonance and may be misrepresented in the reconstructed image.

One major source of magnetic field inhomogeneities is variation in magnetic susceptibility, χ, which measures measures the extent to which a material becomes magnetized when placed in an external field. Susceptibility differences $\Delta\chi$ between soft tissue and surrounding air or bone structures lead to magnetic field distributions across individual voxels. The resulting errors in

gradient encoding are called magnetic susceptibility effects (MSE), and manifest as non-uniform slice excitation, geometric and intensity distortion within an image, and through-plane signal losses in echo train techniques. Magnetic field inhomogeneities and MSE become more severe as field strengths increase.

In addition to static magnetic susceptibility effects, physiological processes such as cardiovascular pulsation, brain motion, respiratory motion of the lungs and diaphragm, as well as changes in gas susceptibility due to breathing in living subjects can create time-varying $\Delta\chi$ over the imaging volume. Respiration in particular is a primary source of time-varying susceptibility variation[10], introducing a magnetic field inhomogeneity that depends on the inverse cube of the distance from the lungs (Raj et al., 2000; Zhao 2006; Van de Moortele et al., 2007).

5.1. Image Distortion in Gradient Echo EPI

In 2D-EPI, spatial information is encoded by an oscillating frequency encoding gradient along with a series of short phase encoding gradient pulses. If TE is the effective echo time, T is the time interval between adjacent k_y lines, and Δt is the time between samples in k_x, then the time at the n-th k_y and m-th sample point is (Zhao, 2006):

$$t = TE + nT \pm m\Delta t \tag{2.36}$$

[10] During normal breathing, the oxygen concentration can change by as much as 7% in the lungs, leading to a 0.12 ppm changes in the air susceptibility and inducing magnetic field fluctuation in the brain (Raj et al., 2000; Zhao 2006).

A field inhomogeneity $\Delta B(x,y)$ in the imaging plane will cause a pixel originally at (x, y) to appear at x_1, y_1 in the reconstructed image $\rho_1(x_1,y_1)$:

$$x_1 - x = \pm\frac{\gamma\Delta B(x,y)\Delta t}{2\pi\Delta k_x} \qquad y_1 - y = \frac{\gamma\Delta B(x,y)T}{2\pi\Delta k_y} \tag{2.37}$$

For an image with pixel size of $\Delta x \cdot \Delta y$,

$$\Delta k_x = \frac{1}{N_x\,\Delta x} \qquad \Delta k_y = \frac{1}{N_y\,\Delta y} \tag{2.38}$$

The relative pixel shift in the imaging plane are then (Zhao, 2006):

$$\frac{x_1-x}{\Delta x} = \pm N_x\,\Delta f(x,y)\,\Delta t \qquad \frac{y_1-y}{\Delta y} = \pm\,N_y\,\Delta f(x,y)\,T \tag{2.39}$$

Where

$$\Delta f(x,y) = \frac{\gamma\,\Delta B(x,y)}{2\pi} \tag{2.40}$$

is the resonance frequency offset due to local magnetic field inhomogeneities.

Though in principle off-resonance effects can occur in any direction, in 2D-EPI strong frequency encoding gradients and high sampling rates generally lead

to negligible off-resonance effects in the frequency encoding direction. By contrast, the sampling rate in the phase encoding direction is at least N_x times less than in the frequency encoding direction because N_x gradient echoes are acquired between phase encoding steps. Therefore 2D-EPI experiences serious off-resonance effects in phase encoding direction. Neglecting relaxation and taking field inhomogeneities into account, the received signal for a given slice acquired with gradient-echo 2D-EPI at the echo time TE becomes (Zhao, 2006):

$$S'(k_x, k_y) = \int\int \rho_M(x,y) e^{-\boldsymbol{i}\,\gamma\,\Delta B(x,y)\,TE} e^{-\boldsymbol{i}\,k_x\,[x \pm \frac{\gamma\,\Delta B(x,y)\,\Delta t}{2\,\pi\,\Delta k_x}]} e^{-\boldsymbol{i}\,k_y\,[y + \frac{\gamma\,\Delta B(x,y)\,T}{2\,\pi\,\Delta k_y}]} dx\,dy \quad (2.41)$$

The first exponential term in the integral describes signal losses if ΔB varies within voxel. The second and third exponential terms describe the pixel shifts we have just discussed. According to the Fourier shift theorem, additional phase in k-space creates a linear pixel shift in image space. In particular, bulk off-resonance shifts causes a net shift of the image in the phase encoding direction, whereas a linear field shift in the phase encoding direction causes a compression or expansion of the image in the phase encoding direction. This is the commonly observed geometric distortion effect in echo-train sequences. Distortion also

occurs in the slice select direction, causing heterogeneous slice thickness, intensity distortion, and through-plane signal losses (Zhao, 2006).

Increasing in-plane resolution for a given field of view worsens these effects in 2D-EPI because it increases N_x and further reduces the sampling rate in k_y. This is particularly troubling at high field, because achieving higher spatial resolutions is a primary motivation for increasing field strength. Local field inhomogeneities also tend to increase with field, making the task of acquiring artifact-free images with 2D-EPI quite difficult at 7T and above.

6. The Signal to Noise Ratio

6.1. Spatial Signal to Noise

The signal-to-noise ratio (SNR) describes the ability to differentiate relevant information from the unwanted noise inherent to MR data. For a given set of experimental conditions, the theoretical SNR of an image can be written:

$$SNR = K \cdot \Delta x \cdot \Delta y \cdot \Delta z \cdot \sqrt{\left(\frac{N_x \, N_y \, N_z \, N_{EX}}{BW_{read}} \right)} \qquad (2.42)$$

Where Δx , Δy , and Δz are voxel dimensions, N_x , N_y , and N_z are the number of gradient encoding steps (for 2D imaging, N_z = 1), N_{EX} is the number of excitations used for signal averaging, BW is the receiver bandwidth, and K is a parameter that includes hardware, pulse sequence and tissue dependent

factors. According to Eq. 2.42, 3D acquisitions enjoy an increased signal-to-noise ratio of $\sqrt{N_z}$ compared to equivalent 2D scans when all else is equal. Using Eqs. 2.33 - 2.35, the SNR of 2D-EPI, 3D-FFE and 3D-PRESTO are given by:

$$SNR_{2D-EPI} = S_{GE} \cdot \Delta x \cdot \Delta y \cdot \Delta z \cdot \sqrt{\left(\frac{N_x\, N_y\, N_{EX}}{BW_{read}}\right)} \tag{2.43.1}$$

$$SNR_{3D-FFE} = S_{GE} \cdot \Delta x \cdot \Delta y \cdot \Delta z \cdot \sqrt{\left(\frac{N_x\, N_y\, N_z\, N_{EX}}{BW_{read}}\right)} \tag{2.43.2}$$

$$SNR_{3D-PRESTO} = S_{ES-GE} \cdot \Delta x \cdot \Delta y \cdot \Delta z \cdot \sqrt{\left(\frac{N_x\, N_y\, N_z\, N_{EX}}{BW_{read}}\right)} \tag{2.43.3}$$

As mentioned in section 4.2, 3D sequences designed for functional imaging acquisitions often use much smaller flip angles and shorter repetition times than 2D-EPI. Together these lead to significantly reduced raw signal. Combined with the $\sqrt{N_z}$ SNR benefit of 3D acquisition, 2D multi-slice and 3D volume data are often offer similar SNR performance. We present a detailed comparison 2D-EPI, 3D-FFE, and 3D-PRESTO in Chapter V.

The measured SNR in individual MR images is defined:

$$SNR_0 = \frac{\overline{S}}{\sigma} \tag{2.44}$$

Where $\overline{S}$ and σ are the mean and standard deviation of signal within a nominally uniform region of interest (ROI). Because gradient-echo sequences

acquire individual images very quickly, it is safe to assume that SNR_0 does not depend on signal fluctuations over time. The image signal to noise ratio is frequently used to describe the quality of individual images and is of critical importance in anatomical and diagnostic imaging.

6.2. Temporal Signal to Noise

Some experiments require high signal stability over time in a rapidly acquired series of images. The temporal signal to noise ratio (TSNR) is defined as the mean value of a signal within a single voxel compared to the standard deviation of the signal in that voxel over time in a series of images.

$$TSNR = \frac{\overline{S}}{\sigma} \tag{2.45}$$

Several noise components contribute to the total signal variation in a time series of images. These include time-varying thermal noise (σ_T), noise caused by system instability (σ_S) and, in living subjects, physiological noise from metabolic, cardiac, or respiratory activity and related motion (σ_P). When these are independent the total noise may be written:

$$\sigma = \sqrt{\sigma_T^2 + \sigma_S^2 + \sigma_P^2} \tag{2.46}$$

First identified by Weiskoff et al. in 1993, physiological noise (σ_P) is now known to be a dominant source of temporal signal variation in time series data. Physiological noise can be further broken into two components (Kruger and Glover, 2001; Triantafyllou et al., 2005):

$$\sigma_B = c_1 \cdot T_2^* \cdot TE \cdot S \tag{2.47.1}$$

$$\sigma_{NB} = c_2 \cdot S \tag{2.47.2}$$

Where c_1 and c_2 are hardware dependent constants and S is the signal. The total temporal variation in a time series of images can then be written:

$$\sigma = \sqrt{\sigma_S^2 + \sigma_T^2 + \sigma_B^2 + \sigma_{NB}^2} \tag{2.48}$$

Because Eqs. 2.47.1-2 depend on the NMR signal, the contributions of physiological noise increase with magnetic field strength and voxel volume (Kruger and Glover, 2001; Triantafyllou et al., 2005; Triantafyllou et al., 2007). Several techniques for physiological noise removal have been suggested, including navigator echoes, retrospective gating, digital filtering, k-space and image-space based estimation, pulse sequence gating, and more (Hu et al., 1995; Wowk et al., 1997; Biswal et al., 1996; Glover et al., 2000; Chuang et al., 2001; Le et al 1996).

This model treats physiological noise as purely additive and independent from other temporal noise sources. While microscopic magnetic susceptibility effects are accounted for through the T_2^* term in 2.47.1, this model does not account for bulk magnetic susceptibility effects as described in section 5, and therefore may not fully characterize the effects of σ_P on a time series of images, particularly at high field where physiological noise dominates temporal signal variance, or when or when certain acquisition techniques are applied. We explore this issue in detail in Chapter III.

7. Image Characteristics

7.1. Spatial Resolution

In order to fulfill the Nyquist sampling limit[11] and avoid aliasing in reconstructed MR images, k-space must be sampled at a spatial frequency of $1/\Delta k = FOV$, where FOV (field of view) is the distance across a given dimension in the image. Encoding frequency along $\hat{x}$ and phase along $\hat{y}$:

$$\Delta k_x = \gamma\, G_x\, \Delta t = \frac{1}{FOV_x} \tag{2.49.1}$$

$$\Delta k_y = \gamma\, \Delta G_y\, \tau_{pe} = \frac{1}{FOV_y} \tag{2.49.2}$$

[11] The Sampling Theorem states that in order to be accurately reconstructed from discrete samples, the sampling rate must be no less than twice the highest frequency present in the reference signal.

Where Δt is the interval between samples in the frequency encoding direction and ΔG_y is the phase encoding gradient step size. Pixel sizes along these dimensions are:

$$\Delta x = \frac{FOV_x}{N_x} = \frac{1}{N_x \, \gamma \, G_x \, \Delta t} = \frac{1}{N_x \, \Delta k_x} \tag{2.50.1}$$

$$\Delta y = \frac{FOV_y}{N_y} = \frac{1}{N_y \, \gamma \, \Delta G_y \, \tau_{pe}} = \frac{1}{N_y \, \Delta k_y} \tag{2.50.2}$$

Hence spatial resolution is fundamentally limited to $1/(N\Delta k)$, and is determined by gradient strength, gradient encoding bandwidth, and acquisition matrix size. High spatial resolution provides more detailed images for anatomical scans, and better localization brain activity during functional scans. However, as seen from the signal-to-noise relation (Eq. 2.42), small voxel volumes reduce SNR. A main benefit of high field imaging is the increase in baseline signal which in turn allows higher spatial resolutions to be achieved with reasonable SNR.

When sampling at the Nyquist limit is not achieved (i.e., Δk is too large), the FOV is reduced and signal from portions of the object outside the field of view are aliased back onto the edges. Figure 2.10 shows aliasing in the case of inadequate sampling in the phase encoding direction.

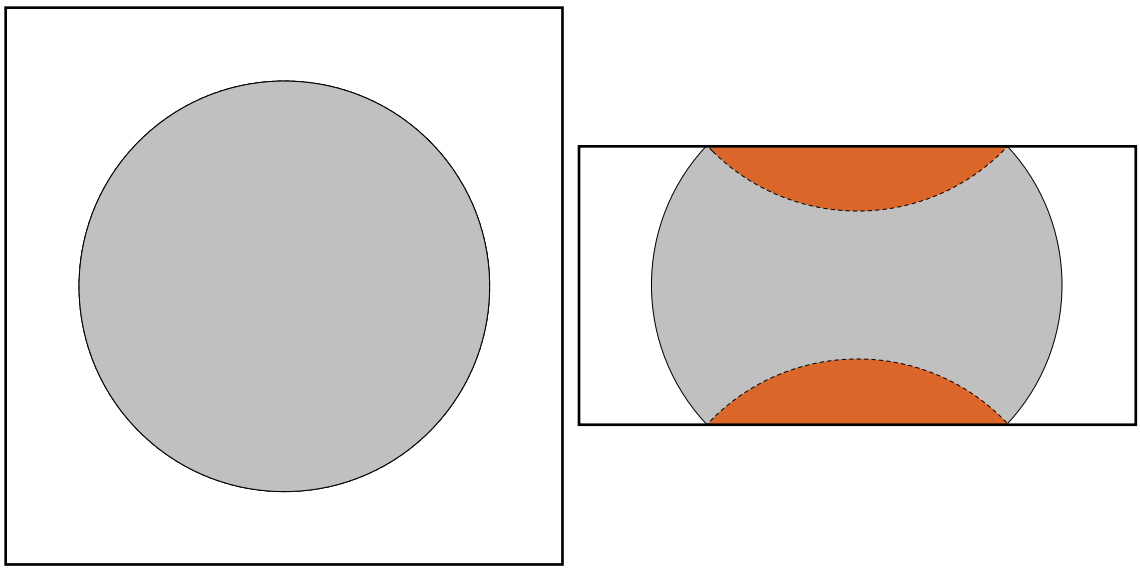

Figure 2.10: (a) Full FOV image with no aliasing. (b) Aliasing due to under-sampling of data in k-space. The field of view is reduced by half in the phase encoding direction and signal from outside the FOV is aliased back onto the edges.

7.2. Image Contrast

Image contrast is defined in terms of image intensity differences. NMR relaxation causes image contrast to depend on the timing of RF pulses used in the experiment. Three major types of contrast depend on proton density, T_1, and T_2. Proton density contrast is linearly proportional to the tissue proton density difference, while T_1 and T_2 contrasts are exponentially related to variations in the relaxation times as described by the Bloch equation. One of the most important sources of contrast in modern magnetic resonance imaging depends on T2* and is related to microscopic susceptibility variations between oxygenated and deoxygenated blood.

8. Functional Magnetic Resonance Imaging

8.1. The BOLD Signal

Metabolic effects associated with brain activity transform diamagnetic oxyhemoglobin into paramagnetic deoxyhemoglobin, causing small but significant signal changes in a series of T2*-weighted images over time. MSE from deoxyhemoglobin affect the phase coherence of local spins which in turn shorten T2* and reduce the measured signal. This blood-oxygen level dependent (BOLD) contrast forms the basis of most functional magnetic resonance imaging experiments (fMRI) (Ogawa et al., 1993). Depending on the application, low-resolution coverage of the entire brain or high-resolution coverage of specific brain areas may be desirable. Most fMRI experiments at 1.5 or 3.0T employ single-shot 2D-EPI with about 30 slices of matrix size 64x64 or 80x80 with 3 x 3 x 3mm^3 voxels in about 2.5 seconds.

At high field, BOLD sensitivity and achievable spatial resolutions are expected to increase (Bandettini, 2007). Specifically, the BOLD effect varies with the square of the applied field for small vessels, whereas for large blood vessels it varies linearly (Ugurbil et al., 1999). Therefore at high field microvascular contributions to the BOLD signal are expected to increase relative to those of large vessels, resulting in the ability to detect brain activation with greater specificity (Zhao et al., 2007). Bulk magnetic susceptibility effects also increase at high field, however causing serious artifacts in 2D-EPI as discussed in section 5. In addition, the TSNR of high field fMRI data tends to be limited by physiological noise when image SNR is high, and respiratory effects have been

shown to cause more spin dephasing and signal loss at high field (Triantafyllou et al., 2005; Van de Moortele et al., 2007).

8.2. fMRI Data Analysis

In a functional MRI experiment, images must be acquired quickly to adequately sample the hemodynamic response to brain activity. The speed at which these images must be acquired also means the SNR of individual images in an fMRI time series tends to be low. To make up for this, many images are generally obtained in both 'task' and 'rest' conditions. Differences in signal between the two are then compared to a measure of temporal signal variance (i.e., TSNR) and significant differences between 'task' and 'rest' are then determined by statistical means. Therefore high temporal signal stability is critical to BOLD fMRI experiments.

Functional MRI data processing is a deep field in its own right. Briefly, some common fMRI data processing steps include: motion correction to ensure registration throughout a time series of images which may have been collected over several minutes (Friston et al., 1996); "slice timing" correction of phase differences between slices acquired at significantly different times in multi-slice acquisitions like 2D-EPI[12] (Friston et al., 1998; Van de Moortele et al., 1997); spatial smoothing to increase image SNR and improve signal detection capabilities at the cost of subject-specific activation information; and distortion

[12] 3D volume acquisition methods do not suffer from slice timing effects because the excite the entire slab during each repetition.

correction to ensure adequate registration of functional activity to associated anatomical images (Jezzard et al., 1999; Hutton et al., 2002).

After pre-processing, fMRI data is commonly analyzed in the context of the general linear model (GLM) (Friston et al., 1994 a, b; Friston et al., 1995 a, b), which assumes a linear relationship between the measured data and the task-induced changes, such that:

$$y(t) = \beta_i \cdot x_i(t) + c + e(t) \tag{2.51}$$

In which the subscript i counts the number of regressors in the model, and where $y(t)$ is the time series of a given voxel, $x(t)$ is a regressor of interest (i.e., a task), c is a constant, and $e(t)$ is the residual error of the model which accounts for variance in $y(t)$ which cannot be explained by the linear model[13]. Beta weights β are commonly estimated through an ordinary least squares fit to the GLM and are used to determine the significance of activation (commonly measured as T- or F-statistics). As the work presented here focuses mostly on data acquisition methods, we employ mainly standard procedures for fMRI experiment design, pre-processing, and analysis. Details of each specific fMRI experiment are presented in the appropriate chapters.

[13] This "residual variance" plays an important part in our analysis of physiological noise in high field fMRI as presented in Chapter III.

9. Parallel Imaging

9.1. Overview of Parallel Imaging

Spatial encoding in standard Fourier MRI is accomplished exclusively by means of gradient fields. Each point in k-space corresponds to a certain magnetization state under specific frequency and phase encoding gradients, and only one such sample can be measured at a time (Pruessmann, 2006). Hence gradient encoding (k-space sampling) rates place fundamental limitations on the speed of data collection in MRI. Although gradient performance has improved steadily, the inherent limits of k-space speed have almost been reached due to safety and technical concerns (Roemer et al., 1990; Pruessmann et al., 1999).

A major innovation in the past decade has been the development of imaging techniques employing multiple receiver coils in parallel. Central to this method is the fact that a given receiver coil has a spatially varying “sensitivity profile” which describes the voltage induced in the receiver as a function of its distance from the signal source. In a receiver array, each coil has its own such profile as shown in Figure **2.11**.

If several coils measure the same signal simultaneously, each one contains a distinct description of that signal which depends on its unique sensitivity profile. This is equivalent to obtaining multiple observations of the NMR signal simultaneously, which implies the possibility of reducing scan time in Fourier imaging without increasing the k-space sampling rate (Pruessmann et al., 1999; Pruessmann et al., 2006). Conceptually this is accomplished by replacing

some number of gradient encoding steps with spatial encoding based on coil sensitivity profiles.

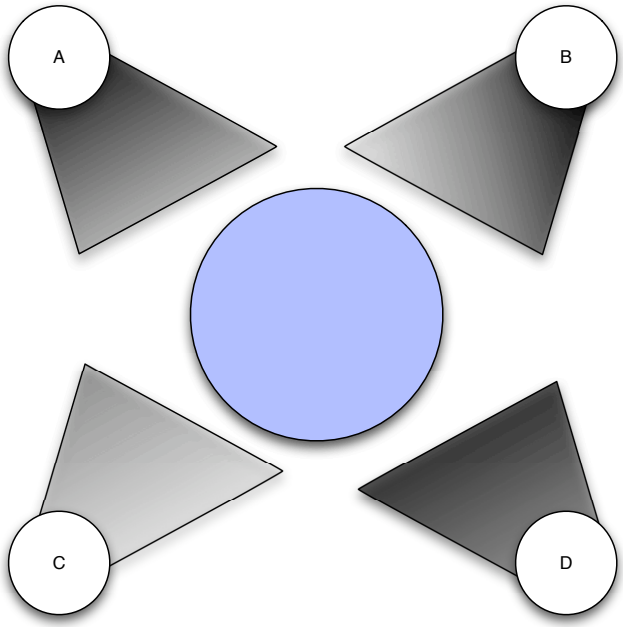

Figure 2.11: An array or receiver coils, each with its own sensitivity profile.

Reducing the number of gradient encoding steps has several uses, including reducing the echo train lengths, which in turn reduces magnetic susceptibility effects. As shown in Figure 2.12, parallel imaging methods can also increase image resolution or the field of view while maintaining a constant scan time, or reduce acoustic noise from gradient switching in echo train sequences (Pruessmann et al., 1999; Golay et al, 2002; de Zwart et al., 2006).

Though the original concepts of parallel MRI were introduced in 1980s (Carlson, Hutchinson et al., Kelton et al.) and early 1990s (Kwiat et al., Carlson et al., Ra et al.), it wasn't until 1997 that Sodickson et al., first reported successful

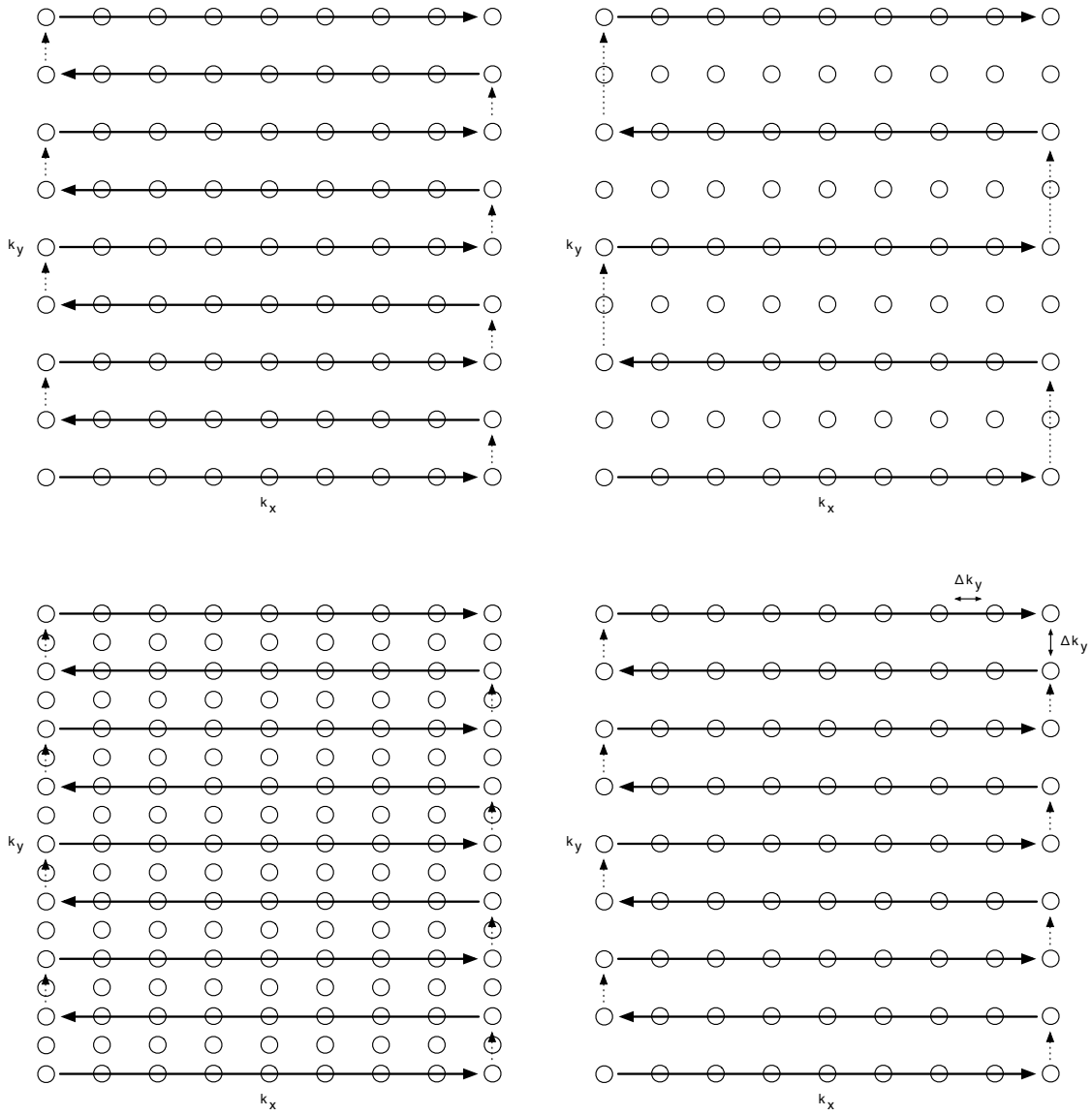

Figure 2.12: k-space trajectories for(a) standard 2D-EPI and undersampled k-space trajectory with R = 2 for (b) Scan time reduction: the number of phase encoding steps and the readout time are halved. (c) Resolution increase: the number of phase encoding steps remains the same as in the full FOV case, but the number of lines in the phase encoding direction are doubled while the limits of k-space remain the same. (d) Field of view increase. The number of phase encoding steps and lines remains the same as in (a), but the spacing between the lines has been halved to double the FOV in the phase encoding direction.

reductions in scan time using parallel receivers using SMASH (SiMultaneous Acquisition of Spatial Harmonics). Since then, many parallel imaging techniques have been been developed. Ultimately, the goal of all parallel imaging methods is to encode distinct signal information in multiple receiver coils in parallel, and then to combine that information into a single image. Here we focus on the Sensitivity Encoding (SENSE) approach to parallel imaging (Pruessmann et al., 1999).

9.2. Spatial Encoding with Parallel Imaging

A measurement with a homogeneously sensitive coil is given by:

$$d_\kappa = \int \rho(\boldsymbol{r})\, e^{i\boldsymbol{k}_\kappa \boldsymbol{r}} d\boldsymbol{r} \tag{2.52}$$

The result is a Fourier transform of $\boldsymbol{\rho}$ at $\boldsymbol{r}$, represented as a single point in k-space (a Dirac peak at $\boldsymbol{k}_\kappa$), where $\boldsymbol{k}_\kappa$ describes the κ-th plane-wave encoding[14]. (Pruessmann et al., 2006). This is essentially Eq. 2.35, where $\rho(\boldsymbol{r})$ has replaced $\rho_M(x, y)$ and $\boldsymbol{k}_\kappa$ has replaced the various gradient encoding terms. In parallel imaging, this encoding equation becomes

$$d_{\gamma,\kappa} = \int \rho(\boldsymbol{r})\, \boldsymbol{s}_\gamma(\boldsymbol{r})\, e^{i\boldsymbol{k}_\kappa \boldsymbol{r}} d\boldsymbol{r} \tag{2.53}$$

[14] Here the term “plane wave encoding” refers to a distinct combination of frequency and phase encoding gradients. In this framework, the frequency and phase encoding represent various combinations of plane-wave modulations of the transverse magnetization and need not be written separately.

Where $\boldsymbol{s}_\gamma(\boldsymbol{r})$ denotes complex-valued, spatially varying coil sensitivity. This leads to a hybrid encoding basis:

$$enc_{\gamma,\kappa}(\boldsymbol{r}) = \boldsymbol{s}_\gamma(\boldsymbol{r})\, e^{i\boldsymbol{k}_\kappa \boldsymbol{r}} \tag{2.54}$$

In which $s_\gamma(\boldsymbol{r})$ represents spatial encoding based on coil sensitivity profiles and $e^{i\boldsymbol{k}_\kappa \boldsymbol{r}}$ represents gradient encoding based on the relative frequency and phase of local spins. If the sensitivity profile for one coil is s_γ, then a sensitivity matrix $S_{\gamma,\rho}$ can be defined:

$$S_{\gamma,\rho} = s_\gamma(\boldsymbol{r}_\rho) \tag{2.55}$$

where the subscripts γ and ρ count the coils and the superimposed pixels, $\boldsymbol{r}_\rho$ denotes the position of the pixel ρ, and s_γ is the sensitivity profile of coil γ. The size of $S_{\gamma,\rho}$ is $n_C \times n_P$ where n_p is the number of pixels superimposed and n_C the number of coils used (Pruessmann et al., 1999; Pruessmann et al., 2006). Replacing the single coil sensitivity profile in Eq. 2.53 with the sensitivity matrix in Eq. 2.55, the encoding equation becomes

$$d_{\gamma,\kappa} = \int \rho(\boldsymbol{r})\, enc_{\gamma,\kappa}(\boldsymbol{r})\, d\boldsymbol{r} \tag{2.56}$$

Thus, with an array of coils, several encodings may be performed at once (Pruessmann et al., 1999)[15]. When image information is partly encoded in coil sensitivity, the total number of gradient encoding steps required to sample a volume of interest can be reduced by an amount R equal to or less than the number of coils in the array. In the case of pure Cartesian sampling, the discrete Fourier transform (DFT) can still be used to reconstruct the final image. Since the methods described in this work -- and a majority of fMRI studies in general -- use Cartesian sampling, we now restrict our discussion to that special case.

When SENSE acceleration is used to decrease the readout length in an echo train pulse sequence, the distance between sampling positions in k-space is increased while the maximum k-values are maintained. According to Eqs. 2.49.1-2, reducing the sampling density (increasing Δk) results in a reduction of the FOV, causing R-fold aliasing in the resulting single-coil images due to violation of the sampling theorem. Figure 2.13 shows aliasing due to undersampling in the phase encoding direction.

9.3. Reconstruction of Sensitivity Encoded Images

After hybrid encoding, the aliased single-coil images must be “unfolded” and combined into a single, full field-of-view image. Consider the vector $\boldsymbol{a}$, which

---

[15] A consequence of hybrid encoding over pure gradient encoding is that hybrid encoding functions are no longer pure plane waves, but now plane waves multiplied by coil sensitivity. They can no longer be represented by Dirac peaks in k-space and no longer yield individual k-space samples. Instead, such encodings are weighted integral of the data from a certain k-space neighborhood, and the encoding operation can no longer be interpreted as sampling the Fourier transform of $\rho_M(x, y)$, and in the case of arbitrary k-space sampling, image reconstruction can no longer be accomplished by a standard Fourier transform (Pruessmann et al., 2006)

contains the complex image values of a chosen pixel in the aliased coil images. The sensitivity matrix, $S_{\gamma,\rho}$ contains the coil sensitivities at each point and can be used to calculate the unfolding matrix U:

$$U = (S^H \Psi^{-1} S)^{-1} S^H \Psi^{-1} \tag{2.57}$$

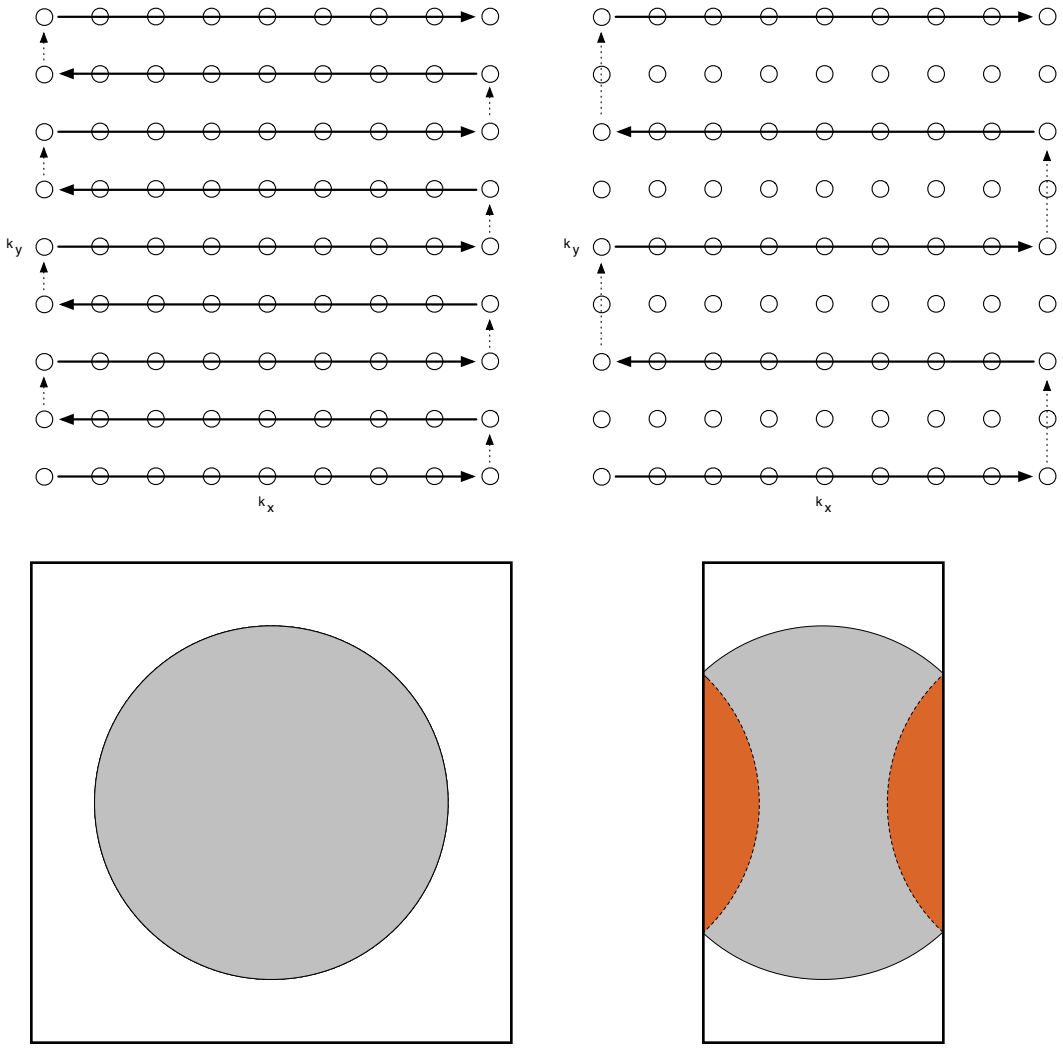

Figure 2.13: (a) Full sampling of k-space results in a full FOV image. (b) Undersampling of k-space results in an aliased image.

Where superscript H indicates the transposed complex conjugate, and Ψ is the $n_C \times n_C$ receiver noise matrix which describes the levels and correlation of noise in the receiver channels (Pruessmann et al., 1999). Signal separation is performed by

$$\boldsymbol{v} = U\boldsymbol{a} \tag{2.58}$$

Where the resulting vector $\boldsymbol{v}$ has length n_P and contains separated pixel values for the originally superimposed positions. By repeating this procedure for each pixel in the reduced FOV, a non-aliased full FOV image is obtained. Unfolding in this way is possible only when the number of pixels to be separated is fewer than the total number of coil elements ($n_P < n_C$).

In most cases with 2D imaging, undersampling is beneficial only in the phase encoding direction. However, 3D imaging techniques using two phase encoding directions (such as 3D-FFE and 3D-PRESTO) benefit from the ability to combine acceleration in flexible manner across both phase encoding directions (Weiger et al., 2002). The case of two dimensional SENSE acceleration in 3D imaging with two phase encoding directions is presented in detail in Chapter IV.

9.4. Noise in Sensitivity Encoded Images

SENSE images are affected by both noise in the sampled data and noise in the coil sensitivity data. With multiple receiver coils, the entries in the noise

correlation matrix Ψvary from channel to channel. There is also noise correlation between samples taken simultaneously (Pruessmann et al., 1999). The reconstruction process can introduce additional noise correlation between pixels in the unfolded image. The ratio of noise levels obtained in a voxel acquired with full Fourier encoding compare to reduced SENSE encoding is given by:

$$\frac{\sqrt{X_{\rho,\rho}^{reduced}}}{\sqrt{X_{\rho,\rho}^{full}}} = \sqrt{R}\,\sqrt{[(S^H\,\Psi^{-1}\,S)^{-1}]_{\rho,\rho}(S^H\,\Psi^{-1}\,S)_{\rho,\rho}} \tag{2.59}$$

Where S is the sensitivity matrix, R is the undersampling factor, and the subscript ρ denotes the aliased replicate number for a given pixel (Pruessmann et al., 1999). The rightmost square root expression above strongly depends on coil geometry and this is called the local *geometry factor* (*g*), which is always at least equal to one:

$$g_\rho = \sqrt{[(S^H\Psi^{-1}S)^{-1}]_{\rho,\rho}(S^H\Psi^{-1}S)_{\rho,\rho}} \geq 1 \tag{2.60}$$

Therefore

$$SNR_\rho^{reduced} = \frac{SNR_\rho^{full}}{g_\rho\sqrt{R}} \tag{2.61}$$

Conceptually, the geometry factor describes the ability of the coil array to separate pixels superimposed by aliasing. Thus the SNR in an image acquired with rate-R SENSE acceleration is bounded by the square root of the reduction factor in the ideal case ($g = 1$) and is further reduced when $g > 1$. Increasing the

acceleration factor R causes deteriorating conditioning of the unfolding problem, which is characterized by growing geometry factors. Detailed characterization of the geometry factor and associated effects on temporal signal stability are considered in the case of (a) one-dimensional acceleration in 2D-EPI, and (b) two-dimensional acceleration in 3D-FFE and 3D-PRESTO, in Chapters III and IV, respectively.

9.5. Parallel Imaging at High FIeld

Parallel imaging methods enjoy a number of benefits at high field. In general, the higher baseline SNR provided by high field scanners means increased flexibility in the ability of SENSE to achieve shorter acquisition time, higher resolution, greater coverage, more repetitions, or other desired benefits with relatively reduced impact on the ultimate SNR (Wiesinger et al., 2006). More subtly, since resonance frequencies increase at higher fields according to the Larmor equation, the wavelength RF excitation pulses must decrease to match. While this presents issues related to energy deposition and B1 inhomogeneity (Vaughan et al.,2003; Bandettini, 2007), it also improves sensitivity encoding by generating coil sensitivity maps which are more distinct from one another and are therefore more effective for signal separation (Wiesinger et al., 2006; Pruessmann et al., 2006). This is reflected in higher achievable acceleration factors with lower geometry factors. Consequently, parallel acquisition methods are expected to be a critical part of fMRI imaging as field strengths increase.

10. Summary

High magnetic fields provide theoretical benefits in SNR and BOLD contrast but also introduce technical issues, including increased bulk magnetic susceptibility effects, RF power deposition, and physiological noise effects. These issues are especially pronounced in techniques like single-shot gradient echo EPI which are popular for functional MRI at lower field strengths. The combination of these factors has thus far prevented single-shot methods from fully achieving the theoretical benefits of high field imaging.

Multi-shot gradient echo 3D imaging techniques such as 3D-FFE and 3D-PRESTO present reduced sensitivity to off-resonance effects at the cost of reduced raw signal and increased sensitivity to temporal instabilities. Though these 3D sequences feature theoretical SNR benefits compared to 2D-EPI in certain situations, it is not yet clear whether these theoretical benefits are realized in practical high field imaging scenarios.

Parallel imaging techniques such as Sensitivity Encoding can alleviate a number of the technical issues inherent to high field imaging at a cost to SNR that depends on the degree of reduction and the local geometry factor. 2D-EPI acquisitions can apply SENSE in a single phase encoding direction, while 3D acquisitions can accelerate both phase encoding directions independently.

The role of parallel acquisition techniques in functional imaging methods is expected to increase with field strength. Indeed, parallel acquisition with receiver coil arrays may be the only way to achieve the theoretical benefits of fMRI at high field. While the effects of parallel imaging on individual images are well-

characterized, a detailed description of the effects of parallel imaging on high field fMRI time series data, in particular with regard to the differences between 2D and 3D acquisitions, is currently lacking but is clearly needed. The work presented in the following chapters aims to address these issues with the ultimate goal of improving methods for functional MRI at high field.

CHAPTER III

EFFECTS OF SENSITIVITY ENCODING ON TEMPORAL SIGNAL STABILITY AND FMRI AT 7T

1. Introduction

High field MRI scanners operating at 7T or above are finding increasing use in studies of brain function. In theory, increasing the main magnetic field (B_0) leads to increases in the signal-to-noise ratio (SNR) of MR images and to increased contrast from blood oxygen level dependent (BOLD) effects in functional MRI (fMRI). At the same time, magnetic field inhomogeneities and magnetic susceptibility gradients are also increased (Vaughan et al., 2001; de Zwart et al., 2006; Pruessmann, 2006). During long acquisition times like those required for echo-planar fMRI, magnetic field inhomogeneities cause local spins to become out of phase. This results in undesirable magnetic susceptibility effects (MSE) such as signal dropout and image distortions.

A limitation in many fMRI studies is the contribution of physiological noise to the variation in a series of images. This noise originates from physiological processes in living subjects and differs from thermal noise in that it cannot be fully modeled simply by adding a fixed amount of variance to the images. Instead, physiological noise modulates the MR signal, scales with image intensity, and becomes more severe as field strength increases (Kruger and Glover, 2001**;** Triantafyllou et al., 2005). At high field, physiological noise may be the dominant source of temporal signal variation in an fMRI data set, often

causing signal changes on the same order of magnitude as those related to brain function (Van de Moortele et al., 2002; Triantafyllou et al., 2005).

One type of physiological noise originates from respiratory variations and causes susceptibility-based fluctuations in the magnetic field (Raj et al., 2000; Raj et al., 2001; Van de Moortele et al., 2002). Magnetic susceptibility effects depend not only on the strength of the underlying field, but also on the acquisition time of the MR data. More specifically, their severity depends upon the duration over which spin phase evolves during the traversal of k-space. One way to reduce the severity of MSE is to shorten the data acquisition window. Parallel imaging techniques such as Sensitivity Encoding (SENSE) accelerate data acquisition and reduce imaging time by collecting under-sampled (aliased) data from multiple receiver coils simultaneously. SENSE requires a full field of view (FOV) reference scan and accomplishes the unfolding of aliased single-coil images in image space (Pruessmann et al., 1999; Wiesinger et al., 2006).

In general, high field imaging and parallel acquisition techniques complement one another well (Wiesinger et al., 2006). Applying SENSE can increase the image matrix size without changing the readout period, or shorten acquisition time by reducing the echo train length. Because k-space is traversed more quickly with SENSE, MSE such as distortion are reduced in the direction of acceleration (usually the phase-encoding direction). However, the lower sampling density of SENSE acquisitions relative to full Fourier encoding leads to an SNR penalty that depends on the acceleration factor *R*. Moreover, the SENSE reconstruction algorithm introduces spatially varying noise amplification based on

the sensitivity profiles and spatial locations of individual receive coil elements (Pruessmann et al., 1999; Ohliger et al., 2003; Wiesinger et al., 2006).

On the other hand, higher magnetic fields provide increased baseline SNR levels which offset this penalty, and spatial encoding benefits based on high field RF electrodynamics make parallel imaging techniques more robust at 7T compared to 3T and below (Wiesinger et al., 2006). The interaction between high field imaging and parallel acquisition techniques is especially relevant for fMRI, as the SENSE-related SNR penalty limits the temporal signal to noise ratio (TSNR) of a time series, which in turn determines fMRI sensitivity.

Previous work suggests that the SNR penalty incurred with SENSE does not lead to an equal loss in fMRI sensitivity, and that this difference may depend on the relative contributions of thermal and physiological noise to the temporal variance of the time series (Preibisch et al., 2003; de Zwart et al., 2006). The statistical significance of brain activation in BOLD fMRI experiments is not directly derived from the signal and noise amplitudes; instead it depends on the difference in signals between two distinct states compared with the stability of the signal over time (de Zwart et al., 2006). When physiological noise is a major contributor to temporal signal variance at high field, the penalty for the use of SENSE in fMRI depends on the relative contribution of physiological noise to the overall temporal standard deviation. While it is clear that physiological noise dominates the temporal variance at high field in standard non-accelerated (R=1) gradient-echo EPI, potential interactions between SENSE acceleration and physiological noise effects due to susceptibility changes (Raj et al., 2001; Van de

Moortele et al., 2002) or other mechanisms (Kruger and Glover et al., 2001; Triantafyllou et al., 2005), are less clear. The manner in which physiological noise is partitioned across independent receiver channels is also poorly understood.

In light of the challenges facing high field fMRI studies, especially those performed with single-shot gradient-echo EPI, we aim to characterize the relationships between physiological noise, SENSE acceleration, and magnetic susceptibility effects in a simple high-resolution fMRI experiment at 7T. The ultimate goal of this and related work is to develop a method for selecting sequence parameters which provides an optimal trade-off between physiological noise, image distortion, resolution, and temporal signal stability for specific high field fMRI applications.

2. Theory

In Chapter II we introduced the spatial and temporal signal to noise ratios:

$$SNR_0 = \frac{\overline{S}}{\sigma_T} \tag{3.1}$$

$$TSNR = \frac{\overline{S}}{\sqrt{\sigma_S^2 + \sigma_T^2 + \sigma_P^2}} \tag{3.2}$$

Here we assume negligible scanner-related instabilities ($\sigma_S = 0$), and in a phantom, no physiological noise ($\sigma_P = 0$). Provided maps of the mean signal ($\overline{S}$) and *TSNR*, the map of temporal variance for images of a phantom is given by:

$$\sigma_{T_{phantom}} = \frac{\overline{S}_{phantom}}{TSNR_{phantom}} \tag{3.3}$$

For humans, physiological noise is a major source of temporal signal variance. Assuming negligible scanner-related instabilities compared to physiological and intrinsic thermal noise ($\sigma_S = 0$), we have:

$$TSNR_{human} = \frac{\overline{S}_{human}}{\sqrt{\sigma^2_{T_{human}} + \sigma^2_P}} \tag{3.4}$$

Given an estimate of $\sigma_{T_{human}}$, a map of physiological noise, σ_P, may be calculated from:

$$\sigma_P = \sqrt{\left(\frac{\overline{S}_{human}}{TSNR_{human}}\right)^2 - \sigma^2_{T_{human}}} \tag{3.5}$$

Though it may not be possible to obtain a precise map of $\sigma_{T_{human}}$, a reasonable approximation can be made using $\sigma_{T_{human}} = c \cdot \sigma_{T_{phantom}}$, where the constant *c* accounts for the differences in temperature and coil loading and receiver gains between human and phantom, provided the human and phantom scans are acquired at a similar bandwidth. The constant *c* can be estimated from differences in variance between thermal noise dominated images in phantoms and humans, or special images acquired with a zero degree flip angle

(Triantafyllou et al., 2005). Thus the estimated map of physiological noise in humans becomes:

$$\sigma_P = \sqrt{\left(\frac{\overline{S}_{human}}{TSNR_{human}}\right)^2 - \left(c \cdot \sigma_{T_{phantom}}\right)^2} \tag{3.6}$$

As discussed in chapter II, Sensitivity Encoding accelerates data acquisition by collecting under-sampled data from multiple receiver coils in parallel. For a given bandwidth and spatial resolution, the application of SENSE acceleration factor R leads to an R-fold decrease in signal intensity and a $\sqrt{R}$ decrease in the intrinsic noise in the acquired data, along with an increase in image noise that depends on coil geometry, the number of receive elements in the coil array, and a combination of the receive coil sensitivity profiles. The net effect is an increase in intrinsic image variance (de Zwart et al., 2006):

$$\sigma_{T_{SENSE}} = g \cdot \sqrt{R} \cdot \sigma_{T_{full}} \tag{3.7}$$

Where $\sigma_{T_{full}}$ is the thermal noise for an acquisition without acceleration (R = 1), R is the SENSE acceleration factor, and *g* is the local geometry factor, a measure of parallel imaging performance which describes noise amplification related to conditioning of the aliased image unfolding operation and reflects coil sensitivity profile accuracy (Wiesinger et al., 2006). Now we have:

$$\sigma_{T_{phantom_{SENSE}}} = \frac{\overline{S}_{phantom_{SENSE}}}{g \cdot \sqrt{R} \cdot TSNR_{phantom_{SENSE}}} \tag{3.8}$$

Note $\sigma_{T_{phantom_{SENSE}}} \approx \sigma_{T_{phantom_{full}}}$ when R = 1, since *g* ≈1 at all points in that case. Now equations 3.4 and 3.5 become:

$$TSNR_{human_{SENSE}} = \frac{\overline{S}_{human}}{\sqrt{\left(g_{human} \cdot \sqrt{R} \cdot c \cdot \sigma_{T_{phantom_{full}}}\right)^2 + \sigma_P^2}} \tag{3.9}$$

$$\sigma_P = \sqrt{\left(\frac{\overline{S}_{human}}{TSNR_{human_{SENSE}}}\right)^2 - \left(g_{human} \cdot \sqrt{R} \cdot c \cdot \sigma_{T_{phantom_{full}}}\right)^2} \tag{3.10}$$

Equation 3.10 characterizes the SNR behavior in SENSE data as a combination of several mechanisms: signal modulations and magnetic susceptibility effects related to physiological processes (σ_P), noise due to reduced overall data acquisition and reduced intrinsic signal averaging (R), and noise amplification related to the operations of unfolding the aliased image and to coil configuration, the shape and size of the imaged object, the imaging volume, and noise covariance in the imaging data (*g*).

de Zwart et al. (2002) provide a formulation of noise in SENSE images which suggests, in the case of perfect image reconstruction (i.e., *g* = 1 at every pixel), no interaction between physiological noise and R. In practice, however, *g* > 1 at almost all points in a data volume and heavily influences noise in SENSE

image reconstruction. Specifically, for a reconstruction matrix F, the noise covariance (X) of the resulting image is given by:

$$X = F\Psi F^{H} \tag{3.11}$$

Where Ψ is the noise covariance matrix of the input data, the superscript H indicates the complex conjugate transpose, and the diagonal elements of X are the noise variances in individual pixels (Pruessmann, 2006). Reconstruction matrices are derived from the combination of individual coil sensitivity profiles, which are based upon the physical magnetic field within the sample (Ohliger et al., 2003; Pruessmann, 2006; Wiesinger et al., 2006). Because the sensitivity profiles are based on the magnetic field, their accuracy is subject to inhomogeneities in B_0. Sensitivity profile errors cause ill-conditioning of the inverse unfolding and reconstruction problem and increase noise in the resulting image (Pruessmann, 2006). The severity and spatial extent of this phenomenon is reflected in the geometry factor, which is responsible for the majority of noise enhancements and image artifacts associated with higher acceleration factors.

Since the geometry factor is partly determined by the noise covariance matrix, which describes the time-averaged statistical properties of the noise in the receive coils, the noise amplitude received by individual coils, and noise correlation between coil pairs (Ohliger et al., 2003), and physiological noise effects modulate the magnetic field over space and time and can introduce signal intensity gradients in individual images as well as autocorrelation into voxel time

series (Raj et al., 2001; Murphy et al., 2007), we may expect physiological noise to influence SENSE reconstruction through the noise covariance matrix of the input data and the determination of coil sensitivity profiles. However, most existing methods for SENSE image reconstruction do not account for time variations in B_0 from physiological noise, tissue motion, and eddy currents (Pruessmann, 2006). Thus the extent to which which physiological noise effects interact with SENSE reconstruction in realistic imaging scenarios, especially those at high field where physiological noise is known to dominate temporal signal variance, is currently unclear.

3. Methods

Data were acquired with a single-shot, multi-slice gradient echo EPI sequence on a Philips Achieva 7T scanner with a 16 channel SENSE receive-only head coil with an outer quadrature transmit coil. Written consent was obtained from all subjects in a manner consistent with approved Vanderbilt University Medical Center IRB protocols. Head immobilization was achieved with foam pads, and subjects were asked to relax while in the scanner.

Subjects were presented with a flashing checkerboard stimulus (8Hz) in 24 second intervals ([on, off] x4). Each run was a total of 192 seconds in length, while resolution (1 x 1 x 2mm^3), field of view (192 x 192 x 18mm^3) and readout bandwidth (1280Hz) were fixed across all scans. Nine axial slice were collected with TR = 2000ms and TE = 25ms. The SENSE acceleration factor R was varied from 1-8 for each subject. Respiration and heart rate were monitored with

respiratory bellows and a pulse-oximeter, respectively. Five subjects were scanned.

For each subject and at each R, fMRI magnitude images and *g*-factor maps were reconstructed using the standard vendor-supplied SENSE reconstruction algorithms and were transferred from the scanner to MATLAB (The Mathworks Inc. Natik, MA) for analysis. The image time series was masked to exclude pixels outside of the brain. Mean signal and linear trends were removed on a voxel-by-voxel basis using the MATLAB detrending routine, and temporal SNR maps were generated for each time series by taking the mean value of each pixel divided by its standard deviation over time. Maps of physiological noise in humans were calculated according to equations 6 - 12.

Spatial and temporal processing and analyses were performed using SPM5 (Wellcome Department of Cognitive Neurology, London, UK). Data were slice-timing corrected using the first slice as the reference slice, then realigned to the first volume and normalized into SPM's standardized neuroanatomical space. Low frequency fluctuations were removed with the SPM default high-pass filter which removes frequency drifts with period greater than 128 seconds. Motion parameters were estimated and used as regressors during analysis. For each subject, statistical parametric maps of T-values were created ($p < 0.0001$). Geometry factor (*g*), the temporal signal-to-noise ratio (*TSNR*), residual variance in the time series, physiological noise (σ_P), and the distribution of T-values in active voxels were measured and compared across subjects and acquisitions.

4. Results

Figure 3.1 shows geometry factor maps for one representative phantom (a) and one representative human (b) for R = 1-8. The spatial distribution of geometry factors is similar between the two, with differences owing to due to the different sizes and relative locations of the object within the coil array. The geometry factor does not become much greater than 1 anywhere in either the phantom or the human until $R > 5$. At this point and beyond, "hotspots" (areas of high *g*) occur in areas where the coil sensitivity profiles are unreliable, while “coldspots” (areas of low *g*) are visible on edge areas near receive coil elements.

Figure 3.2 shows the distribution of geometry factors in a central ROI (21x21 pixels), averaged across all humans (black) and across all phantoms (red) for R = 1-8. As Figure 3.1 suggests, the distribution of *g*-factors is nearly identical for humans and phantoms through R = 4. At R = 5 and beyond, *g* grows significantly, achieving higher maximum values in phantoms. On this and all other box plots shown here, the central horizontal line in each box represents the median, the top and bottom bounds of the box represent the 75th and 25th percentiles, respectively, and the whiskers represent 1.5 times the interquartile range. Outlier points beyond the whiskers are marked as crosses of the appropriate color.

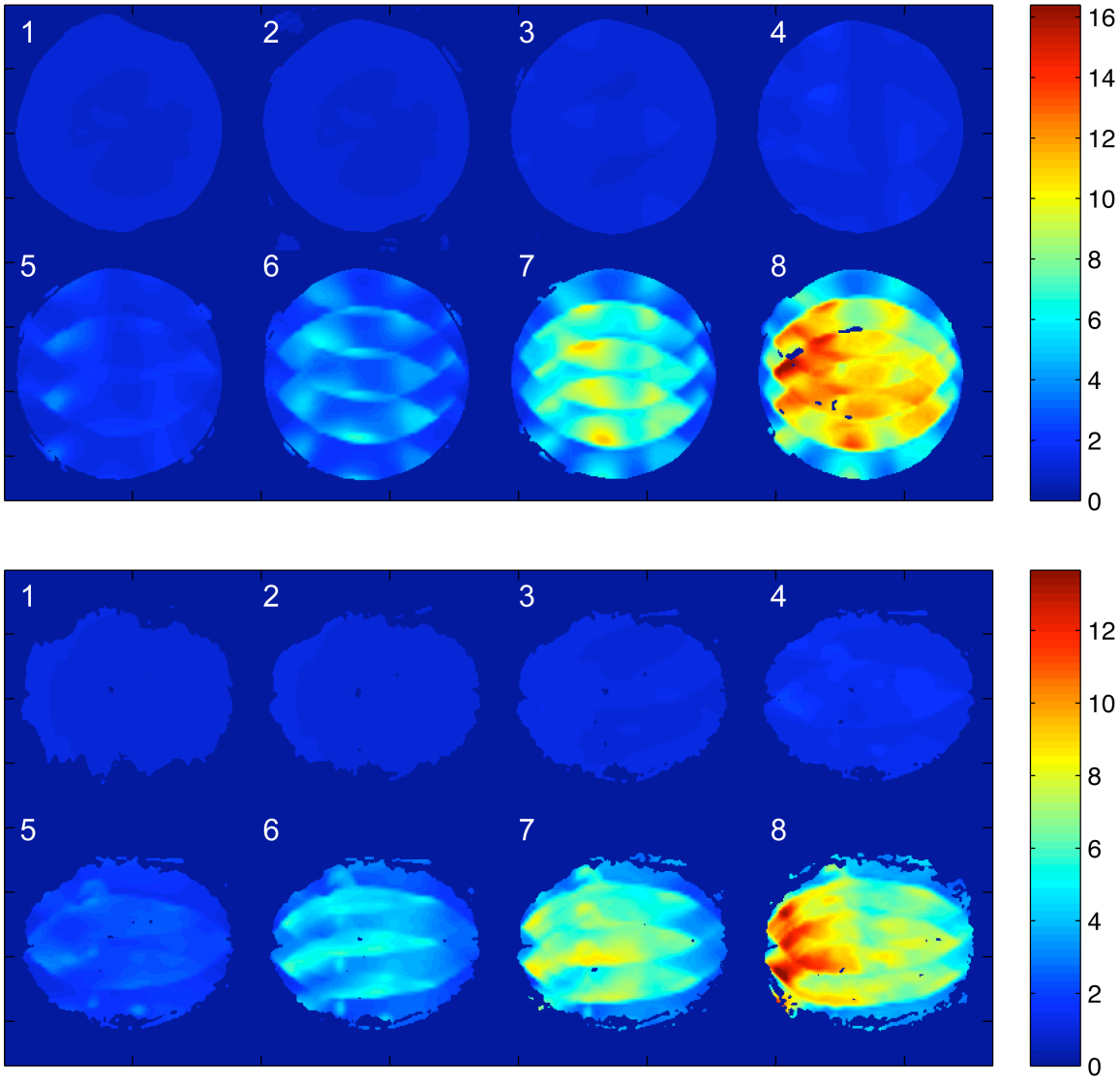

Figure 3.1. Maps of geometry factor (*g*) for a representative phantom (top) and human (bottom) for R = 1-8 (white numbers). The geometry factor does not become much greater than 1 anywhere until R > 5.

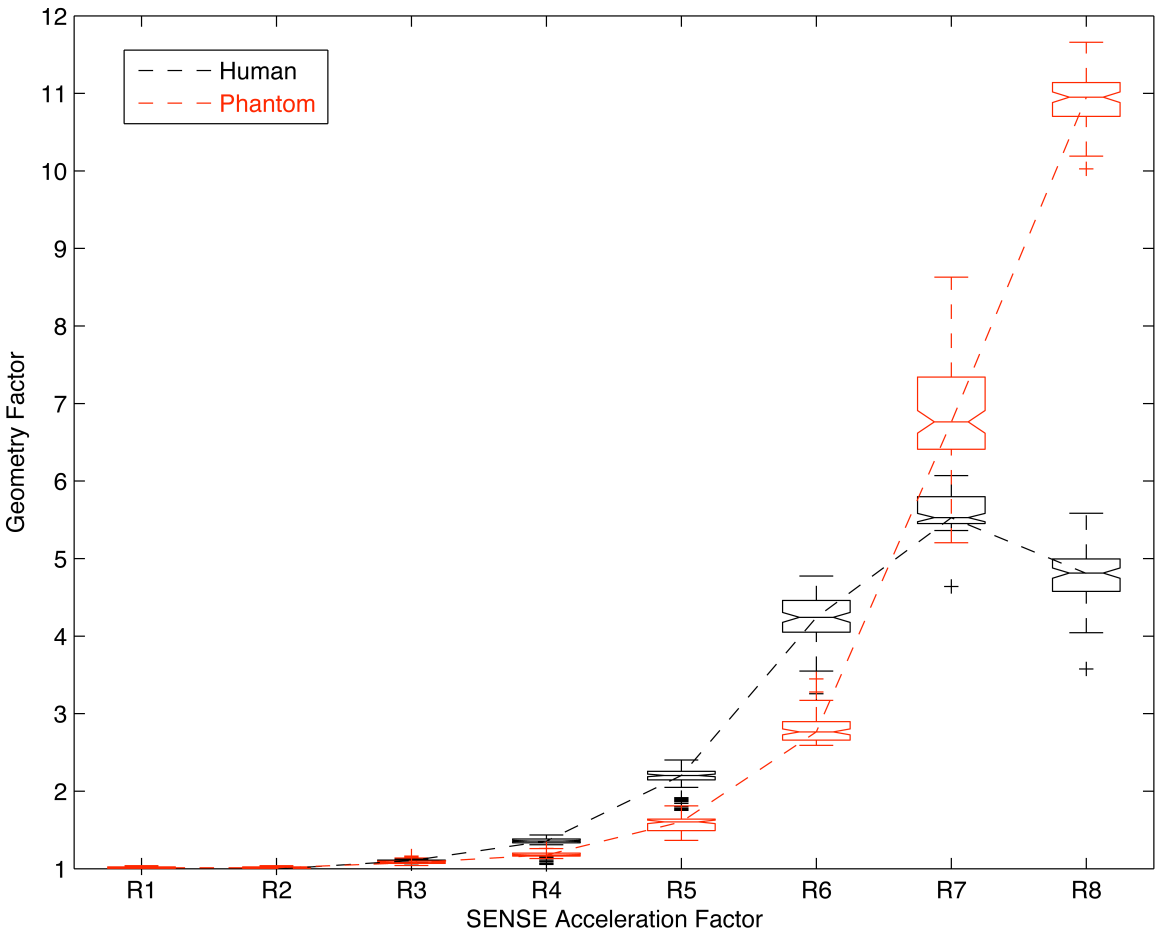

Figure 3.2. Distribution of *g*-factors within a central ROI (21x21 pixels), averaged across all humans (black) and phantoms (red) for each R. The distribution of *g*-factors is nearly identical for humans and phantoms until R > 4. Humans show slightly larger *g*-factors between R = 4 and R = 6, but phantoms clearly attain higher maximum *g*-factors at the highest R values as shown in Fig. 3.1.

Figure 3.3 shows maps of the temporal signal to noise ratio for one representative phantom (a) and one representative subject (b) for R = 1-8. The spatial distribution of TSNR matches closely with that of the *g*-factors observed in Figure 3.1. One notable exception is lower TSNR in the ventricles, CSF, and some areas in the gray matter on the human data. This is expected because physiological noise due to respiration and blood pulsation from cardiac processes is known to be high these areas. Meanwhile, white matter, which has been

shown to exhibit relatively less physiological noise (Triantafyllou et al., 2005), has higher TSNR. Reductions in distortion are evident from R = 1-5 on both humans and phantoms.

Figure 3.4 shows a box plot of the distribution of TSNR in (a) a central ROI (21x21 pixels) and (b) an off-center ROI (21x21 pixels) chosen specifically to have high *g*-factors across all R , averaged across all humans (black) and across all phantoms (red) for R = 1-8. The dashed curves represent the theoretical $\frac{1}{g \cdot \sqrt{R}}$, based on the median *g*-factor within the ROI using measured *g* from humans and phantoms as appropriate.

TSNR tends to follow the shape of the theoretical curve, but with slightly higher values than predicted relative to the TSNR values for R = 1 in both humans and phantoms. The ROI selected to have larger *g*-factors (b), demonstrates TSNR behavior that more closely matches the theoretical relationship for both humans and phantoms. That is, when *g* is large, it dominates TSNR as seen in Figure 3.3.

We observe median TSNR values of approximately three-to-four times larger in phantoms than in humans until R > 6, at which point the difference becomes less pronounced. Physiological noise is expected to be the primary source of this difference, especially in the central ROI because it is located near the ventricle area where physiological noise is at its highest.

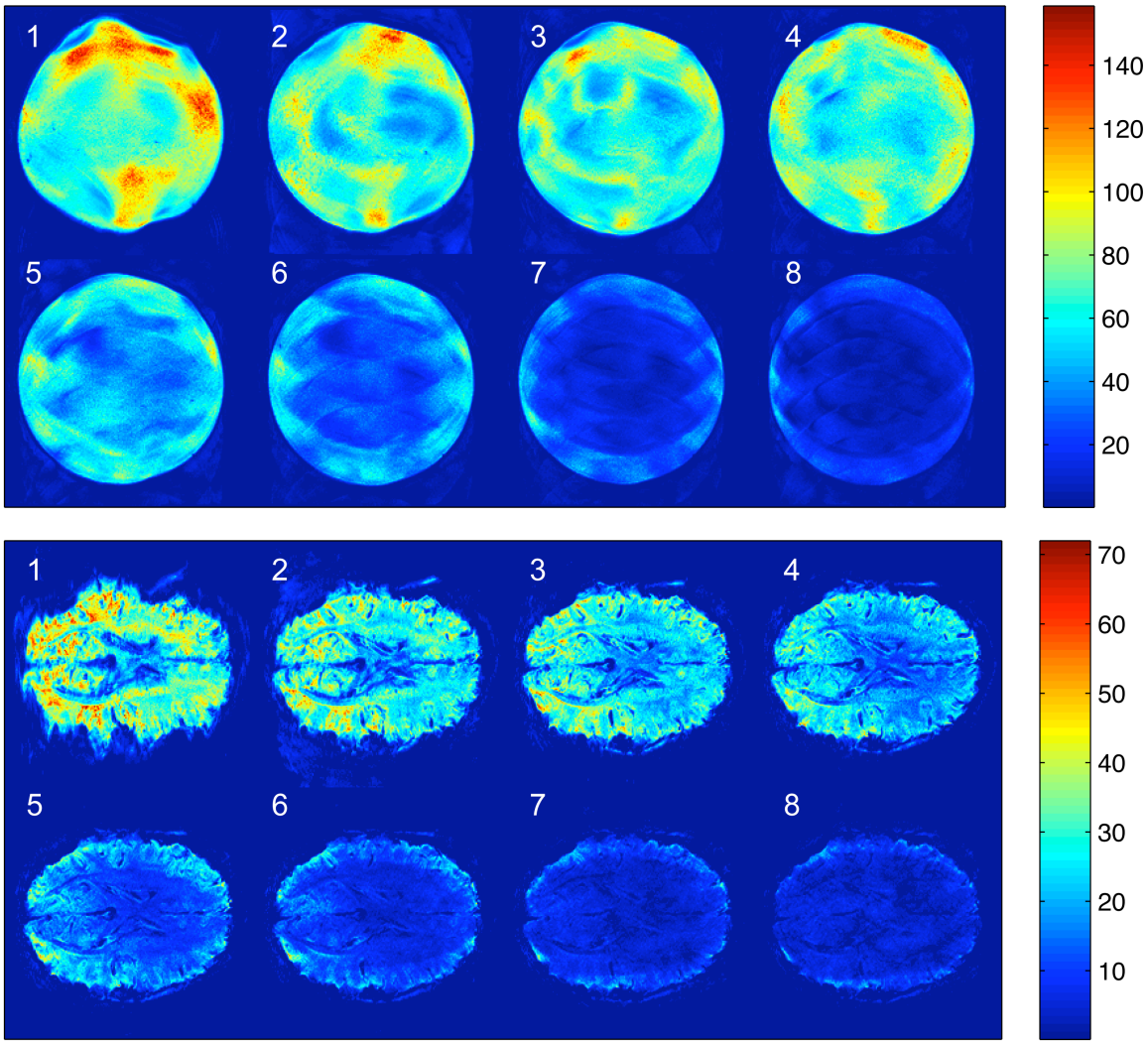

Figure 3.3. Maps of the temporal signal-to-noise ratio (TSNR) for one representative phantom (top) and human (bottom) for R = 1-8 (white numbers). TSNR decreases according to the increase in *g*-factor (see Fig. 3.1) and residual variance (see Fig. 3.5). In humans, TSNR is generally higher in white matter and lower in regions of physiological activity such as the ventricles, CSF, and gray matter. Reductions in distortion are evident as R increase from 1-5 on both the human and the phantom.

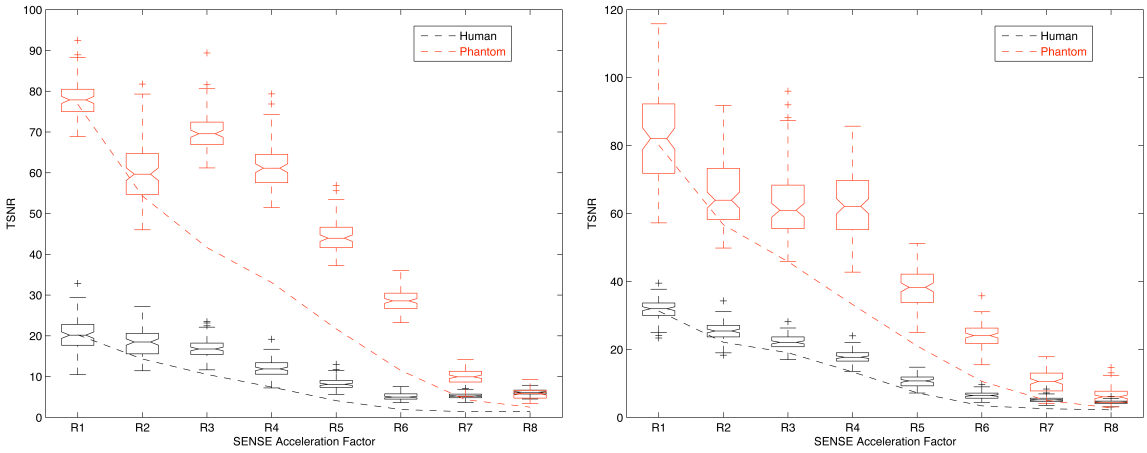

Figure 3.4. Temporal SNR within (left) a central ROI (21x21 pixels) and (right) an off-center ROI (21x21 pixels) specifically selected in an area of high *g* across all *R*, averaged across all humans (black) and phantoms (red) for each R. TSNR for the phantom is significantly greater than that of the human until around R = 7, with physiological noise being the primary cause of this difference. The dashed curves represent the theoretical $\frac{1}{g \cdot \sqrt{R}}$ behavior of TSNR based on the median *g*-factor within the ROI. These curves are not perfectly smooth because the median *g*-value do not always transition smoothly from one R value to the next.

Figure 3.5 shows the residual variance maps for phantoms and humans for R = 1-8. Residual variance maps are calculated by SPM as part of the general linear model analysis and represent all temporal variance in the fMRI time series that cannot be accounted for by the mean signal, the task, or any other regressors (such as motion). These maps of residual variance complement the TSNR maps in Figure 3.3. That is, areas with high residual variance generally reflect low TSNR, and vice versa.

In the human images, we observe large residual variance in the ventricles and CSF at R < 4, confirming the expectation that physiological noise is the primary source of temporal variance in humans at those R values. At R > 5, the

areas of high temporal variance resemble the *g*-factor maps shown in Figure 3.1 as expected.

Phantoms are have no physiological noise but still experience other forms of temporal variance. Here we observe low temporal variance until R > 5, at which point the residual variance maps begin to resemble the *g*-factor maps shown in Figure 3.1. The phantom images show central regions of higher variance relative to the rest of the image at R = 1-4. These areas of higher variance are not due to *g*, as Figure 3.1 shows that geometry factors are not much larger than 1 anywhere for phantoms or humans at R < 4. Instead, these may be caused by inhomogeneous B_1 excitation due to the dielectric effect present at high field strengths. Subtle dielectric effects are also visible on the human images, but are much smaller than the variance due to physiological noise at lower R. Note the different scales for human and phantom images. Color axes have been manually limited to reveal detail at lower R-values.

Figure 3.6 shows box plots of residual variance for (a) a central ROI (21x21 pixels) and (b) an off-center ROI (21x21 pixels) specifically selected in an area of low *g* across all R, averaged across all humans (black) and phantoms (red) for each R. The dashed curves represent the theoretical $g \cdot \sqrt{R}$ based on the median *g*-factor within the ROI.

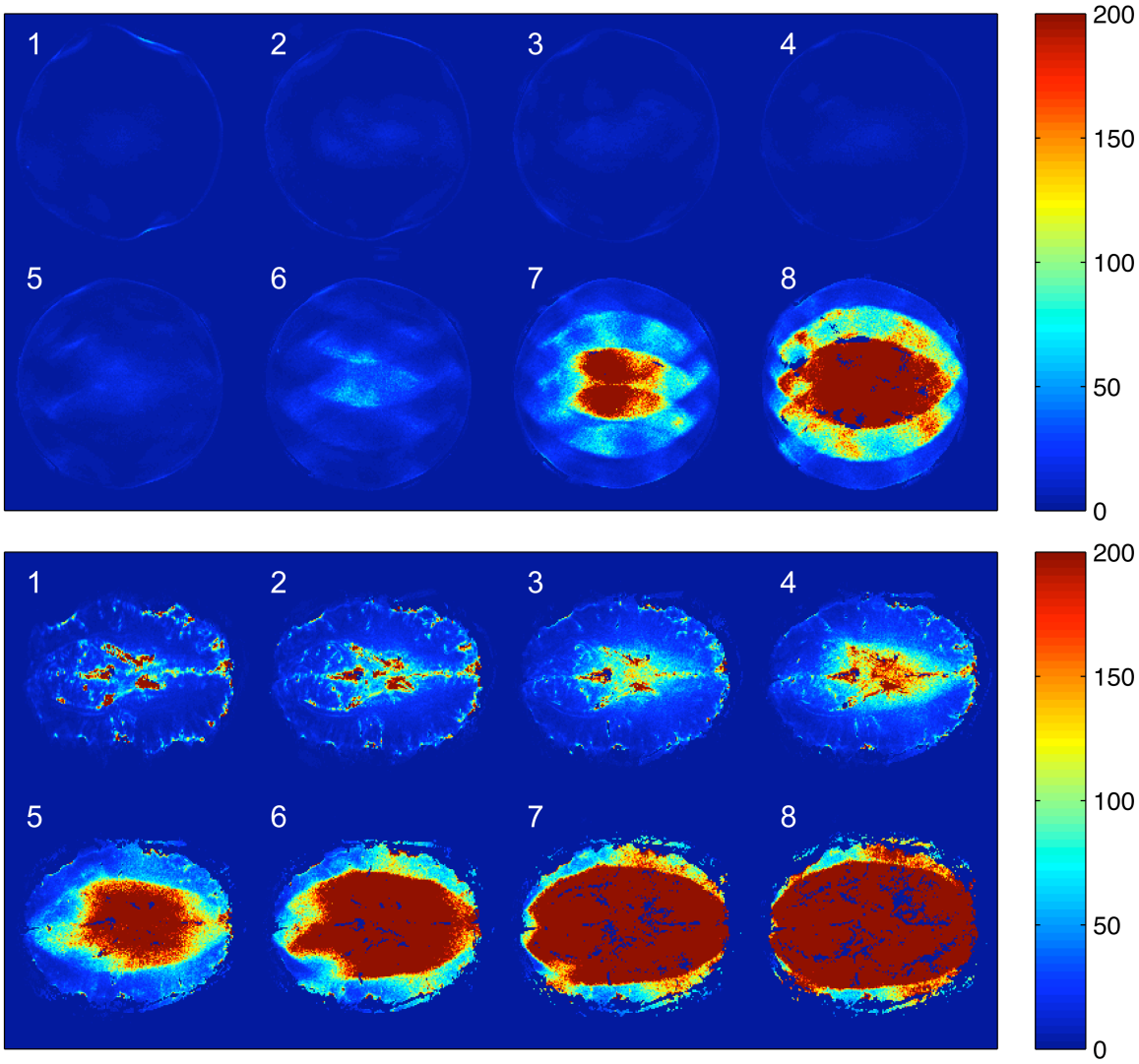

Figure 3.5. Maps of residual variance for one representative phantom (top) and human (human) for R = 1-8 (white numbers). Color axes have been manually limited to reveal more detail at low R values. In the human images, bright ventricles, CSF, and gray matter at R < 4 suggests physiological noise is the primary source of temporal variance in humans at those R values. At R > 5, the areas of high variance begin to resemble the *g*-factor maps seen in Fig. 3.1.

The median residual variance accords well with theory for humans and phantoms until R > 5, at which point the variance exceeds theoretical prediction. There are a number of outliers in the human data which correspond to the disproportionately high variance in the ventricles and cerebro-spinal fluid

(CSF) compared to the surrounding tissue, as observed in Figure 3.5. As R increases, the number of such outliers begins to decrease, representing a reduced contribution of physiological noise relative to that of SENSE-related noise to the total temporal variance. The residual variance is smaller in off-center ROI (b) because it is located away from the ventricles in humans, and in an area of low *g* in both humans and phantoms.

Figure 3.7 shows maps of the ratio of physiological noise to thermal noise in humans. As expected from the residual variance maps (see Fig. 3.5), we observe a high ratio of physiological to thermal noise at low R. The distribution of these values is consistent with expectations as gray matter, CSF, ventricles, and edges of the brain show the largest ratios of physiological to thermal noise. As R increases, we observe a steady decrease in contributions of physiological noise relative to thermal noise in agreement with the theoretical SENSE-related SNR penalty (Eq. 3.10).

Figure 3.8 shows box plots of the ratio of physiological to thermal noise for (a) a central ROI (21x21 pixels) and (b) an off-center ROI (21x21 pixels) chosen specifically to have low *g*-factors across all R, averaged across all humans (black) and across all phantoms (red) for R = 1-8. The dashed curves represent the theoretical $\frac{1}{g \cdot \sqrt{R}}$, based on the median *g*-factor within the ROI using measured *g* from humans and phantoms as appropriate. Median values for the relative contribution of physiological noise across all subjects were roughly 3-5 times that of thermal noise at lower R, and decreasing as R increases. Though there is no “physiological” noise in a phantom, phantoms do sometimes exhibit

slight temporal signal fluctuations from scanner instabilities, eddy currents, or B_1-related time-varying signal inhomogeneity. The red outlier points on these plots correspond to such effects, typically located on the edges of the phantom.

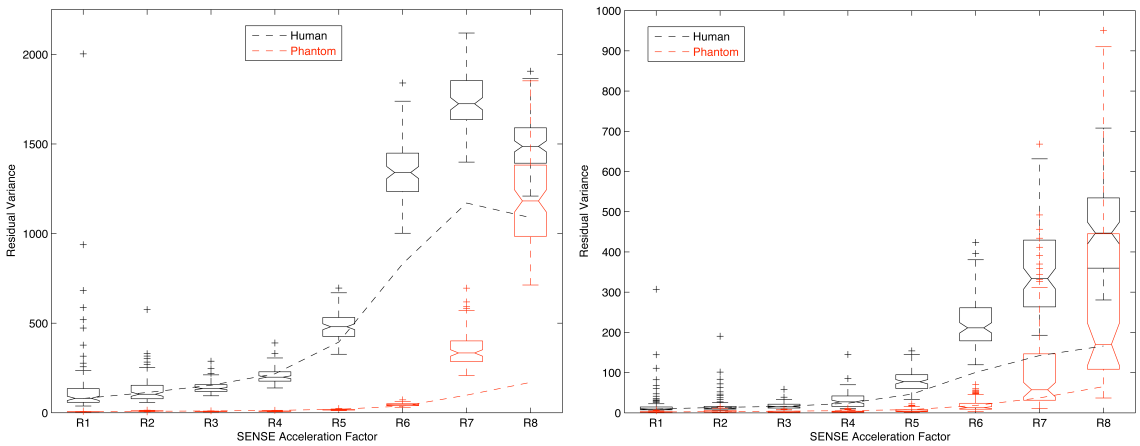

Figure 3.6. Residual variance within (left) a central ROI (21x21 pixels) and (right) an off-center ROI (21x21 pixels) specifically selected in an area of low *g* across all *R*, averaged across all humans (black) and phantoms (red) for each R. The dashed curves represent the theoretical $g \cdot \sqrt{R}$ based on the median *g*-factor within the ROI. Residual variance increases in the same manner for humans and phantoms, showing that the influence of physiological noise on the human data is not changing from one R value to the next. Instead, changes in *g* and R, which are roughly the same for humans and phantoms, dictate changes residual variance with R for both humans and phantoms.

Figure 3.9 shows the absolute contribution of physiological noise within (a) a central ROI (21x21 pixels) and (b) an off-center ROI (21x21 pixels) chosen specifically to have low *g*-factors across all R, averaged across all humans (black) and across all phantoms (red) for R = 1-8. The dashed curves represent the theoretical $\frac{1}{g \cdot \sqrt{R}}$, based on the median *g*-factor within the ROI. The absolute contribution of physiological noise does not demonstrate any significant relationship with R. Apparent decreases in human physiological noise at R = 6-8

are accompanied by apparent increases in phantom "physiological noise," and most likely represent slight errors in the calculation of the physiological noise maps as *g* becomes large. The red crosses represent outlier pixels on the phantom which exhibited significant temporal variability. The ROI in (b) is closer to the edge of the phantom, so the higher percentage of non-zero temporal fluctuations in that ROI is probably due to edge artifacts.

Figure 3.10 shows SPM-generated activation maps (red areas) overlaid onto anatomical slices for R = 1-8 for one representative subject. The degree of activation portrayed clearly decreases as R increases. Beyond R = 6, significant activation is no longer visible on this particular slice at this significance threshold ($p < 0.0001$). Also noteworthy is the pronounced decrease in distortion as SENSE acceleration increases through R = 5. Here R = 4 appears to represent the best compromise between activation, distortion, and SNR.

Figure 3.11 shows SPM-generated activation maps on the SPM "glass brain" which displays activation across all slices. The spatial patterns of activation are in agreement with Figure 3.10, though more activation is visible since here since all slices are taken into account.

Figure 3.12 shows box plots of T-statistics for a small ROI (7x7 pixels) over (a) an activated area in the visual cortex, and (b) an inactive area in white matter, averaged across subjects (black), together with the T-statistics for ROIs at the same coordinates in the phantoms (red) for R = 1-8. For the human data, the decrease in T-values in the activated ROI is consistent with $\frac{1}{g \cdot \sqrt{R}}$, while in the inactive white matter region there is no difference between T-values in the human

or the phantom. As expected, we observe median T-values of roughly zero in phantoms at both the location of “active” and “inactive” ROIs.

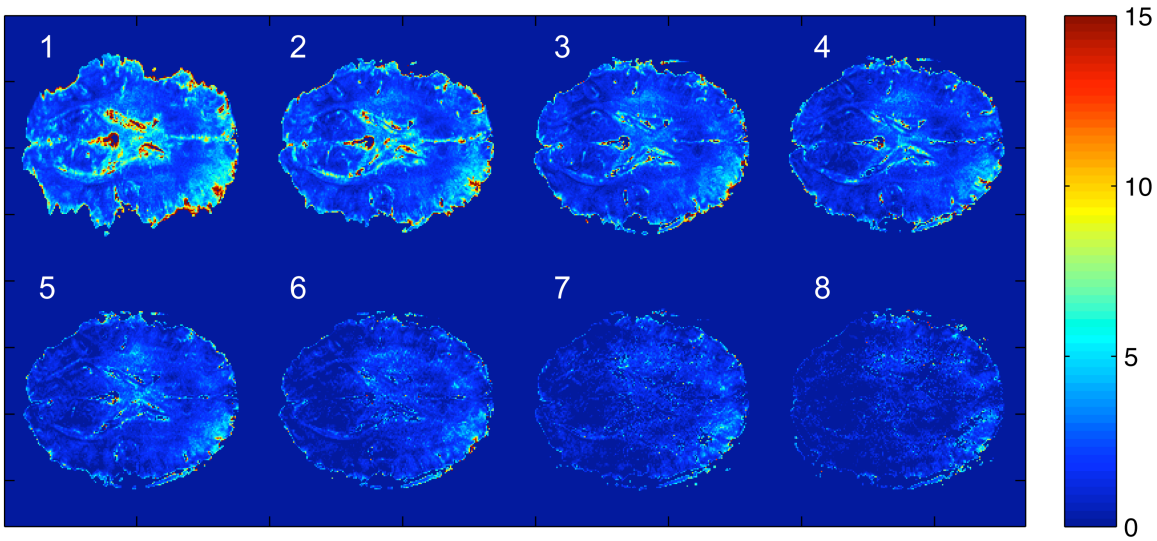

Figure 3.7. Maps of the ratio of physiological noise to thermal noise on one representative subject for R = 1-8 (white numbers). As expected, this ratio varies widely across the brain and is highest in the ventricles, CSF, gray matter, and on the edges. As R increases, the ratio of physiological noise to thermal noise decreases according to the theoretical predictions of $\frac{1}{g \cdot \sqrt{R}}$ (see Fig. 3.8). The largest decreases occur in the areas where *g*-factors are large (see Fig. 3.1). Median values for the ratio of physiological noise to thermal noise range from about 3-5 depending on subject and location in the brain.

5. Discussion

Physiological noise is a major concern for high field fMRI experiments because it scales with field and signal strength. At 7T and above, physiological noise can be a dominant source of temporal variance for fMRI studies. At the same time, high field fMRI studies using single-shot gradient-echo EPI frequently suffer from magnetic susceptibility effects such as image distortion and signal dropout. Thus far, these issues have limited the utility of gradient-echo EPI in high field fMRI applications.

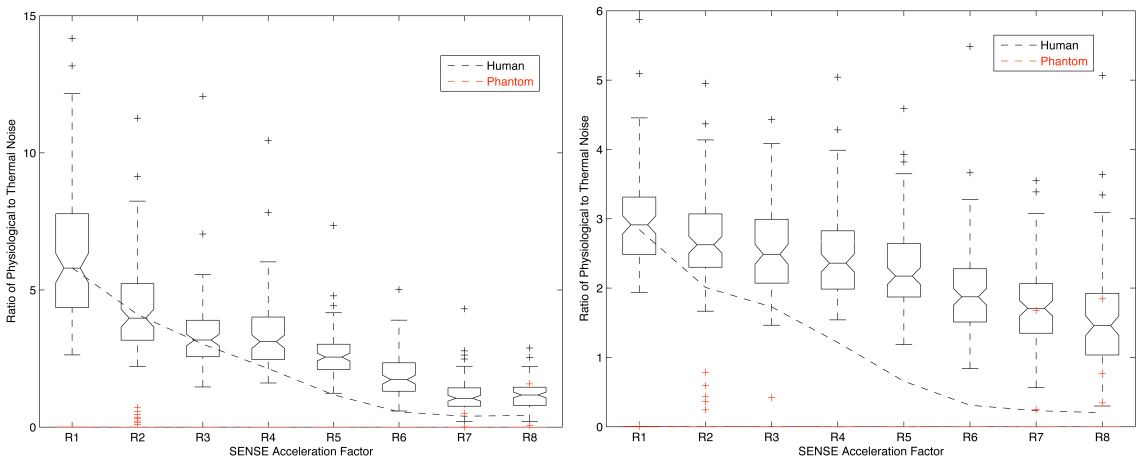

Figure 3.8. The ratio of physiological to thermal noise within (left) a central ROI (21x21 pixels) and (right) an off-center ROI (21x21 pixels) specifically selected in an area of low *g* across all R, averaged across all humans (black) and phantoms (red) for each R. The dashed curves represent the theoretical $\frac{1}{g \cdot \sqrt{R}}$ based on the median *g*-factor within the ROI. Agreement with theory is better when *g* is low, as seen in R = 1-3 on (right) and all of (left), which was a specifically chosen low-*g* area. In an ROI where *g* is large (not shown), we observe lower ratios of physiological noise to thermal noise that decrease more slowly as R increases. This is probably because in areas where *g* is large to begin with, it does not change as quickly with R.

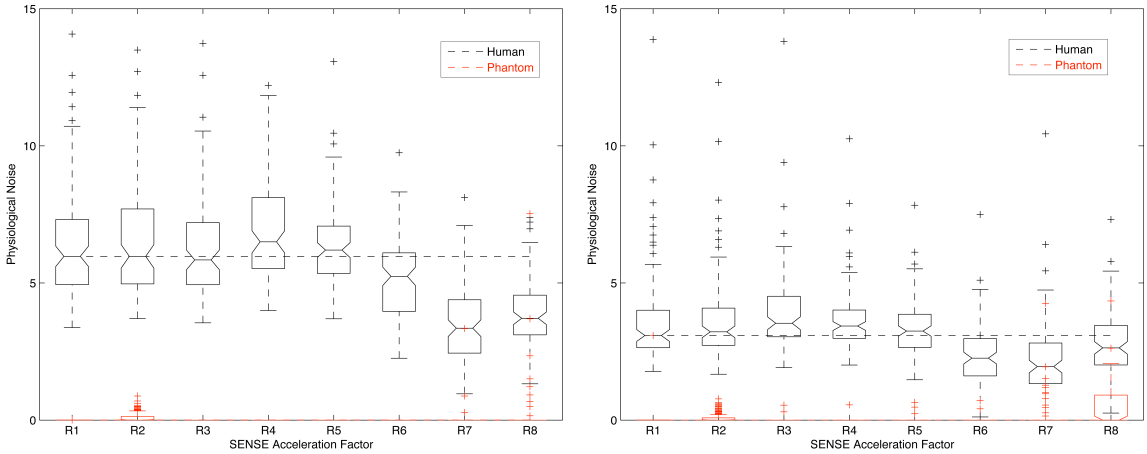

Figure 3.9. Absolute physiological noise within (left) a central ROI (21x21 pixels) and (right) an off-center ROI (21x21 pixels) specifically selected in an area of low *g* across all R, averaged across all humans (black) and phantoms (red) for each R. The absolute contribution of physiological noise to the fMRI data does not show any significant relationship with R. Note that the physiological noise in the central ROI represented in (left) is larger than that seen in (right) because the central ROI (left) lies in the center of the image near the ventricles.

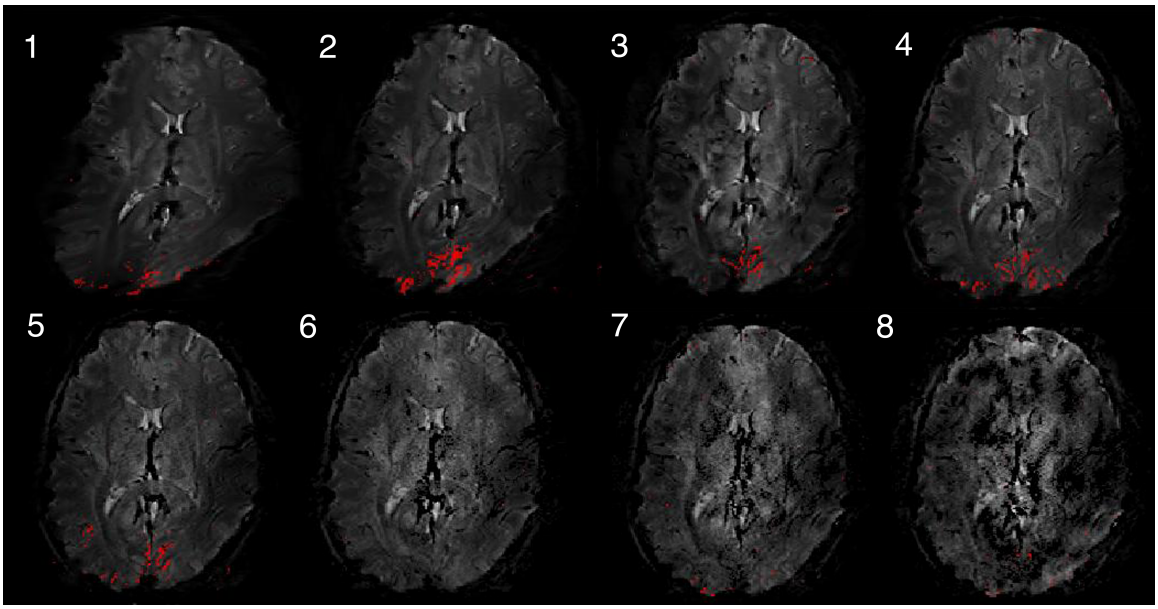

Figure 3.10. SPM-generated activation maps ($p < 0.0001$) overlaid onto anatomical slices for R = 1-8 (white numbers) for one representative subject. Activation clearly decreases as R increases. On this slice of this subject, activation is no longer reliably detectable beyond R = 5. Distortion decreases significantly as SENSE acceleration increases through R = 5. Under these conditions, R = 4 appears to represent the best compromise between activation, distortion, and SNR.

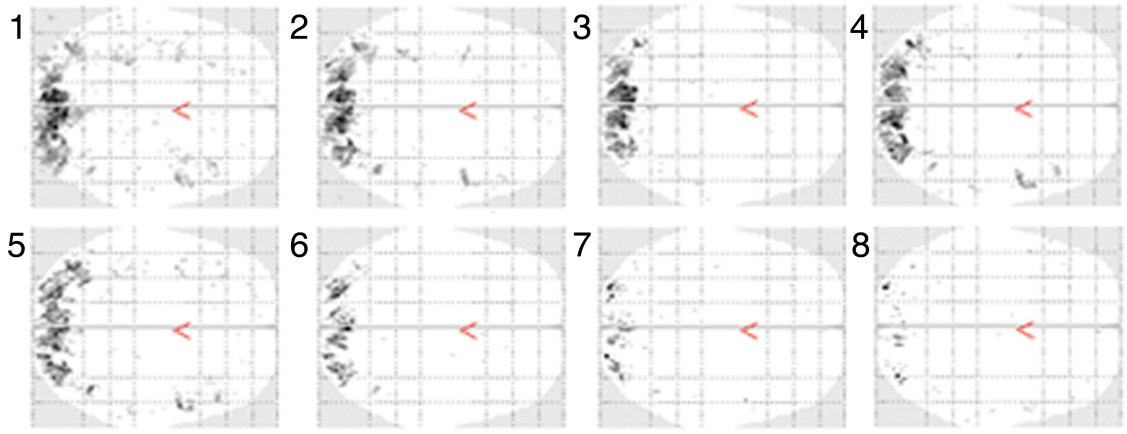

Figure 3.11. Visual activation for R = 1-8 (black numbers) in one subject. This "glass brain" view takes into account activation in all slices of the acquired volume. The degree of activation portrayed clearly decreases as R increases, though significant activation is still visible through R = 6 here (compare to Fig. 3.10, which shows only one slice).

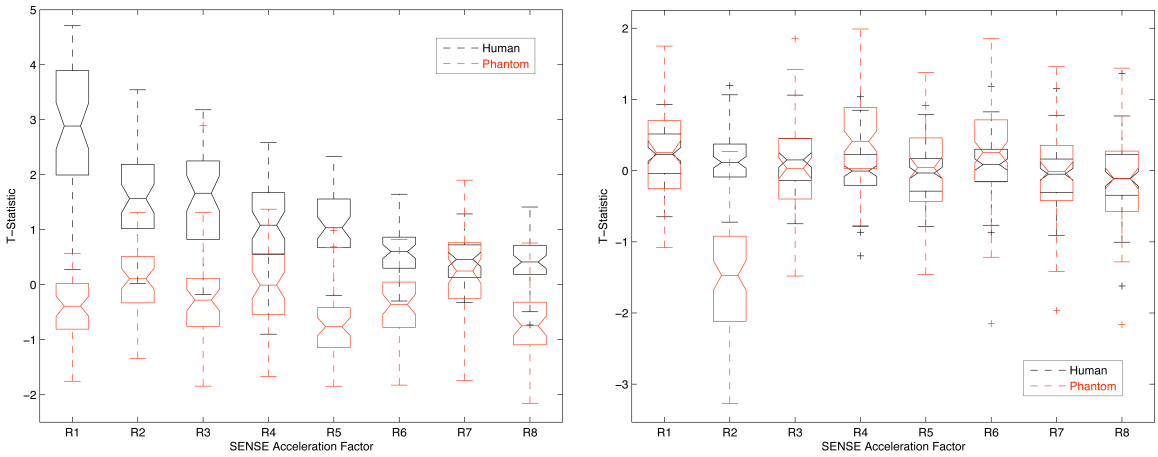

Figure 3.12: T-statistics in (left) an activated ROI (7x7 pixels) in the visual cortex and (right) an inactive ROI (7x7 pixel) in gray matter in one representative human (black) and in the same ROI on a phantom (red). In the active ROI (left), T-statistics decrease as *R* increases. In agreement with Figure 3.11, significant activation is clearly visible through R = 6. In the inactive ROI (right), there is no significant difference between T-statistics in humans or in phantoms as expected.

Parallel imaging techniques present a number of natural synergies with high field imaging, including an efficient means of reducing MSE at a modest cost to SNR (Wiesinger et al., 2006). Given that the effects of both physiological noise and SENSE acceleration have a significant presence in high field fMRI, we thought it worthwhile to characterize their interactions in a typical high-resolution fMRI study at 7T. Central to this aim was to confirm whether physiological noise is sensitive to SENSE acceleration or whether physiological noise influenced the quality of the SENSE reconstruction in any significant way.

Wiesinger et al. (2004; 2006) have given theoretical predictions for the behavior of *g* and its corresponding effect on SNR, and they have experimentally verified these predictions using an electrodynamic scaling technique which simulates changes in B_0. We have verified their predictions in human fMRI studies for acceleration factors ranging from R = 1-8 at 7T. Specifically, our

results confirm that the geometry factor *g* operates in two regimes: the first, favorable regime is characterized by low *g*-factors close to the optimal value of 1 (generally $R < 4$ in our experiment). In this case, the temporal variance of a time series of images is dominated by physiological noise in humans. In the second regime - which sets in beyond some critical degree of reduction that depends on a combination of B_0, coil configuration, number of coil elements, coil loading, and other factors - is characterized by an exponential growth of *g* (generally > 5 here). In this case, amplified thermal noise due to *g* and R dominate both the spatial and temporal variance for both humans and phantoms.

In agreement with theoretical predictions, Figures 3.7-3.9 demonstrate that the observed decrease in the ratio of physiological noise to thermal noise is due to the increase in thermal noise related to *g* and R. Meanwhile, the absolute contribution of physiological noise remains roughly constant.

High image SNR values lead to a plateau of TSNR at high field strengths when physiological noise dominates temporal signal fluctuations (Kruger and Glover, 2001; Triantafyllou et al., 2005). This plateau is quickly reached at 7T, meaning improvements in magnetic field strength beyond this point will not yield significant gains in TSNR or fMRI sensitivity. Under these conditions the full potential of high field imaging cannot be realized unless the contribution of physiological noise to the time series is reduced.

Triantafyllou et al. (2005) have demonstrated that decreasing voxel volume is an effective means of reducing the relative influence of physiological noise in fMRI data at a given field strength. More recently, physiological noise

has been shown to decrease as the number of receive elements in a parallel imaging coil array increases even in the absence of acceleration (Jonsson et al., 2009). This could be because as the number of coil elements increases, the sensitivity map associated with each one becomes more precise and less sensitive to B_0 fluctuations (Weiger et al., 2006; Ohliger et al., 2003). In this context, increasing the number of receive elements in an array enables higher resolutions to be achieved through greater acceleration -- thereby reducing physiological noise due to smaller voxel volumes -- while at the same time reducing physiological noise through smaller and more accurate coil sensitivity profiles. This may be thought of as increasing the effective “sensitivity resolution” of the array.

One possible explanation for this behavior is that physiological noise affects SENSE image reconstruction by increasing the noise covariance between neighboring voxels, or between voxels which are affected by physiological noise in a similar way (i.e., in gray matter). When the coil elements are smaller, physiological noise could become more distributed, reducing the impact on each sensitivity profile.

Another way in which physiological noise could affect SENSE image reconstruction is through the time-varying magnetic field fluctuations due to respiration (Raj et al., 2000; Raj et al., 2001; Van de Moortele et al., 2002). These susceptibility effects could create discrepancies between the actual sensitivity maps used to reconstruct the images (usually acquired only once at the beginning of the scan session) and the theoretically “optimal” set of sensitivity

maps which would most precisely unfold and combine the individual coil images acquired under specific magnetic field conditions ("ideal" maps could be slightly different in each coil at every time point); This is analogous to the way in which individual B_0 field maps collected at the beginning of a scan session can be insufficient to completely correct distortion in a series of images which encounters magnetic field fluctuations over time (due to motion, respiration, scanner instability or other sources).

We note also that the *g*-factor hotspots observed in Figure 3.1 are not predicted by theoretical models of the "ultimate" achievable SNR in SENSE imaging which assume a perfect receiver coil array (Ohliger et al., 2003; Wiesinger et al. 2006). This suggests that another benefit of increasing the number of coil elements would be not only substantially reduced *g*-factors, but also a significant increase in *g*-factor uniformity throughout the object.

We observed the transition from physiological noise dominance to thermal noise dominance between R = 4-5 (averaged across the entire brain) in our experiment. In physiological noise-dominated regions such as the ventricles (as seen in Figure 8a), the transition did not occur until R = 7. Meanwhile, in a white matter region away from the center of the head, we observed the transition at R = 3. Together, these observations demonstrate that even at the relatively high resolution of $2mm^3$ ($1 \times 1 \times 2mm^3$), physiological noise is still a major source of temporal variance in high field fMRI data. At lower resolutions, we expect these effects to be even more pronounced.

As we did not observe any specific interaction between SENSE acceleration factor and the absolute contributions of physiological noise to our images, our findings suggest that the primary role of SENSE in single-shot gradient-echo EPI for high field fMRI will be either 1) to decrease physiological noise indirectly through increasing spatial resolution while maintaining a constant acquisition time, or 2) to decrease distortion at a fixed spatial resolution while shortening acquisition time, depending on the demands of a given experiment.

Increasing SENSE acceleration decreases SNR and TSNR and thus will not “optimize” the acquisition in the strictest sense. However, it is quite possible that the reductions in distortion or in physiological noise may be more valuable than the corresponding loss in TSNR for a given experiment. Therefore, assuming one maintains the necessary TSNR to detect BOLD activation in areas of interest, the SENSE factor becomes an additional degree of freedom in obtaining an optimal tradeoff between acquisition time, image distortion, coverage, and resolution (and implicitly physiological noise).

A final consideration is that the choice of acceleration direction determines the spatial distribution of *g*-factors. Our left-right phase encoding direction led to areas of high *g* near our areas of interest in the visual cortex at higher R values. These did not contaminate our results at lower $R < 4$ because on average $g < 2$ in those cases, but at higher R the presence of large *g*-factors near regions of functional interest could impact fMRI sensitivity. This is confirmed by Figures 3 and 5, which show that TSNR and residual variance are closely matched to the patterns of *g* observed in Figure 3.1. Thus, one should take care in choosing the

acceleration direction such that areas of rapid *g*-factor growth do not overlap with the regions of functional interest. Conversely, understanding the spatial distribution of *g*-factors in a specific study may allow for higher-than-typical acceleration if it can be verified that areas of large *g* do not coincide with regions of interest.

6. Conclusions

This work demonstrates that the ratio of physiological noise to thermal noise decreases according to the well-known $g \cdot \sqrt{R}$ relationship in SENSE fMRI acquisitions at 7T. The apparent reduction in physiological noise as R increases owes more to an increase in SENSE-related thermal noise than to a reduction in magnetic susceptibility effects caused by respiratory, cardiac, or other physiological processes. Thus, while physiological noise decreases relative to thermal noise as R increases, the absolute contribution of physiological noise appears independent of R. While these results are not altogether unexpected, we believe there is some value in the continued validation of existing theory as field strengths increase.

In our experiment the dominant source of temporal variance transitioned from physiological noise to thermal noise between R = 4 and R = 5 on average across the brain. We also observed robust T-values through R = 4, and significant reductions in image distortion through R = 4. Beyond this critical point, *g* and R related thermal noise dominated the temporal variance.

Despite our observation that physiological noise does not appear to directly interact with the SENSE acceleration factor, we note that it is possible to reduce physiological noise through SENSE acceleration by trading SNR for smaller voxels (Triantafyllou et al., 2005). Therefore we conclude that the acceleration factor R acts as an additional degree of freedom in selecting acquisition parameters to obtain an optimal tradeoff between acquisition time, image distortion, coverage, resolution, and physiological noise for a given fMRI application.

We suggest that optimal conditions for a given single-shot gradient-echo EPI functional MRI experiment at high field can be achieved by first selecting the highest reasonable resolution, given hardware and experimental constraints, in order to reduce physiological noise and partial volume effects (e.g. Bodurka et al.'s "suggested voxel volume" in which the relative contributions of physiological noise and thermal noise are equal (2007)); then the SENSE acceleration factor should be chosen to minimize distortion while maintaining geometry factors in the "favorable" regime to ensure minimal TSNR sacrifices.

Because calculation of the geometry factor depends on numerous unique considerations (Pruessmann et al., 2006; Wiesinger et al., 2006), it is not generally practical to determine theoretical maps of *g* for a given experimental set-up. Instead, we recommend that initial validation studies be performed to ensure geometry factors are within acceptable limits before acquiring human fMRI data. In general $g > 2$ should be avoided in experimentally relevant areas.

Taken together, these results suggest the most efficient way to enhance high field fMRI performance is investment in high quality parallel imaging arrays with many coil elements. Increasing the number of coils in an array increases the baseline SNR, which can be used to acquire images at higher resolutions. High resolutions, in turn, reduce the influence of physiological noise on the time series data. Coil arrays with more elements also offer reduced image distortion through the ability to achieve higher acceleration factors while maintaining geometry factors in the lower, favorable regime. Finally, as noted by Pruessmann (2006), increasing the number of coil elements has no drawback apart from increasing the amount of data generated by each scan and requiring greater precision in coil array calibration.

CHAPTER IV

OPTIMIZATION OF SENSITIVITY ENCODED FMRI ACQUISITIONS AT HIGH FIELD

1. Introduction

When applied to the phase encoding direction(s) of echo-train pulse sequences such as 2D-EPI, 3D-FFE, or 3D-PRESTO, sensitivity encoding can shorten acquisition time, reduce magnetic susceptibility artifacts, increase spatial or temporal resolution, increase the field of view, or reduce gradient acoustic noise (Pruessmann et al., 1999; Weiger et al., 2002; Wiesinger et al., 2006; Pruessmann 2006; de Zwart et al., 2006). SENSE also incurs a spatially-varying signal-to-noise penalty $g \cdot \sqrt{R}$, which depends on the total degree of acceleration (R) and the local geometry factor (*g*), which is determined in part by coil geometry, the field of view (FOV), the object of study, and coil sensitivity profile characteristics (Pruessmann et al., 1999; Wiesinger et al., 2006).

When sensitivity profiles have errors or are not distinct, even modest amounts of aliasing will lead to high geometry factors. By contrast, highly accurate sensitivity profiles enable separation of more highly aliased signals and will therefore yield lower *g* values even when the degree of aliasing is high.

While *g* tends to vary widely over the imaging volume, the aliasing patterns are somewhat intuitive for in-plane acceleration in 2D imaging. Figure 4.1 illustrates possible fold-over scenarios for varying degrees of single-

dimensional acceleration in the simple case of a circular object that fits fully within the FOV in an axial slice.

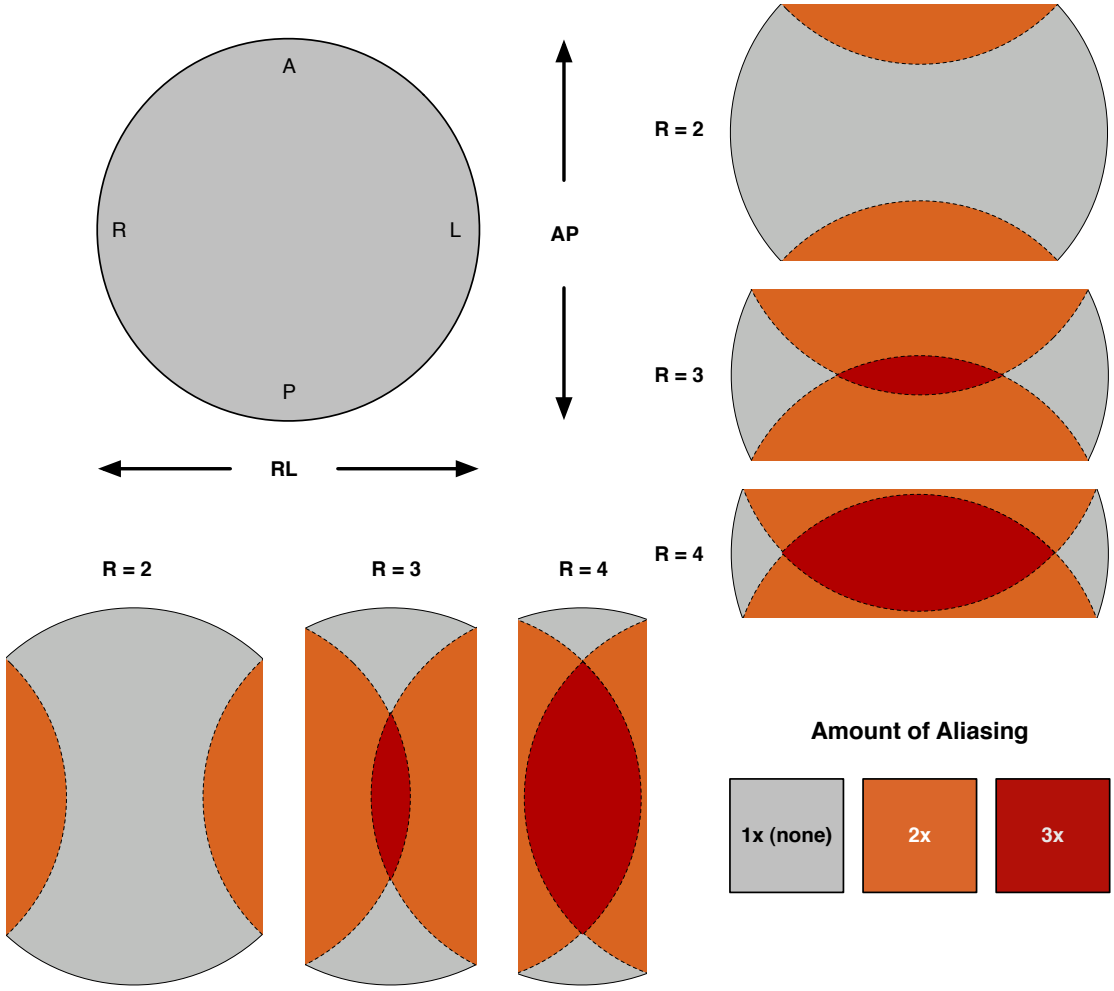

Figure 4.1: Aliasing due to single dimensional acceleration in either the RL (bottom) or AP (right side) phase encoding directions. The distribution of geometry factor depends strongly on the direction of acceleration, commonly the phase encoding direction.

Three dimensional acquisitions can accelerate both phase encoding directions independently. There are a number of benefits to this approach. First, distributing the total undersampling across two phase encoding directions tends to improve the conditioning of the reconstruction problem, which results in higher

achievable net reduction and reduced *g* compared to the same degree of acceleration in a single-dimension (Weiger et al., 2002). Second, the additional phase encoding steps in 3D imaging generally add significant scan time compared to 2D-EPI scans with the same coverage. Applying SENSE in the second phase encoding direction in a 3D acquisition can reduce the number of "slice encoding" steps, thereby reducing the total number of shots necessary to collect the entire data set and shortening the total scan time. Finally, the SNR benefits from whole-volume excitation make 3D imaging more resistant to the SNR penalties inherent to SENSE imaging.

On the other hand, when acceleration is applied in two dimensions, the geometry factor distribution becomes more complex. This is especially true when the field of view is small, the object is not symmetrical within the FOV, or when acceleration is applied along a direction which does not align with the receiver array elements. Figure 4.2 illustrates aliasing in the straightforward case of symmetrical 2-D acceleration in both in-plane phase encoding directions for a circular object within the FOV. With R = 2x2, the resulting image has many fewer pixels with high degrees of aliasing (red) than the comparable R = 4x1 scans in Figure 4.1. Figure 4.3 shows the case of a limited field of view and asymmetric object (such as the back of the head) as is common in high field fMRI.

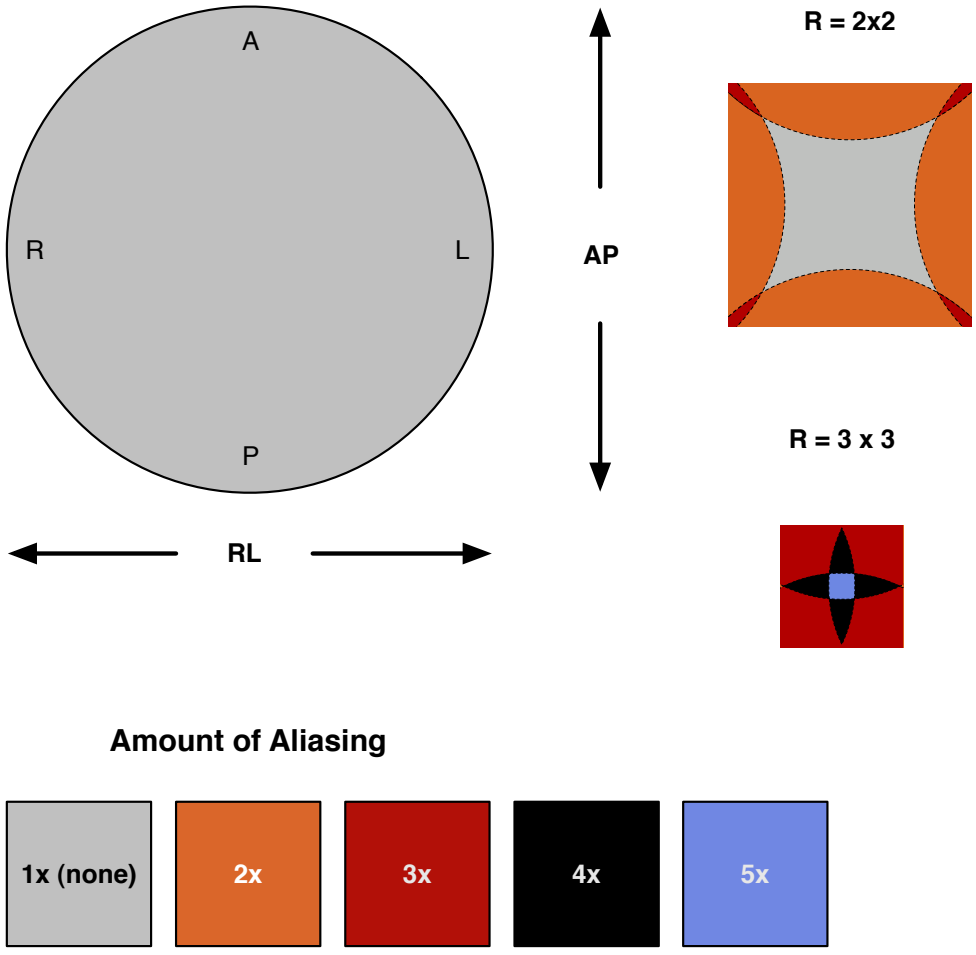

Figure 4.2: Aliasing due to symmetric acceleration of both phase encoding directions within the imaging plane of a 3D acquisition.

The geometry factor is determined not only by the degree of aliasing (as shown in Figures 4.1 - 4.3), but by a combination of this and characteristics of the coil sensitivity profiles and noise as described by Eq. 2.60 in Chapter II. For example, in an array with only 4 channels, a 3x aliased pixel would yield much larger geometry factors than if the same pixel had 3x aliasing in a 16 channel array. This is one reason why the geometry factor is unique to a given

experimental set-up. As predicted by Wiesinger et al. (2006) and shown experimentally in Chapter III, the geometry factor operates in two regimes: the first, favorable regime is characterized by *g* values close to the ideal value of 1, while the second, unfavorable regime is characterized by exponential growth of *g*. When g is high, SENSE-related noise enhancement can dominate both spatial and temporal noise in fMRI data.

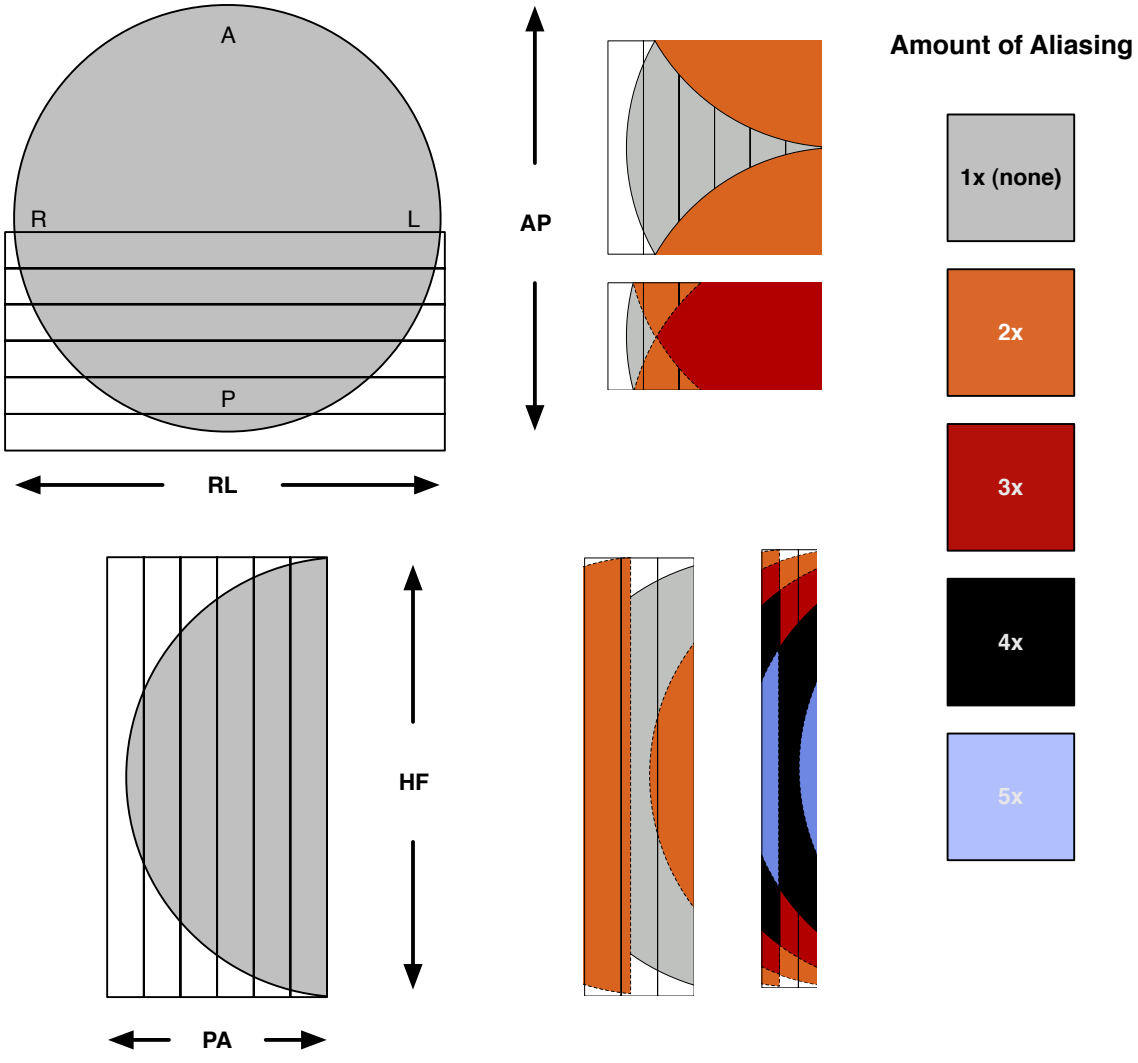

Figure 4.3: In-plane (head-foot) and through-plane (anterior-posterior) aliasing in a limited FOV with curved object.

Coil configuration relative to the FOV and acceleration direction is critical factor in determining the degree of local noise enhancement. Experiments by Weiger et al. (2002) involved arranging four receiver coil elements to yield the lowest geometry factors for acceleration of both in-plane image dimensions. However, in most cases the receiver array configuration will be fixed. For example, the VUIIS has a commercial 16-channel receive-only SENSE coil with array elements positioned as shown in Figure 4.4.

Optimizing sensitivity encoded fMRI acquisitions with a fixed coil array therefore entails finding configurations of slice orientation, field of view, and acceleration factors to achieve specific criteria (i.e., high temporal resolution or low distortion) while maintaining geometry factors within acceptable levels. A rule of thumb is to maintain $g < 2$ in areas of functional interest. Given the numerous factors involved, it is not generally possible to predict local g for all points in a given experiment. Therefore it is important to run validation studies to ensure that the g, TSNR, and other critical quantities are within acceptable bounds prior to costly and time consuming functional data acquisition.

Here we present a series of experiments designed to characterize the volume distribution of geometry factor and the associated effects on temporal signal stability in single-shot gradient-echo 2D-EPI, multi-shot 3D-FFE, and multi-shot 3D-PRESTO under a variety of resolution, field of view, and acceleration conditions. The ultimate goal of this work is development of a method for generating optimized imaging sequences for a variety of high field fMRI applications. Two specific aims of this chapter are 1) to identify one or more 3D-

PRESTO sequences appropriate for high temporal resolution, full brain coverage fMRI at 7T and 2) to identify a set of 2D-EPI, 3D-FFE, and 3D-PRESTO sequences which represent optimal trade-offs between coverage, distortion, temporal signal to noise and imaging time at both high and low resolutions with coverage appropriate for retinotopic mapping. These sequences will be applied to a retinotopic mapping experiment in the next chapter.

2. Methods

All data were collected on a Philips Achieva 7T scanner with 16 channel SENSE receive-only head coil (as shown in Figure 4.4) and outer quadrature transmit coil. Though most of the results presented here are from phantom studies, four MR experienced volunteers were also scanned to compare phantom measurements with *in vivo* data. Each subject provided written informed consent and was treated in a manner consistent with a protocol approved by the IRB of Vanderbilt University. Subjects' heads were secured with padding and a bite bar to minimize motion. Geometry factor maps and TSNR maps were calculated as described in Chapter III.

Six experiments were conducted to the highest acceleration values that could be applied with acceptable g-factors and TSNR in both low resolution, full coverage and high resolution, limited FOV applications. For clarity, each is described separately.

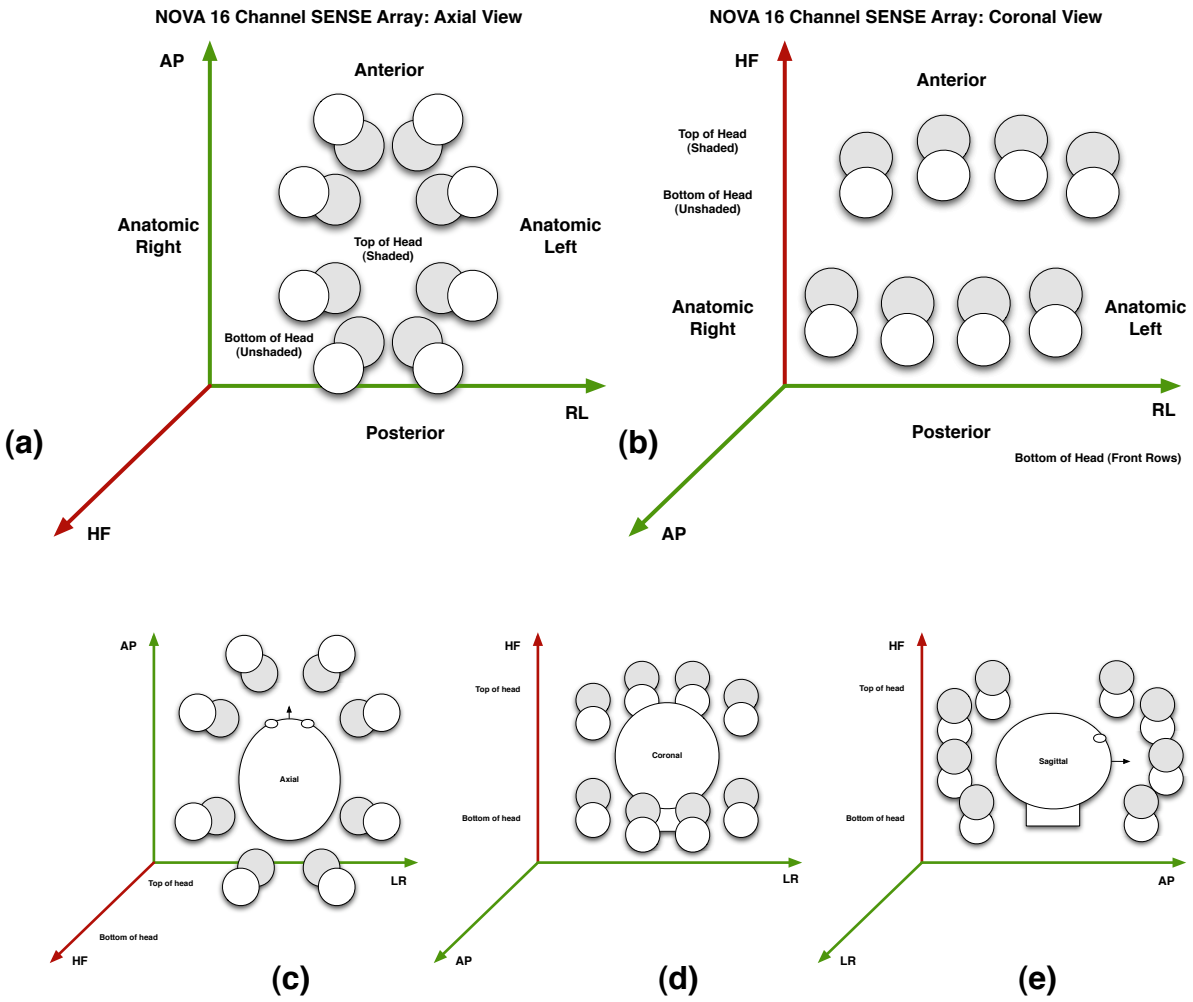

Figure 4.4: Coil element layout for the VUIIS NOVA 16 channel headcoil. (a) Axial view (b) coronal view. Shaded coil elements are located near the top of the head, while unshaded coil elements are located toward the base of the head. Coil elements shown relative to axial (c), coronal (d), and sagittal (e) slice orientations. Green axes are directions favorable for SENSE acceleration, while red axes are unfavorable for acceleration.

2.1. Experiment 1: High-resolution 3D-FFE scan with limited FOV and 2D acceleration

This experiment aimed to compare the effects in-plane versus through-plane acceleration in a high resolution 3D-FFE scan. A spherical phantom was scanned with a multi-shot 3D-FFE sequence at 0.5 x 0.5 x 1 mm^3 with 128 x 128

x 20 mm^3 field of view. Echo train length (ETL) was 17, TR = 50ms, and TE = 21ms for all scans. 20 coronal slices were placed on the back edge of the phantom to simulate an fMRI study of the visual cortex. In-plane acceleration (R_P) of the right-left (RL) phase encoding direction was varied from 1 to 4 in steps of 0.25 for each of three values (1.0, 1.25, and 1.5) of through-plane acceleration (R_S) in the anterior-posterior (AP) direction. Results from Experiment 1 are shown in Figures 4.5 - 4.6.

2.2. Experiment 2: Sphere and head phantom in high resolution 3D-FFE

This experiment had three aims: (1) to compare the geometry factor distribution when acceleration is increased to reduce sampling in the in-plane or through-plane phase encoding directions independently; (2) to determine whether the noise contributions from acceleration in each direction are independent, and whether it is possible to simulate g-factor maps at arbitrary acceleration factors from multiplication of "component" maps[16]; and (3) to compare geometry factor volumes between a spherical phantom and a "head" phantom with the same shape, size, and dielectric properties as the human head.

Both phantoms were scanned with the acquisition parameters, slice placement, and FOV described in Experiment 1. Two series of "component" *g*-volumes were generated: in series one, in-plane RL acceleration (series R_P) was varied from 1 to 7 in steps of 0.5 while $R_S = 1.0$; in series two, through-plane AP

[16] For example, whether it is possible to simulate the geometry factor volume for $R_S = 1.5 \times R_P = 4.0$ acceleration by multiplication of component maps [$R_S = 1.5$ by $R_P = 1.0$] x [$R_S = 1.0$ by $R_P = 4.0$].

acceleration (series R_S) was varied from 1 to 7 in steps of 0.5 while R_P = 1.0 (for a total of 26 g-volumes). The sphere phantom scans from Experiment 1 and Experiment 2 took place back-to-back on the same day, while the head phantom scans took place at a later date.

Simulated *g*-volumes were created by multiplying "component" maps from the R_P and R_S series in all combinations (13 x 13 = 169 volumes, each with 20 slices, totaling 3,380 g-maps for each phantom). Simulations were compared to measured g-maps from Experiment 1 and compared between sphere and head phantoms. Results from Experiment 2 are shown in Figure 4.7 - 4.12.

2.3. Experiment 3: Survey of fast, full brain 3D-PRESTO scans

This experiment aimed to characterize geometry factor and temporal SNR distributions in ten full brain, high temporal resolution 3D-PRESTO scans to determine their potential for fast, full brain fMRI at 7T.

A first set of four 3D-PRESTO scans with isotropic 3.5 x 3.5 x 3.5mm^3 resolution, axial slice orientation and 224 x 182 x 100 mm FOV were tested in order to determine how quickly full brain coverage could be achieved. Volume TR times were 0.6s, 0.5s., 0.333s, and 0.2s. Acceleration factors were increased such that scan time was reduced while TR = 15ms, TE = 8ms (nominal) / 23ms (shifted), field of view, in-plane frequency and phase encoding bandwidth, echo train length, flip angle, and number of slices were held constant. Parameters for these low resolution axial 3D-PRESTO sequences are shown in Table 4.1.

A second set of 3D-PRESTO scans were acquired in axial orientation with 220 x 176 x 110 mm FOV, but with increased spatial resolution and longer scan times. These included: a 2.75 x 2.75 x 2.75mm^3 isotropic scan with dynamic scan time 0.75 s; a 2.3 x 2.3 x 2.3mm^3 isotropic scan with dynamic scan time 1.5 s; and a 2 x 2 x 2mm^3 isotropic scan with dynamic scan time 2.0 s. TR = 16ms, TE = 8ms (nominal) / 23ms (shifted), field of view, in-plane frequency and phase encoding bandwidth, echo train length, flip angle, and number of slices were held constant while acceleration and slices were changed to achieve isotropic resolutions at the lowest possible dynamic scan time to fill the FOV. Parameters for these medium resolution axial 3D-PRESTO sequences are shown in Table 4.2.

A third set of 3D-PRESTO scans were acquired in sagittal orientation with 220 x 220 x 175mm^3 FOV. These included a 3.5 x 3.5 x 3.5mm^3 isotropic scan with dynamic scan time 0.6 s; a 2.75 x 2.75 x 2.75mm^3 isotropic scan with dynamic scan time 1.0s, and a 2.3 x 2.3 x 2.3mm^3 isotropic scan with 1.0s dynamic scan time. TR = 15ms, TE = 8ms (nominal) / 23ms (shifted), field of view, echo train length, and flip angle were held constant while acceleration factors R_P and R_S and the number of slices were changed to maintain the constant FOV at each resolution. Scan time increased according to resolution. Parameters for these medium-resolution sagittal 3D-PRESTO sequences are shown in Table 4.3. Maps of the geometry factor and TSNR for each acquisition are shown in Figures 4.13 - 4.16.

2.4. Experiment 4: Incremental adjustments to in-plane acceleration in 2D-EPI

This experiment aimed to determine the highest value of in-plane acceleration that yielded geometry factors < 2 throughout the imaging volume in a 2D-EPI scan at 1 x 1 x 1mm^3 with 128 x 128 x 24mm^3 field of view, TR = 2.4s, TE = 22ms, and coronal slice orientation. The in-plane acceleration factor R_P was varied in the RL phase encoding direction from 1.5 - 3.0 while echo train length was reduced from 89 to 45. Resolution and FOV were held constant. Results from Experiment 4 are shown in Figure 4.17.

2.5. Experiment 5: Effects of slice thickness and number on geometry factor

This experiment aimed to investigate the effects of slice thickness and the number of slices acquired on volume geometry factor distribution. The spherical phantom was scanned with 3D-PRESTO with 224 x 176 x 100mm^3 field of view in both axial and sagittal slice orientations. TR = 14ms, TE = 6.4ms (nominal) / 20ms (shifted) Acceleration was constant with in-plane acceleration (R_P) of 2.4 and through-plane acceleration (R_S) of 1.7 for both scans[17]. In-plane resolution was fixed at 2 x 2 x 2mm^3, while the slice thickness and number of slices was varied to fill the 100mm through-plane FOV in both orientations (FH for axial slices; RL for sagittal slices). Specifically, we acquired the following combinations

[17] Because the extent of *g*-related noise enhancement in the through-plane direction depends on the extent of the FOV (as shown by the results of Experiment 3; see Figures 4.13-4.16), we knew we could apply larger through-plane acceleration in these studies in which the mm through-plane FOV was 100mm, compared to, say, Experiment 1 in which the through-plane FOV was only 20mm.

of [Slices, Thickness] in both slice orientations: [100, 1mm], [66, 1.5mm], [50, 2mm], [40, 2.5mm], [33, 3mm], [29, 3.5mm], [25, 4mm], [22, 4.5mm], [20, 5mm]. Results from Experiment 5 are shown in Figures 4.20 - 4.22.

2.6. Experiment 6: Validation of fMRI sequences for retinotopic mapping at 7T

This experiment aimed to develop a number of sequences appropriate for retinotopic mapping at high field with isotropic voxel sizes, minimal distortion, $g < 2$ throughout the imaging volume, and high temporal signal stability. In light of our findings from Chapter III and Experiments 1-5, we developed ten sets of acquisition parameters, one each of 2D-EPI and a corresponding 3D-scan (either 3D-FFE or 3D-PRESTO), at five resolutions: 1 x 1 x 1mm^3, 1.12 x 1.12 x 1.12mm^3, 1.67 x 1.67 x 1.67mm^3, 2 x 2 x 2mm^3, and 3 x 3 x 3mm^3. Parameters for these sequences are given in Table 4.4. Because these sequences were generally acquired with a narrow field of view in the slice direction, no through-plane acceleration was applied. Results for Experiment 6 are shown in Figures 4.23 - 4.25.

3. Results & Discussion

Because this chapter covers a number of separate experiments, results and discussion for each one are presented together. All findings are then considered in the conclusions section.

3.1. Results & Discussion for Experiment 1

Figure 4.5 shows median and mean geometry factors as a function of R_P for R_S = 1.0, 1.25, and 1.5. There is almost no difference between the mean or median values of *g* for R_S = 1.0 and R_S = 1.25, but the mean geometry factor increases considerably at R_S = 1.5. The median value also grows slowly for R_S = 1.5 at first, but becomes significantly higher than the corresponding values in R_S = 1.25 when $R_P > 3$ due to a combination of in-plane and through-plane aliasing (as seen in Figure 4.6). The shape of the mean *g*-factor vs. R_P curve does not change as R_S increases, supporting the notion that R_P- and R_S-related noise enhancement is independent.

In all combinations of R_P and R_S in Experiment 1, the mean and median values stay below $g = 2$. That is, a significant portion of the field of view had $g < 2$ even though $g > 2$ in some "hot spot" areas as shown in Figure 4.6. Color axes in the *g*-maps presented here are capped at $g = 2$, so bright red spots in these images are regions in which fMRI sensitivity may be compromised.

Figure 4.6 shows two distinct aliasing patterns. The left-right "lobe" fold-over pattern in both (a) and (b) is from in-plane R_P acceleration and represents the sides of the spherical phantom folded onto the middle (as seen in Figure 4.1). The large *g* hotspots observed in the center of each slice in the top panel of Figure 4.6(b) are from through-plane R_S acceleration and represent the back edge of the phantom folded onto the center as illustrated in Figure 4.3. These hotspots explain why the mean is significantly larger than the median values of *g* for R_S = 1.5 in Figure 4.5.

Note how *g* changes from one slice to another (top: slice 3, middle: slice 5, and bottom: slice 15) in the presence of through-plane acceleration. The R_S = 1.0 images (left column of Figure 4.6) show similar left-right fold-over patterns at each slice. By contrast, the R_S = 1.5 images show dramatically different g-factor behavior at each slice due to through-plane fold-over.

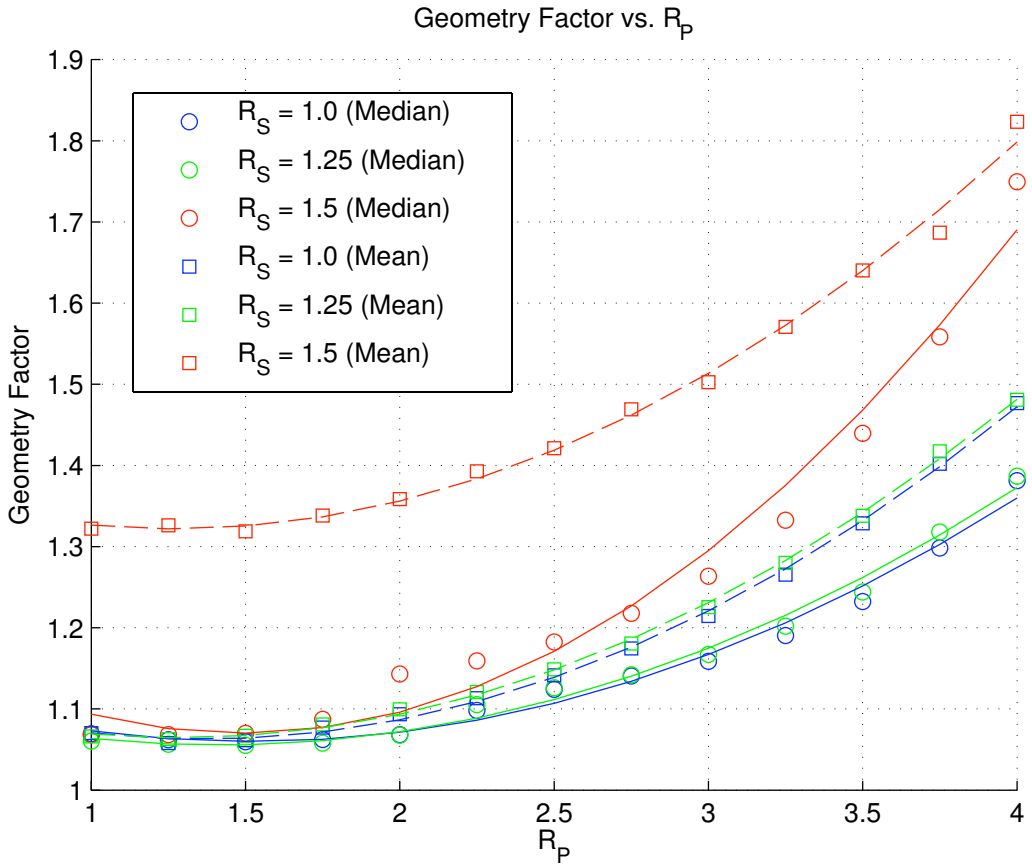

Figure 4.5: Geometry factor vs. R_P for three values of R_S. Median values are plotted with circles and mean values are plotted with squares. Solid and dotted lines represent 2nd order polynomials fit to the median and mean values of *g* at each R_S, respectively.

The bottom right panel of Figure 4.6 shows the area of the phantom that would correspond to the occipital pole in a human fMRI study. Here through-plane fold-over of the taller middle area of the phantom onto the back edge

causes $g > 2$ everywhere throughout the slice regardless of the value of R_P (see Figure 4.3). This would have serious consequences for fMRI because the SNR would be reduced by at least a factor of $2\sqrt{2}$ everywhere in the slice. Meanwhile the middle right panel, which corresponds to a slice in the middle of the phantom, experiences very little through-plane fold-over and is qualitatively similar to the corresponding $R_S = 1.0$ slice.

3.2. Results & Discussion for Experiment 2

Figure 4.7 shows mean geometry factor vs. R for both the sphere (blue) and head (red) phantoms in the R_P (circles) and R_S series (squares). In the R_P series (circles), the sphere and head phantoms show nearly identical, relatively low mean g-values that increase with R. In the R_S series (squares), *g*-factors grow quickly and in the same manner for both phantoms as R_S increases, but peak at $R_S = 3.5$. This pattern is the same in both the sphere and head phantoms, though the head phantom (red squares) attains significantly higher maximum *g* values.

A local maximum for *g* is somewhat counterintuitive in that one might expect *g* to grow monotonically as R increases (as is seen in the R_P direction). However, with the field of view placed on the back edge of the phantom, the object shape changes quickly in the through-plane direction, which can lead to isolated areas of extremely high geometry factors for specific aliasing patterns (R values) while *g* in the surrounding area grow more predictably. In agreement with

Figure 4.5, we observe the transition from R_S = 1.25 to R_S = 1.5 as the point where the geometry factor begins to grow rapidly.

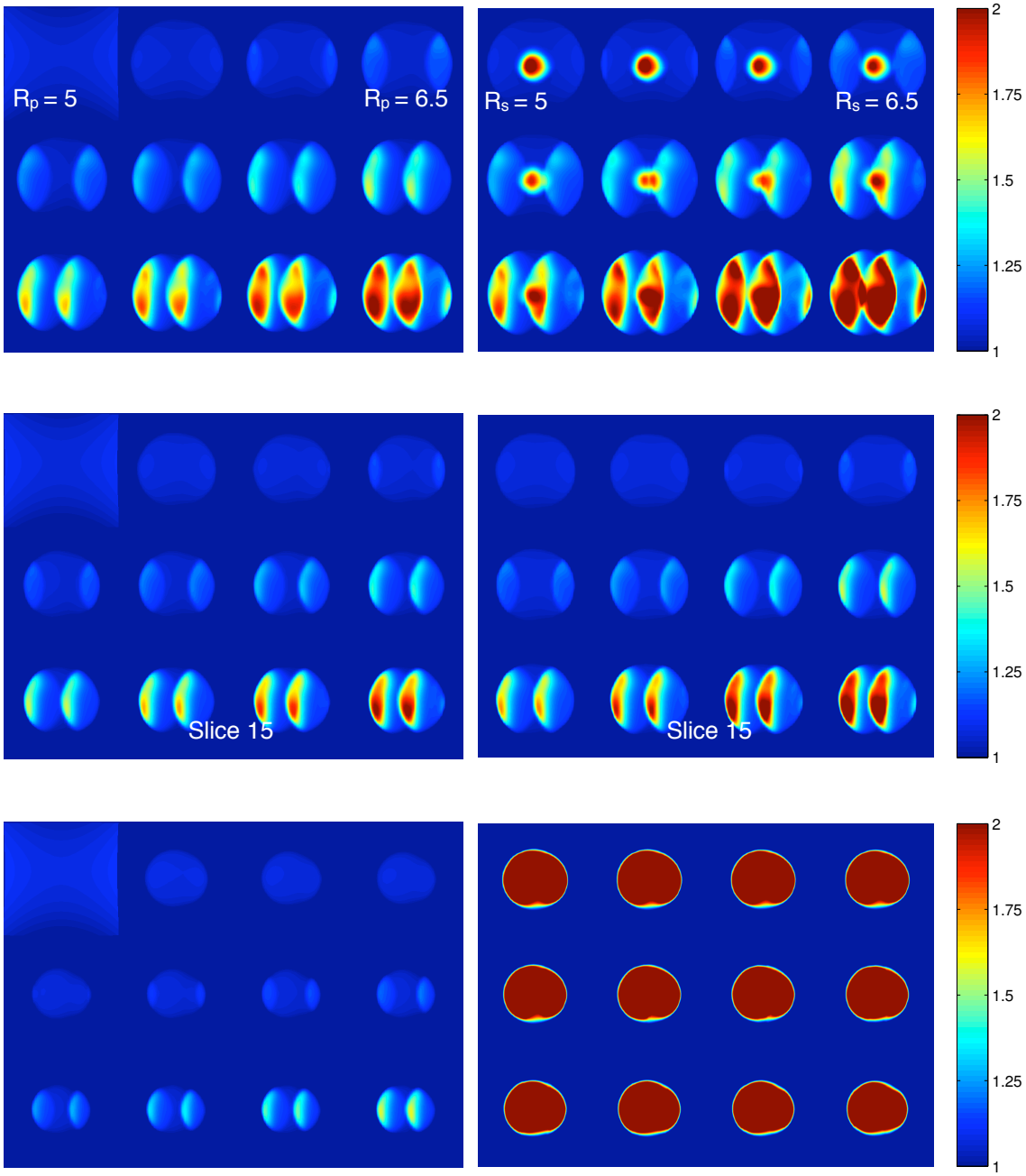

Figure 4.6: Geometry factor maps of coronal slices with R_P = 1.0-6.5 (from left to right, top to bottom within a panel) for R_S = 1.0 (left column) and R_S = 1.5 (right column). Each row represents one slice (top: slice 3, middle: slice 5, bottom: slice 15). Red voxels have g > 2.

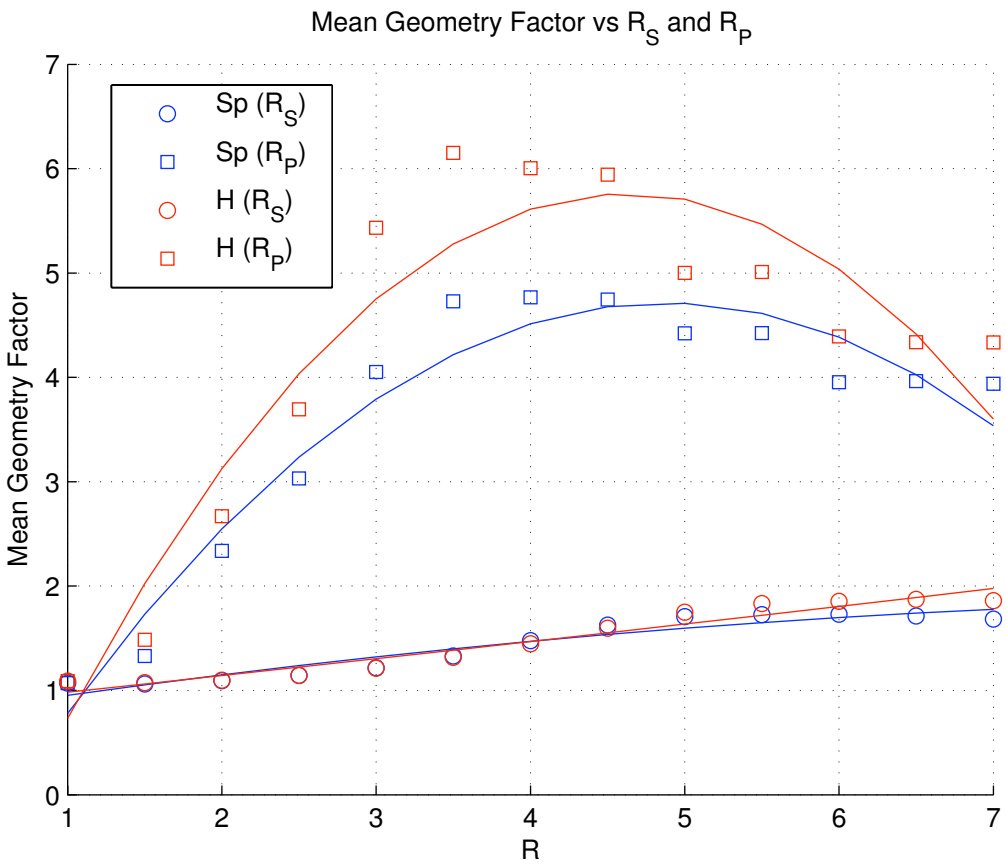

Figure 4.7: Geometry factor vs. R for the sphere (blue) and head (red) phantom in the R_P component series (R_P varies 1-7, R_S = 1; circles) and the R_S component series (R_S varies 1-7, R_P = 1; squares).

Figure 4.8 shows geometry factor maps for in-plane (left column) and through-plane (right column) acceleration in three slices (top panel: slice 3; middle panel: slice 5; bottom panel: slice 15) for the sphere phantom. In agreement with Figure 4.7, geometry factors for through-plane acceleration are much higher than for in-plane acceleration. General distribution of *g* for the head phantom are similar to those in the sphere phantom, though the values are somewhat higher as suggested by Figure 4.7.

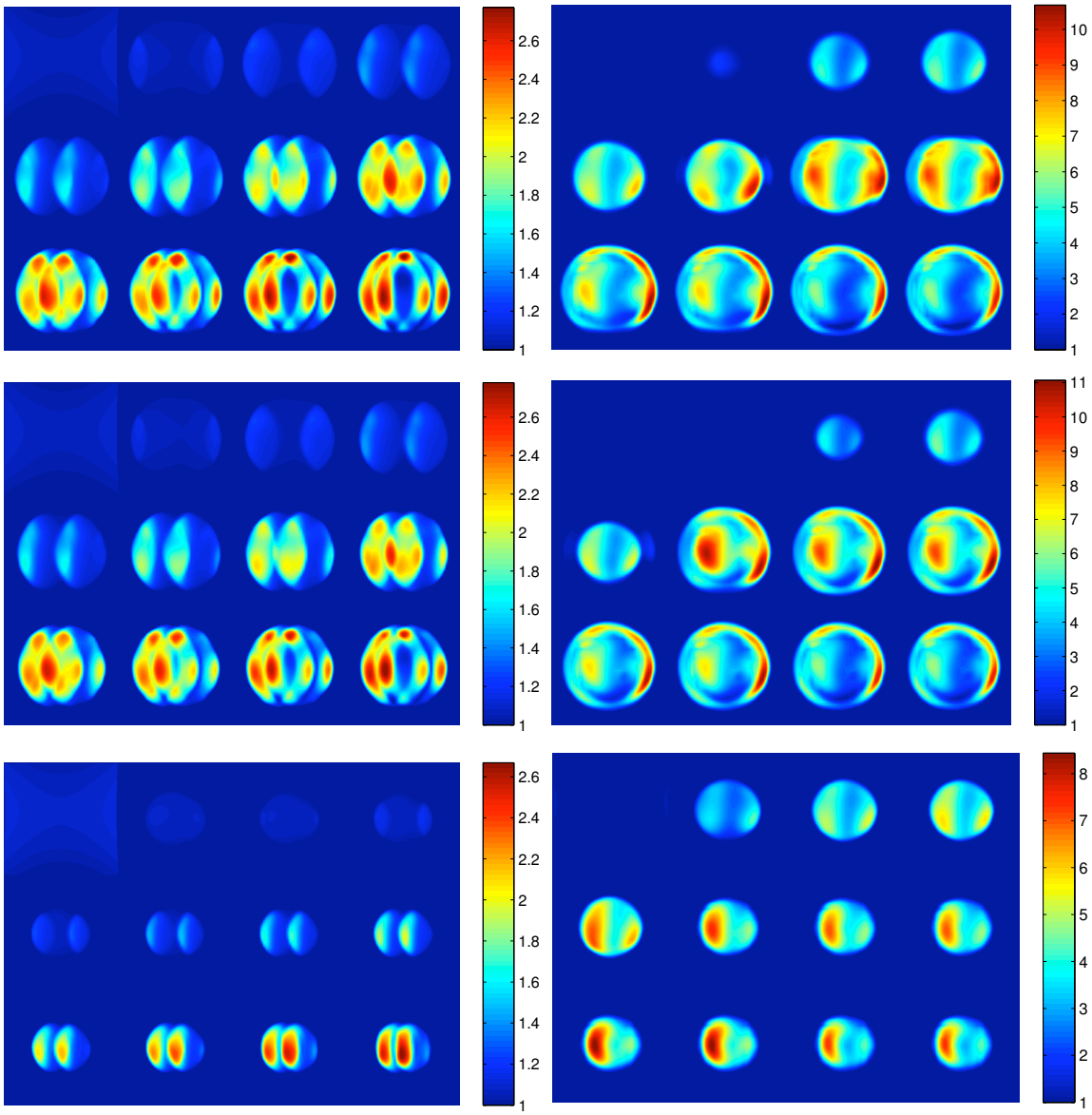

Figure 4.8: In-plane and through-plane geometry factor distributions in a sphere phantom with coronal slice orientation. Left column: g-maps for in-plane R_P = 1.0-6.5 (left to right, top to bottom within a panel). Right column: g-maps for through-plane R_S = 1.0-6.5 (left to right, top to bottom within a panel). Each row represents one slice (top: slice 3, middle: slice 5, bottom: slice 15). Note the drastically different scales for the in-plane (left) vs. through-plane (right) g-factors.

Figure 4.9 shows geometry factor distributions in slice 5 of both the sphere (left column) and head (right column) phantoms side by side. Fold-over patterns are qualitatively similar for both phantoms. At R_P = 4.5 a “double fold-over” effect appears and the distribution of *g* becomes more complex.

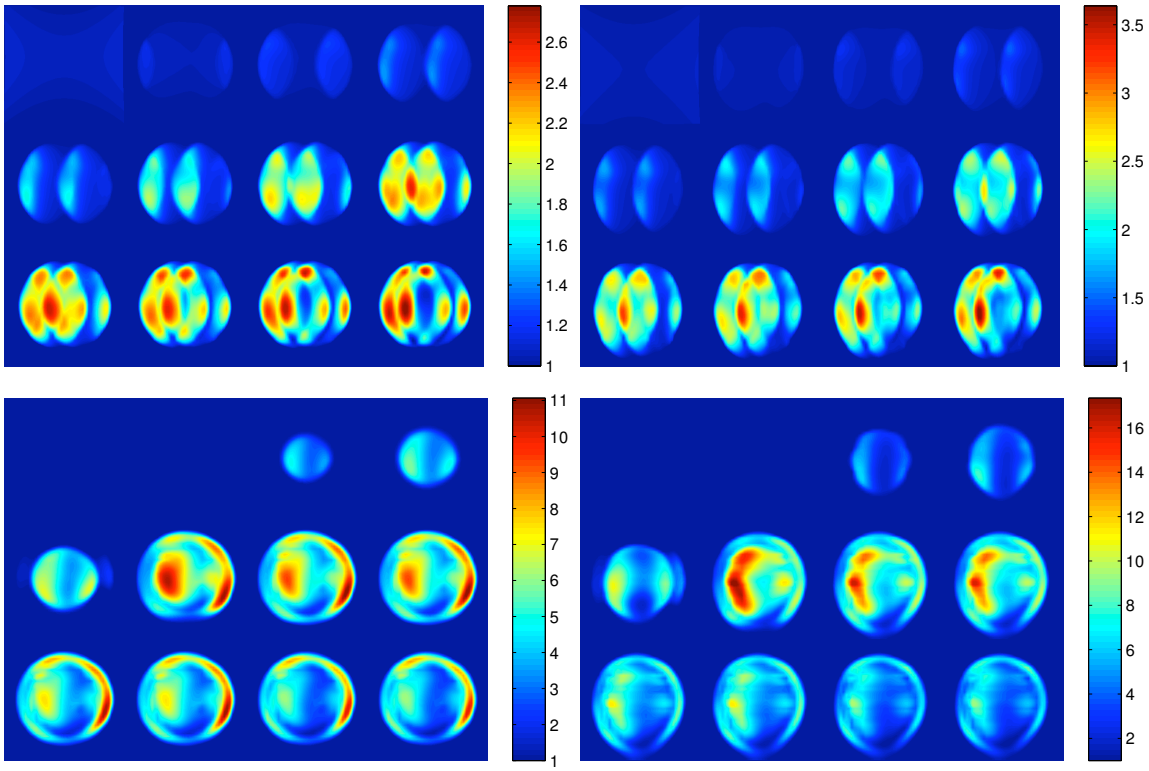

Figure 4.9: Sphere Phantom (left column) compared with Head Phantom (right column). Fold-over patterns for in-plane acceleration (top row) and through-plane acceleration (bottom row) are quite similar for both the sphere and head phantom.

One reason for larger geometry factors in the head phantom could be that the head phantom is larger than the sphere phantom. Since with a larger object there are fewer “empty” pixels in the FOV, the SENSE reconstruction algorithm would therefore exclude fewer voxels from unfolding during reconstruction, which

would lead to more voxels with significant aliasing and therefore higher geometry factors (Wiesinger et al., 2006; Pruessmann et al., 2006).

We simulated geometry factor maps for each combination of R_S = 1-7 x R_P = 1-7 and compared these to the measured g-factor maps from Experiment 1[18]. Figure 4.10 shows measured maps of R_P = 1-3 for R_S = 1.5 (left column) beside the corresponding simulated maps (right column). In general, simulated maps were in excellent agreement with the measured maps. Figure 4.11 shows representative difference volumes (Simulated - Measured). DIfferences between the measured and simulated *g*-volumes are largest in the edge slices where through-plane aliasing occurs. These are the only areas where the difference between simulation and measurement exceeds 0.2. Root mean squared deviation between measured and simulated maps averaged 0.12 across all trials.

When through-plane acceleration was high, the simulated maps tended to slightly overestimate the geometry factor in some areas. Under these conditions, simulated maps provide a conservative estimate of *g* in low-sensitivity areas. Therefore if a map simulated in this way achieves certain geometry factor values (i.e., $g < 2$) then it is reasonable to assume that *g* measured in data acquired with the same acceleration factors in a similar object would also satisfy that condition.

These results indicate that g-related noise enhancement patterns are independent across acceleration directions, and that multiplying “component”

[18] 14 matching combinations: RP = [1, 1.5, 2, 2.5, 3, 3.5, 4] for each of RS = 1.0 and 1.5)

maps allows reasonably accurate estimation of the geometry factor distribution within a given volume at arbitrary acceleration factors.

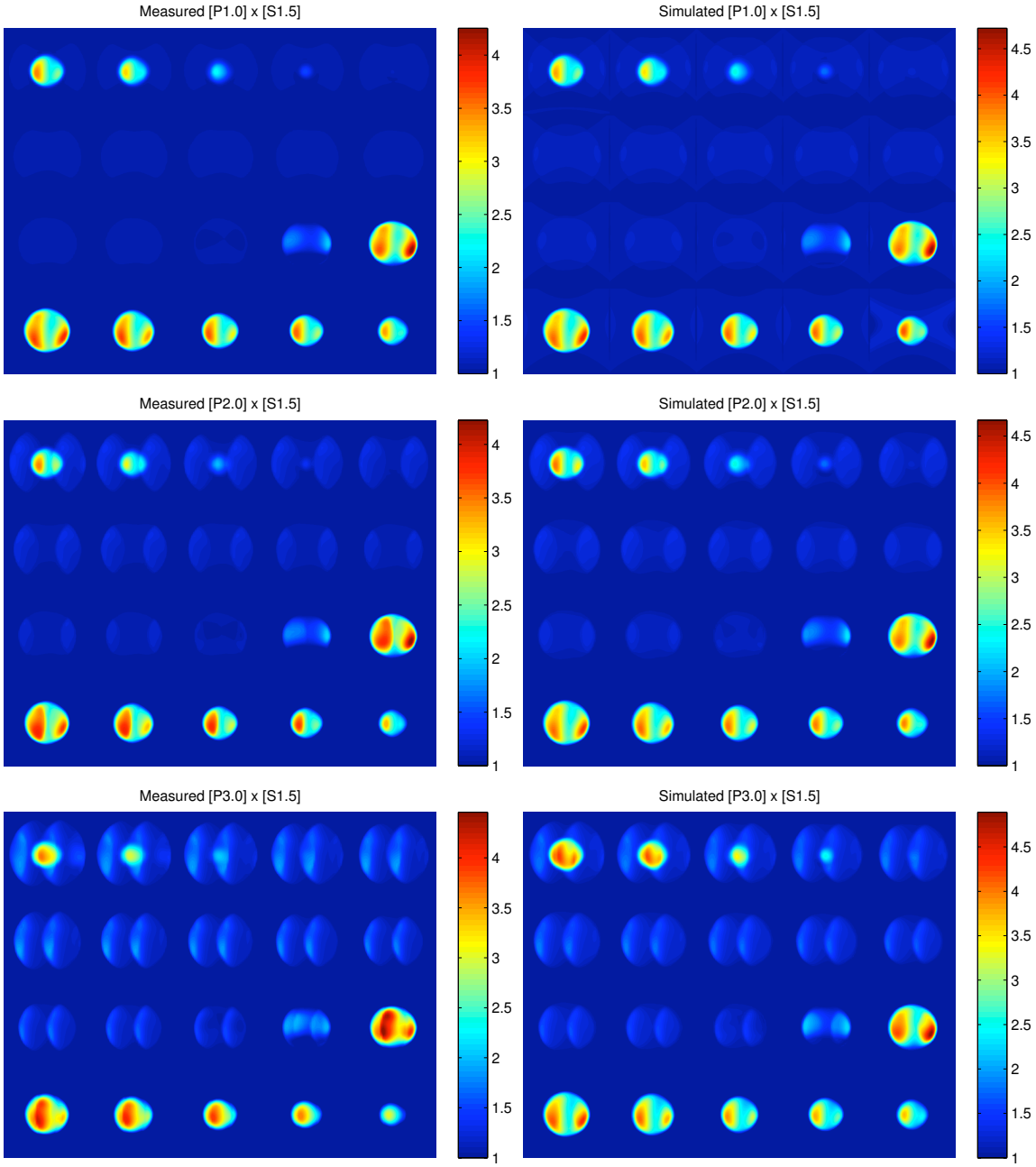

Figure 4.10: Measured (left column) and simulated (right column) geometry factor volumes for RP = 1-3 by RS = 1.5. In general there is excellent agreement between measured and simulated maps, though the simulations tend to slightly overestimate *g* in areas of high aliasing such as the edge slices.

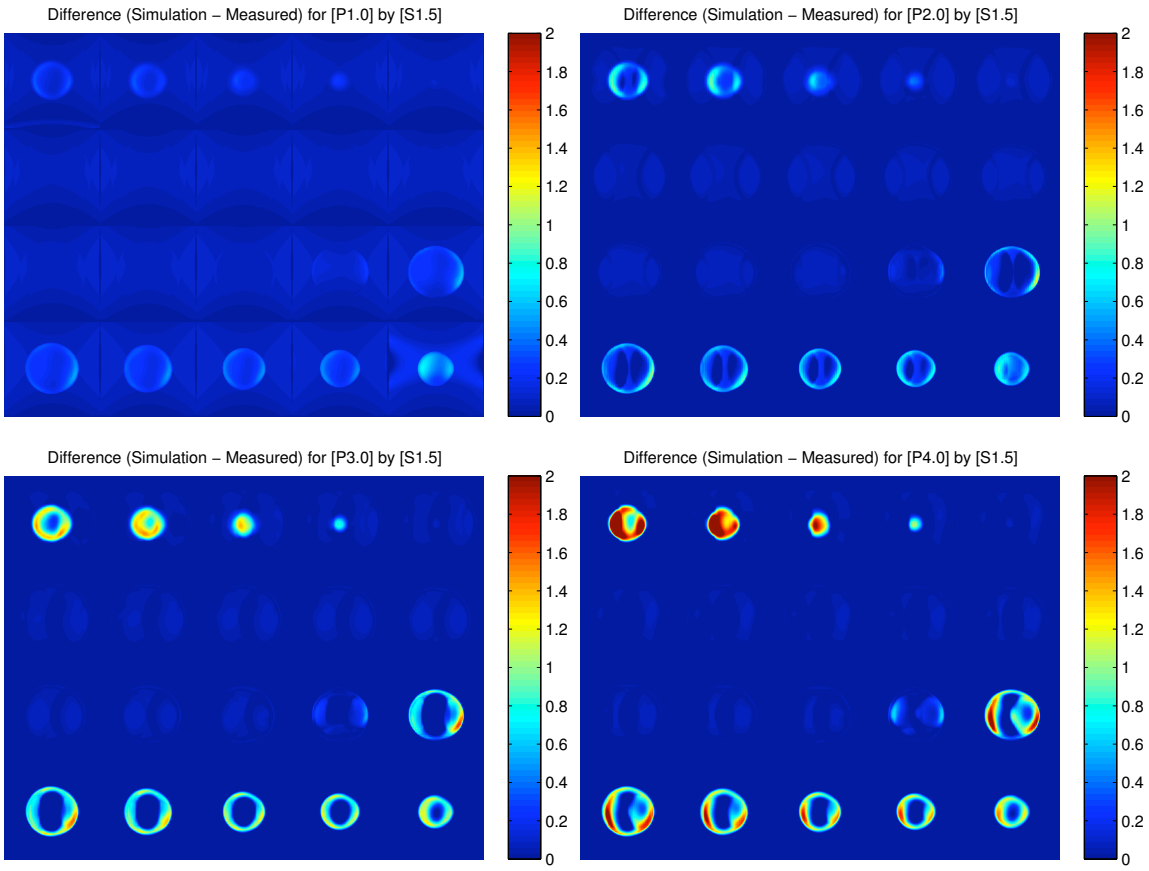

Figure 4.11: Difference of simulated minus measured geometry factor volumes for R_P = 1-4 by R_S = 1.5. The difference is nearly zero in central slices, only exceeding 0.2 on the edges where the degree of aliasing is high. The difference between simulated and measured maps only exceeds 1 in the very edge slices of $R_P = 4 \times R_S = 1.5$.

Figure 4.12 shows median values of each of the 169 geometry factor volumes (26 measured, 143 simulated) in the sphere phantom. In agreement with figure 4.7, peak g-values occur at $R_P = 7 \times R_S = 3.5$. This is a result of the aliasing patterns specific to our object and field of view. The corresponding *g* surface for the head phantom had the same shape, but slightly higher values as suggested by Figures 4.7 and 4.9.

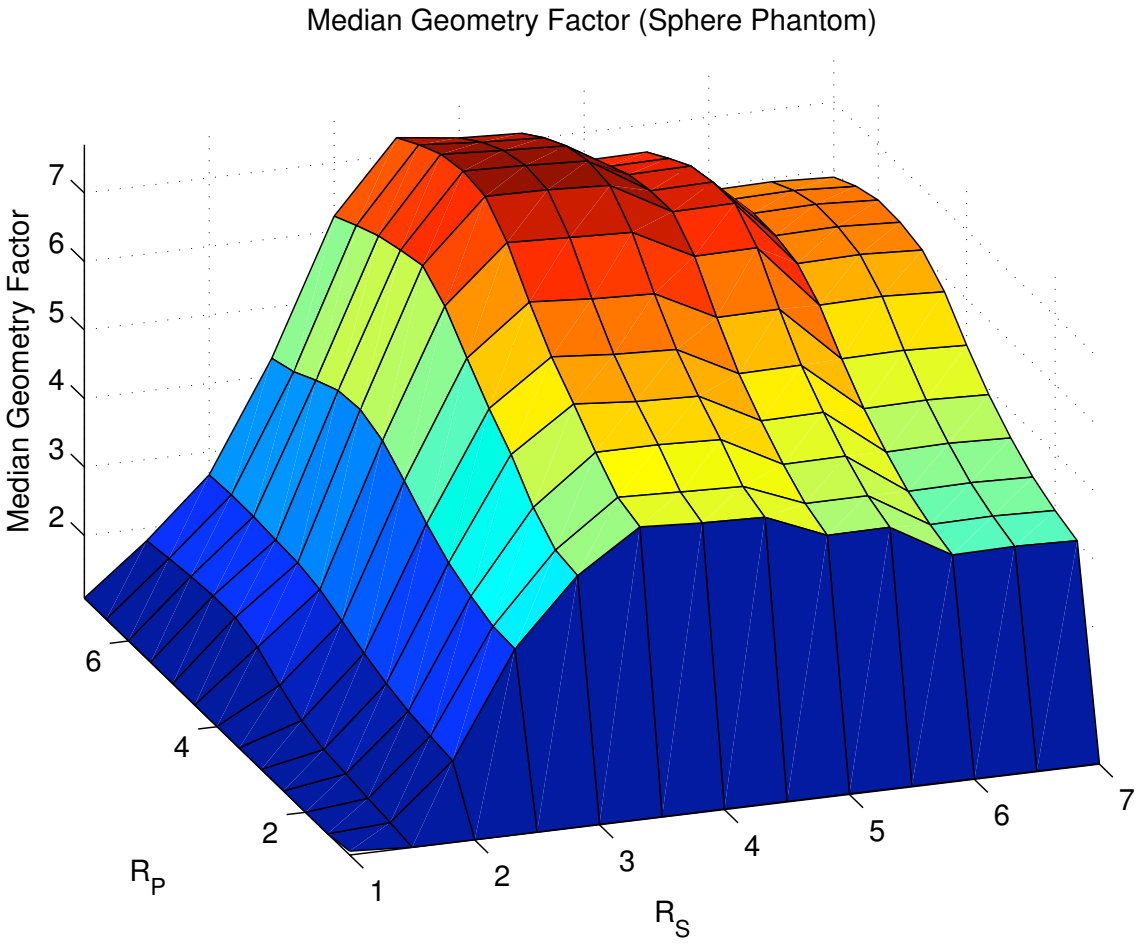

Figure 4.12: Median simulated geometry factor values for a spherical phantom as a function of R_P and R_S, for a 3D-FFE acquisition with 0.5 x 0.5 x 1mm^3 voxels, coronal slice orientation, and 128 x 128 x 20mm^3 FOV.

3.3. Results & Discussion for Experiment 3

Figure 4.13 shows geometry factor distributions for ten 3D-PRESTO scans acquired with the parameters shown in Tables 4.1-4.3. The entire range of geometry factors was within $g < 2$ for all scans except the Axial 3.5 x 3.5 x 3.5mm^3 scan with dynamic scan time of 0.2 seconds with $R_{total} = 12$. Meanwhile, all three Sagittal scans had total acceleration factors of $R > 9$, and yet geometry factors in these acquisitions were quite low. This is because the sagittal slice

orientation better aligns the phase encoding directions with the directions of more receive coil elements in the SENSE array as seen in Figures 4.4 and 4.5. Based on Figure 4.13, we would not expect any of the sequences listed in Tables 4.1 - 4.3, except for the 3.5 x 3.5 x 3.5mm^3, 0.2s scan, to experience significant g-related BOLD sensitivity losses in an fMRI experiment.

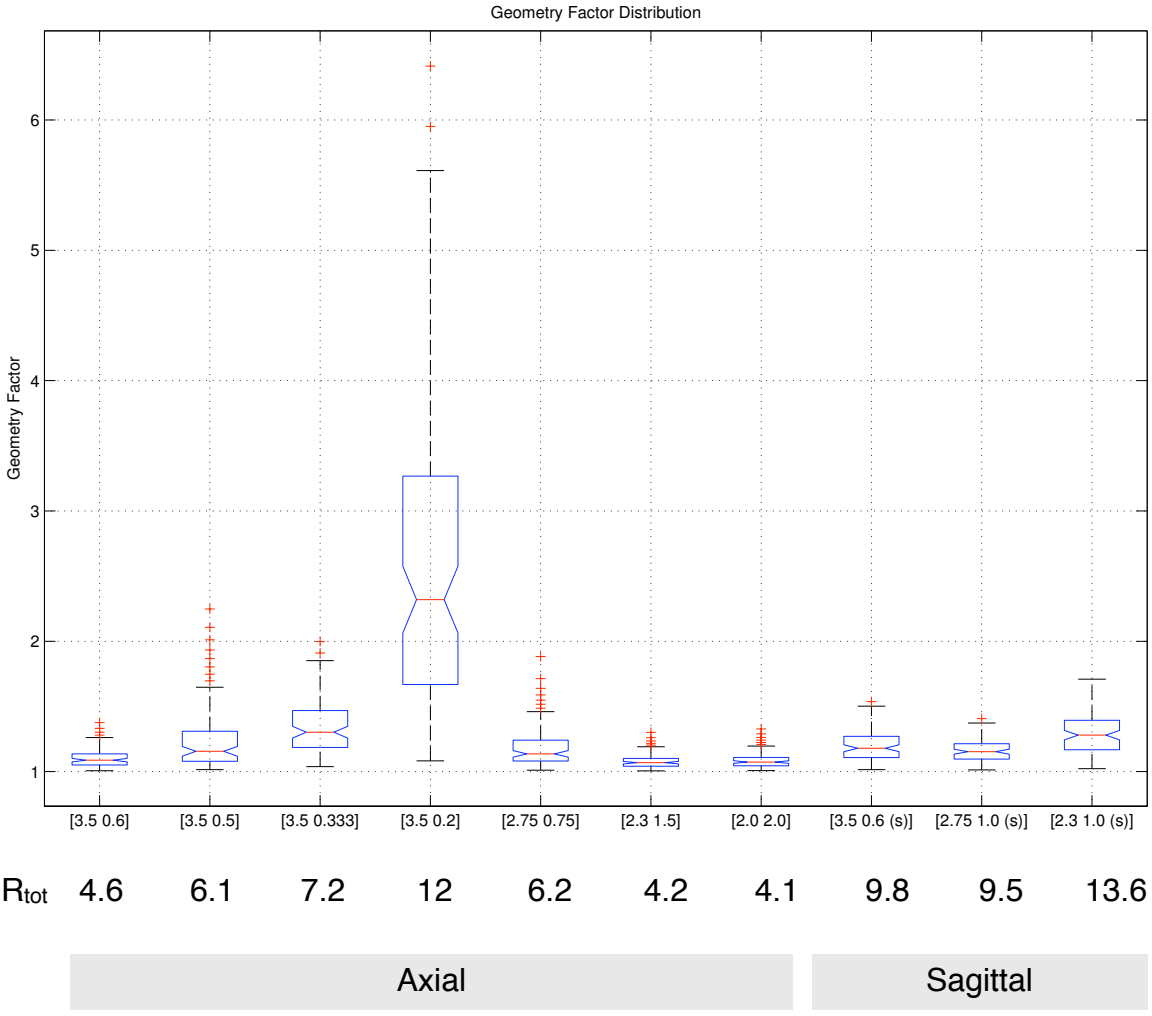

Figure 4.13: Geometry factor distributions for full-brain 3D-PRESTO sequences.

Figure 4.14 shows temporal SNR distributions for the same ten 3D-PRESTO scans (parameters shown in Tables 4.1-4.3). Comparing Figures 4.13 and 4.14 reveals that *g* is only partially responsible for TSNR. This is expected because multi-shot sequences such as 3D-PRESTO are inherently more sensitive to temporal signal instabilities. For example, the scan with by far the highest geometry factors in Figure 4.13 (scan #4) has only the second lowest TSNR. The Axial 2.3 x 2.3 x 2.3mm^3, 1.7s dynamic scan time has the lowest median TSNR even though this scan also features very low geometry factors, suggesting high inherent temporal signal variation in that particular sequence

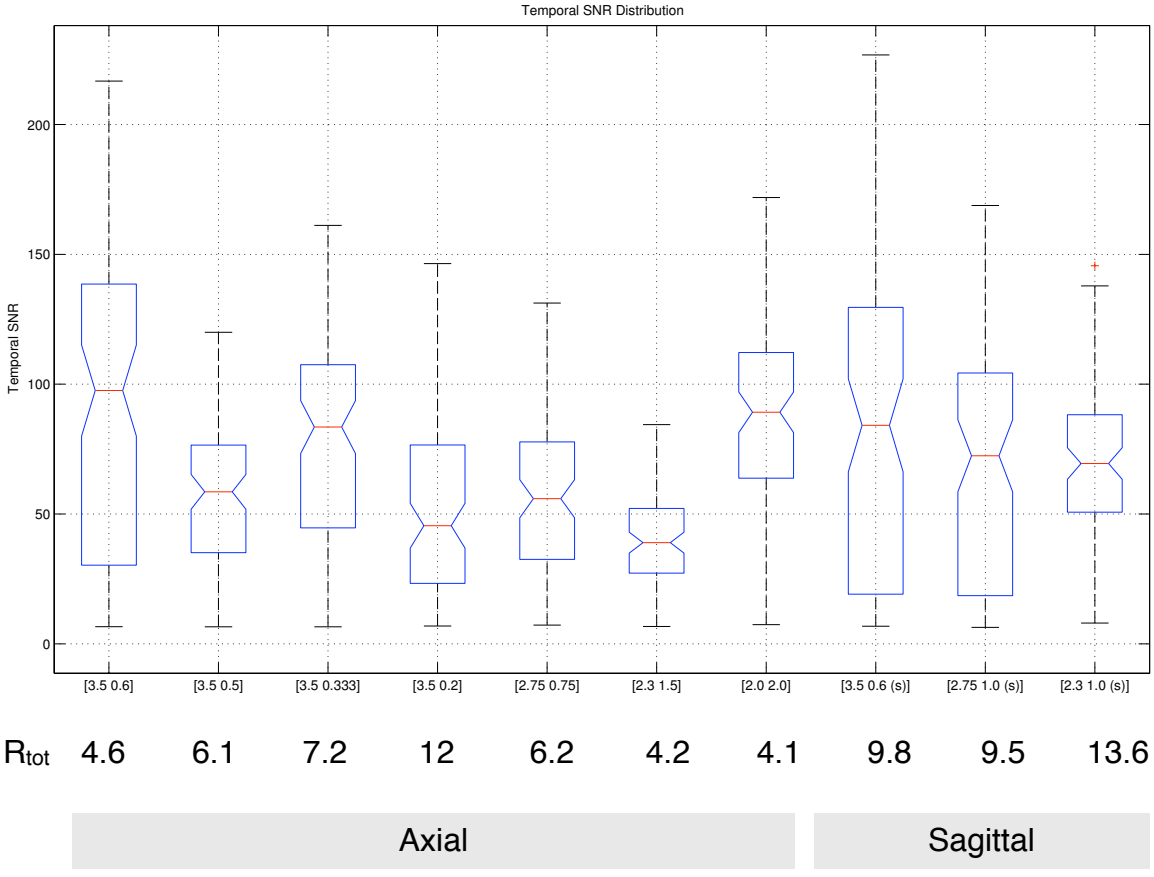

Figure 4.14: Temporal SNR distributions for full-brain 3D-PRESTO sequences.

Figure 4.15 plots the geometry factor vs. TSNR for all ten 3D-PRESTO scans tested here. Scans with the best performance are located in the bottom right, with low geometry factors and high TSNR. Scans with poor performance are located anywhere on the left side, where geometry factors are high and/or TSNR is low. This plot suggests the 3.5 x 3.5 x 3.5mm^3 scan with 0.6s dynamic scan time and R_{total} = 4.6, as well as the 2 x 2 x 2mm^3 scan with 2.0s dynamic scan time and R_{total} = 4.1 provide the highest TSNR and the lowest geometry factors. Next best is the 3.5 x 3.5 x 3.5mm^3 sagittal scan with 0.6s dynamic scan time and R_{total} = 9.8. The other Sagittal scans, which also have R_{total} > 9, generally show low geometry factors and sufficient TSNR for fMRI scans. Compare this to the single-accelerated 2D-EPI scans from Chapter III, in which *g* values started to grow exponentially around R = 5. This illustrates the benefit of distributing total acceleration across two phase encoding directions.

Figures 4.16 - 4.19 show g-maps (left) and TSNR maps (right) for three of the scans with good *g* and TSNR performance. In general, these results indicate that 3D-PRESTO offers several configurations for high temporal resolution, full brain coverage with low geometry factors and reasonable TSNR.

3.4. Results & Discussion for Experiment 4

Figure 4.17 shows the distribution of geometry factors in a 2D-EPI scan acquired at 1 x 1 x 2mm^3 for in-plane R_P acceleration ranging from 1.5-3 in increments of 0.1. For clarity, every third R-value is shown. The geometry factor grows predictably and remains within the favorable regime. We identify R = 2.6 as the highest acceleration value for which g < 2 everywhere in the imaging

volume at this specific combination of resolution, field of view, and object size. Note that even when some pixels have values of $g > 2$, the vast majority of pixels in the image remain within $g < 1.2$.

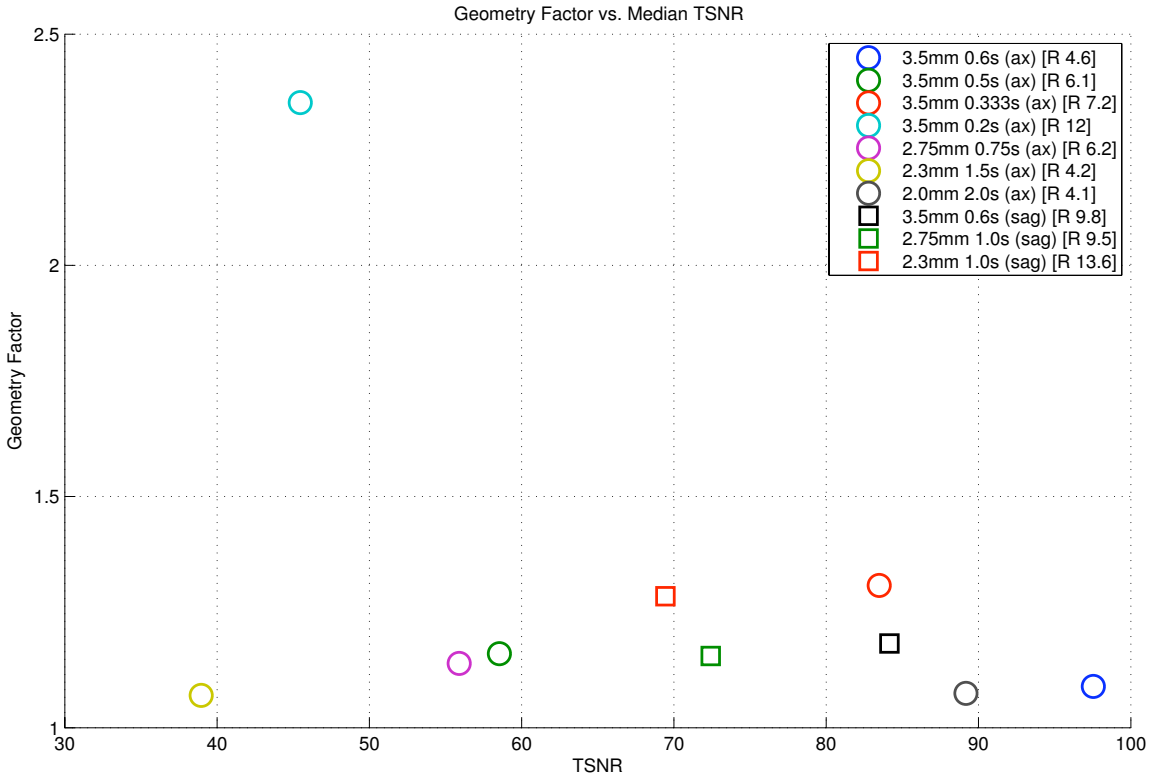

Figure 4.15: Plot of geometry factor vs. median TSNR for all ten 3D-PRESTO scans. The bottom right of the plot is the most favorable position, indicating low geometry factors and high TSNR.

3.5. Results & Discussion for Experiment 5

Figure 4.18 shows geometry factor volumes for a 3D-PRESTO scan with 224 x 176 x 100 mm FOV in Axial (left) and Sagittal (right) slice orientations with [25 slices x 4mm] (top), [50 slices x 2mm] (middle), [100 slices x 1mm] (bottom). Accelerations factors were fixed at RP = 2.4 and RS = 1.7 for all acquisitions.

Figure 4.19 shows the geometry factor distribution in all nine combinations of [number of slices, slice thickness] for both axial and sagittal slice orientations.

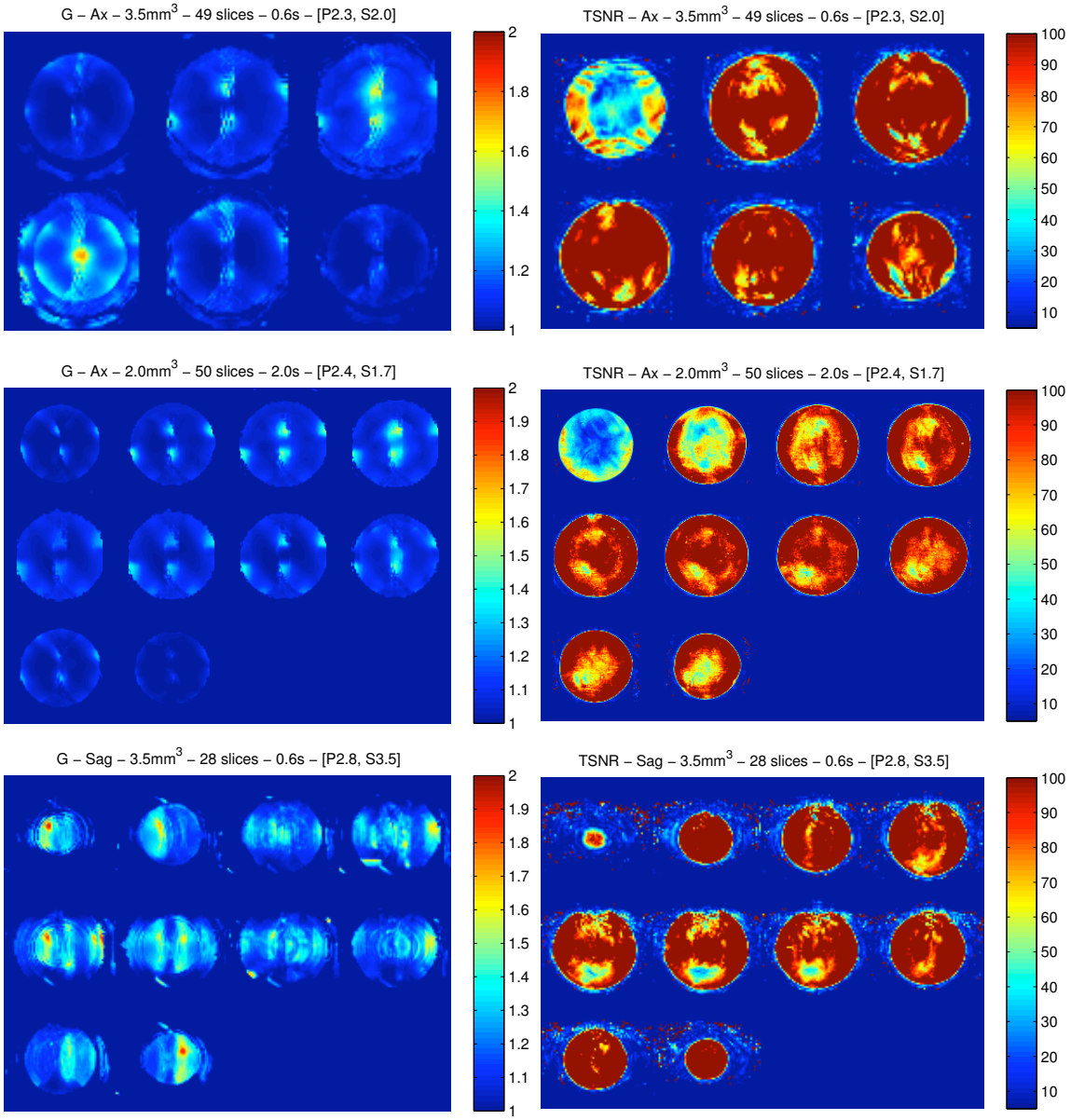

Figure 4.16: Geometry factor (left) and TSNR (right) distributions for three 3D-PRESTO scans which showed high TSNR and low geometry factors throughout the object. In the geometry factor maps, dark blue values indicate g-factors close to the ideal value of 1. In the TSNR maps, red pixels indicate high TSNR values of 100 or greater. To save space, every 4th slice is shown.

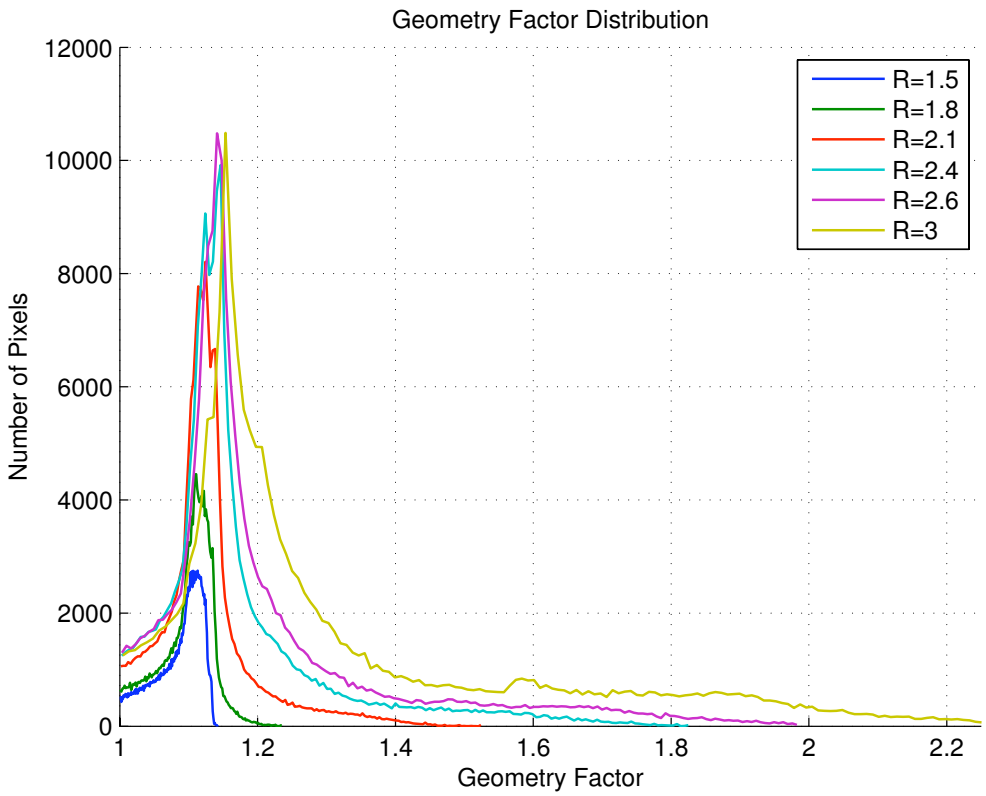

Figure 4.17: Distribution of $g > 1$ in a 1 x 1 x 1mm^3 2D-EPI scan with in-plane acceleration ranging from R = 1-3. R = 2.6 is the highest acceleration value for which $g < 2$ throughout the volume.

The distribution of geometry factor does not change with slice / slab thickness so long as the field of view remains constant. We observe the same general distribution of *g* throughout the volume whether we used many thin slices or fewer thick slices in both orientations.

Despite having the same field of view, object size, acceleration factors and resolution, the Sagittal scans showed significantly lower geometry factors at every slice/thickness combination. This is expected because the sagittal orientation aligns better with the layout of the coil elements of our receiver array (see Figure 4.4).

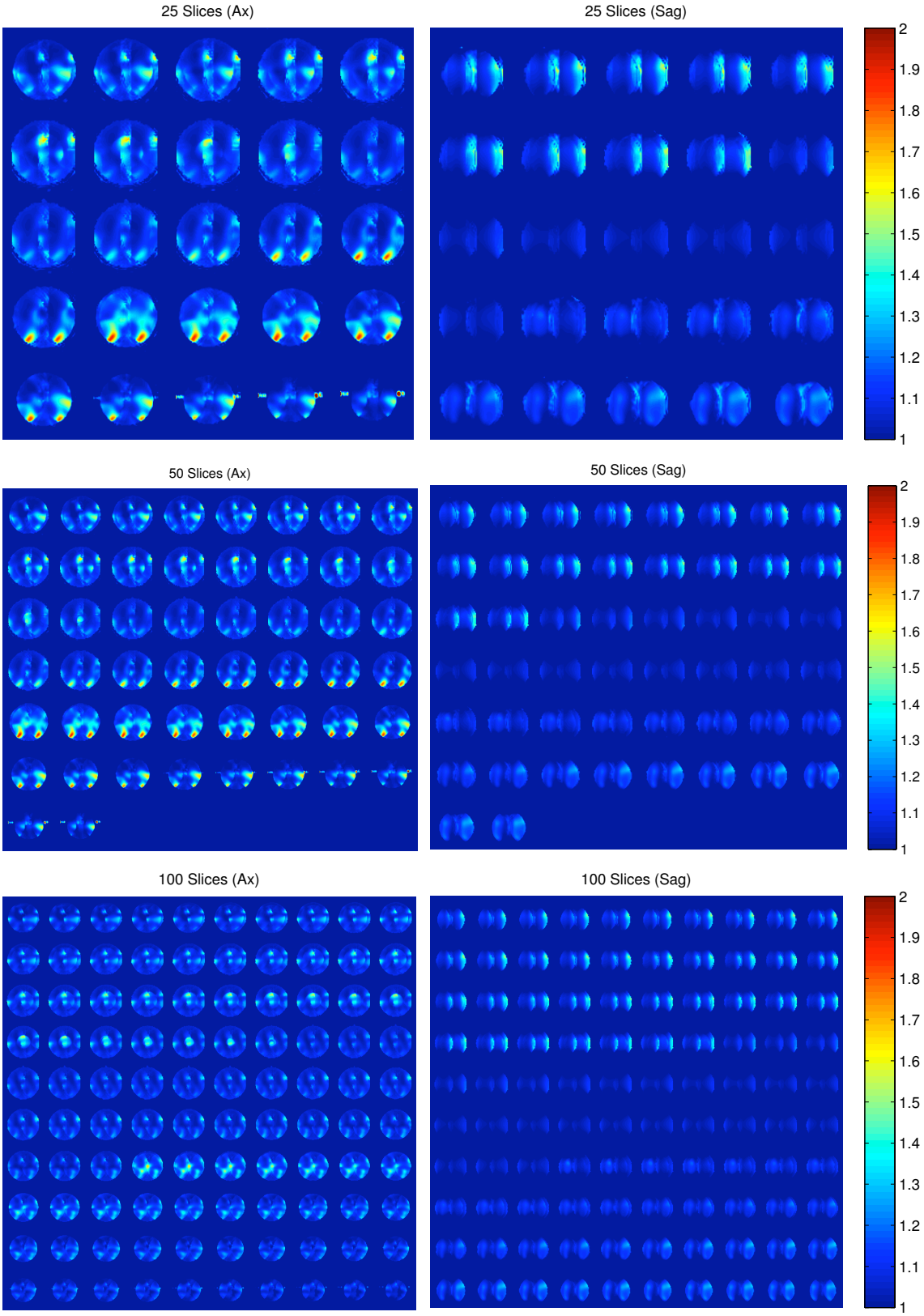

Figure 4.18: Geometry factor volumes for 3D-PRESTO acquisition. Axial (left) and sagittal (right), 224 x 176 x 100mm^3 field of view, with R_P = 2.4 and R_S = 1.7.

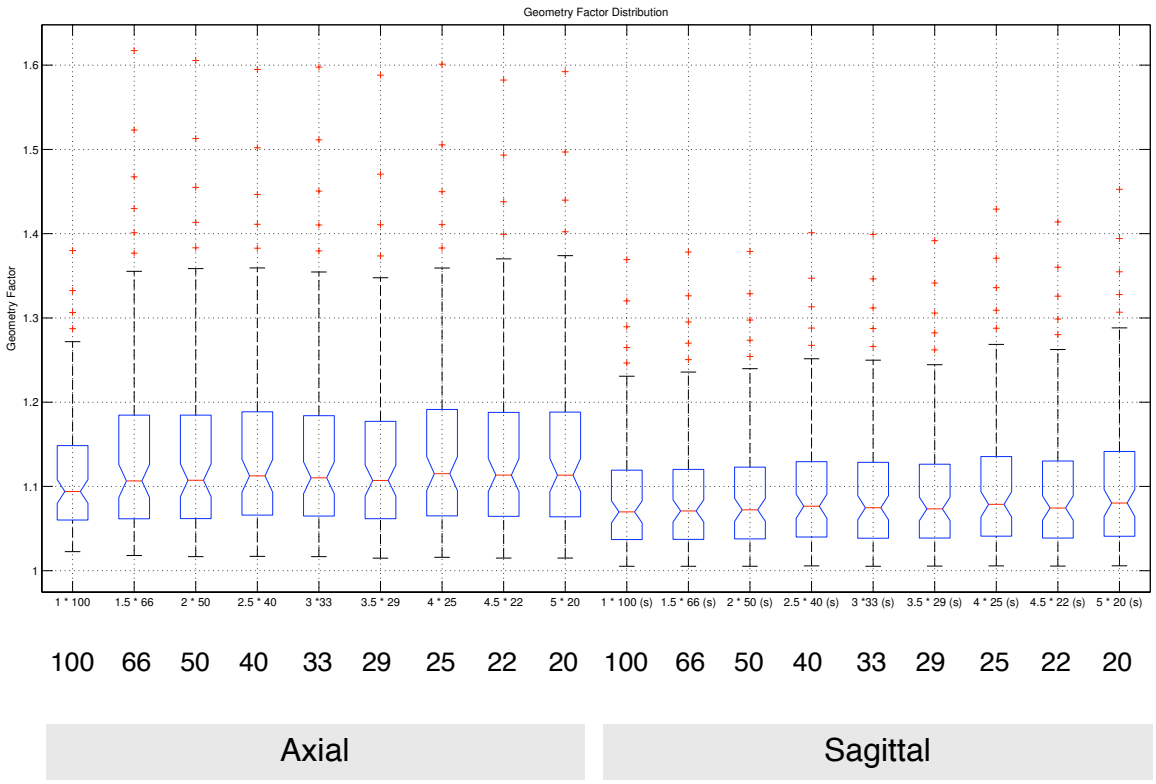

Figure 4.19: Geometry factor distributions for Axial and Sagittal acquisitions with a 224 x 176 x 100 mm field of view and variable number of slices and slice thickness. Numbers below the plot indicate the number of slices. Acceleration factors were $R_P = 2.4$ x $R_S = 1.7$ for all scans. Although all acquisitions maintained $g < 2$ throughout the volume, Sagittal images showed significantly reduced geometry factors compared to Axial images.

Note the small decrease in the geometry factor distribution for the Axial acquisition with 100 slices of 1mm thickness (scan #1). This could be because with very thin slices the geometry factor is more evenly distributed and therefore does not lead to hotspots as observed in the other acquisitions. While we do not observe this in the Sagittal images, it could be that the geometry factors were already low enough that such an effect may not be apparent.

3.6. Results & Discussion for Experiment 6

Figure 4.20 compares geometry factor distributions between humans and phantoms in 2D-EPI, 3D-FFE, and 3D-PRESTO at all five resolutions considered for the retinotopic mapping experiment (1 x 1 x 1mm^3, 1.12 x 1.12 x 1.12mm^3, 1.67 x 1.67 x 1.67mm^3, 2 x 2 x 2mm^3 and 3 x 3 x 3mm^3). Panels (a) and (b) compare geometry factors in humans (black) and phantoms (red) for (a) 2D-EPI and (b) 3D-FFE / 3D-PRESTO. Geometry factors are nearly identical between humans and phantoms at all resolutions except 1 x 1 x 1mm^3, where human g-factors tended to be higher. Panels (c) and (d) compare geometry factors in (c) phantoms and (d) humans for 2D-EPI (black) and 3D-FFE / 3D-PRESTO (red). As expected from the generally higher R values 2D-EPI compared to the 3D sequences, *g* tended to be higher in 2D-EPI compared to 3D-FFE / 3D-PRESTO at each resolution. In fact, the 1 x 1 x 1mm^3 2D-EPI scan with R = 2.4 showed significantly higher geometry factors than 3D-FFE with R = 2.7 while all other parameters except TR, dynamic scan time, and echo train length were equal. See Table 4.4 for a full scan parameters. Figure 4.21 compares g-factor maps for the 1 x 1 x 1mm^3 2D-EPI and 3D-FFE scans.

Median geometry factors remain below 1.3 for all sequences, though in the 1 x 1 x 1mm^3 acquisitions at least 25% of the geometry factors were approximately 1.5 or above for both 2D-EPI and 3D-FFE. We observe similar geometry factor distributions across both humans and phantoms, across different days, and between 2D-EPI, 3D-FFE, and 3D-PRESTO. Therefore we expect all

of the 1.12 x 1.12 x 1.12mm^3 - 3 x 3 x 3mm^3 scans presented here to yield geometry factors within acceptable limits for fMRI experiments.

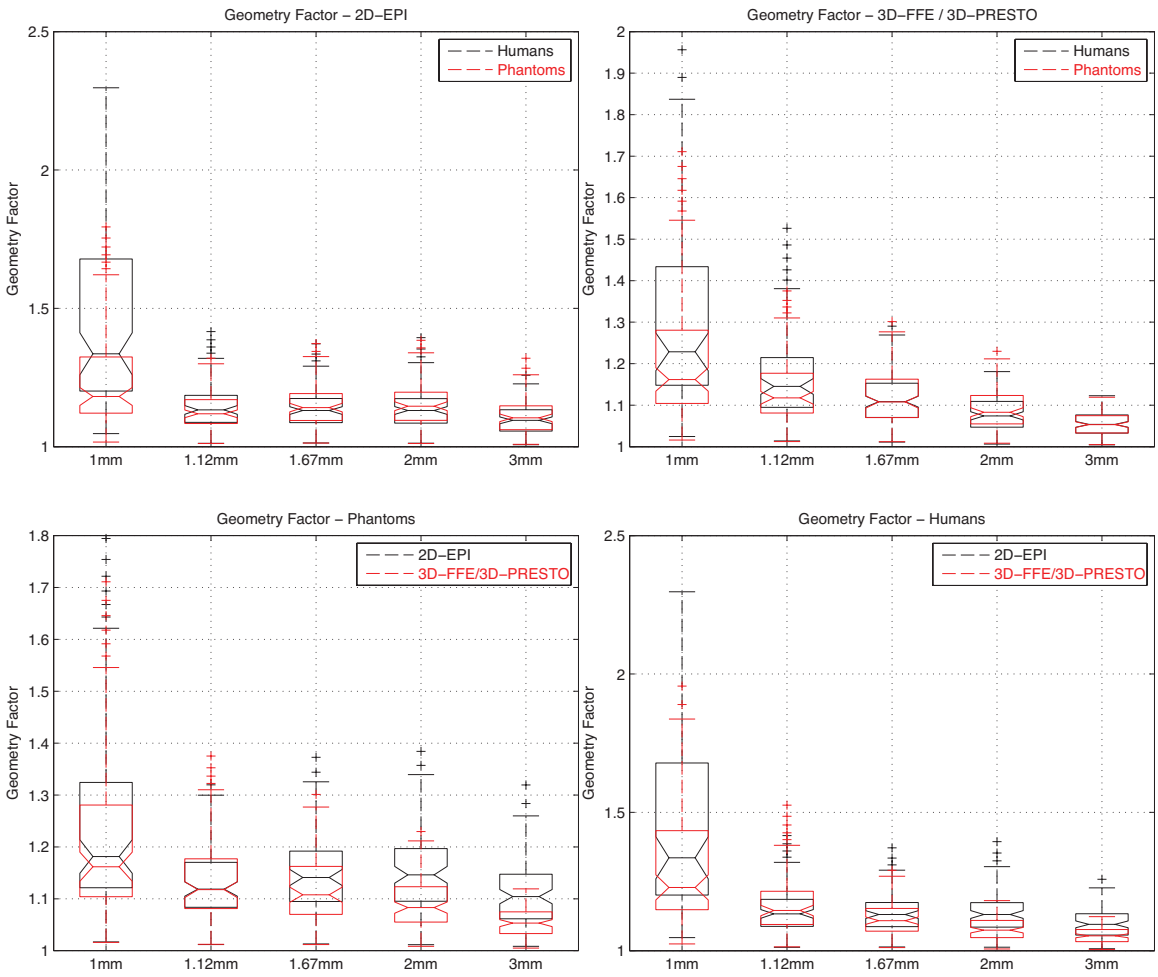

R_{EPI}	2.4	2.4	2.7	2.7	2.6		2.4	2.4	2.7	2.7	2.6
R_{3D}	2.7	2.6	2.6	2.2	1.8		2.7	2.6	2.6	2.2	1.8

Figure 4.20: Geometry factor distributions for 2D-EPI, 3D-FFE, and 3D-PRESTO in humans and phantoms. (a) Humans (black) and phantoms (red) for 2D-EPI. (b) Humans (black) and phantoms (red) for 3D-FFE (1 x 1 x 1mm^3 - 1.67 x 1.67 x 1.67mm^3) and 3D-PRESTO (2 x 2 x 2mm^3 - 3 x 3 x 3mm^3). (c) Phantoms for 2D-EPI (black), 3D-FFE (red, 1 x 1 x 1mm^3 - 1.67 x 1.67 x 1.67mm^3) and 3D-PRESTO (red, 2 x 2 x 2mm^3 - 3 x 3 x 3mm^3). (d) Humans for 2D-EPI (black), 3D-FFE (red, 1 x 1 x 1mm^3 - 1.67 x 1.67 x 1.67mm^3) and 3D-PRESTO (red, 2 x 2 x 2mm^3 - 3 x 3 x 3mm^3).

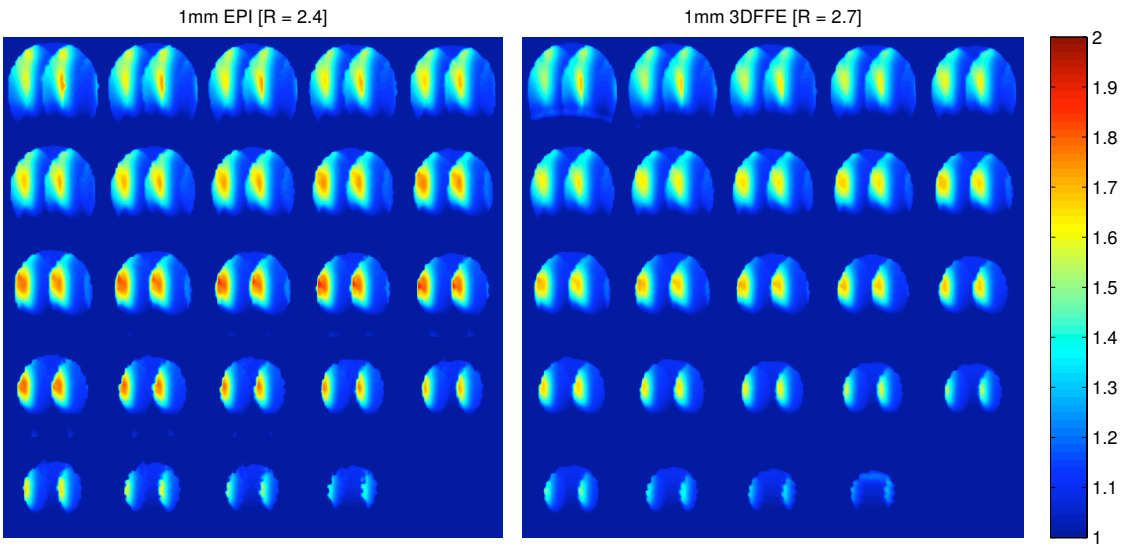

Figure 4.21: Geometry factor distributions for 2D-EPI (left) and 3D-FFE (right) in a spherical phantom at 1 x 1 x 1mm^3. The 2D-EPI scan has higher geometry factors with R = 2.4 than the 3D-FFE scan does with R = 2.7. All other scan parameters except TR are equal (see Table 4.4).

Figure 4.22 compares temporal signal to noise between humans and phantoms in 2D-EPI, 3D-FFE, and 3D-PRESTO at all five resolutions. Panels (a) and (b) compare TSNR in humans (black) and phantoms (red) for (a) 2D-EPI and (b) 3D-FFE / 3D-PRESTO. For both 2D and 3D acquisitions, TSNR is on average 4-5 times higher in phantoms than in humans at all resolutions. This difference is consistent with our observations in Chapter III and owes primarily to motion and physiological effects in humans. For a given scan type, TSNR increases across resolutions in a similar fashion for both humans and phantoms, but the 2D-EPI scans show a much greater TSNR increases at larger voxel sizes compared to the 3D scans. This difference owes to increased temporal instability in the 3D scans which may be due to physiological noise or shot-to-shot instability.

Figure 4.22 panels (c) and (d) compare TSNR in (a) phantoms and (b) humans for 2D-EPI (black), 3D-FFE/3D-PRESTO (red). In phantoms (a), 3D-FFE shows slightly but significantly higher TSNR than 2D-EPI at 1 x 1 x 1mm^3 and 1.12 x 1.12 x 1.12mm^3. In humans (b), the additional variability eliminates this advantage, yielding virtually identical TSNR in 2D-EPI and 3D-FFE. At 1.67 x 1.67 x 1.67 - 3 x 3 x 3mm^3 resolutions, 2D-EPI shows significantly higher TSNR than 3D-FFE and 3D-PRESTO in both humans and phantoms, though the difference is larger in phantoms. This could be because the theoretically more stable single-shot acquisition of 2D-EPI may benefit more from the absence of physiological noise than 3D-FFE or 3D-PRESTO, which will still experience shot-to-shot variations.

4. Conclusions

The broad aim of this study was to generate a variety of fMRI imaging sequences with 2D-EPI, 3D-FFE, and 3D-PRESTO, optimized for both high resolution, limited FOV and low resolution, full FOV scans. There were a number of constraints on this problem: the resulting sequences must have dynamic scan times short enough for fMRI experiments, isotropic voxel dimensions, $g < 2$ throughout the imaging volume, and adequate coverage for both retinotopic mapping and full brain fMRI scans at a variety of different resolutions.

Parallel imaging techniques are critical in obtaining an optimal trade-off between SNR, scan time, resolution, volume coverage, and magnetic susceptibility effects in fMRI scans, especially at high field. The SNR penalty in

scans with a high net reduction is largely determined by the spatially varying geometry factor which is highly specific to individual scanner, coil array, object, and field of view.

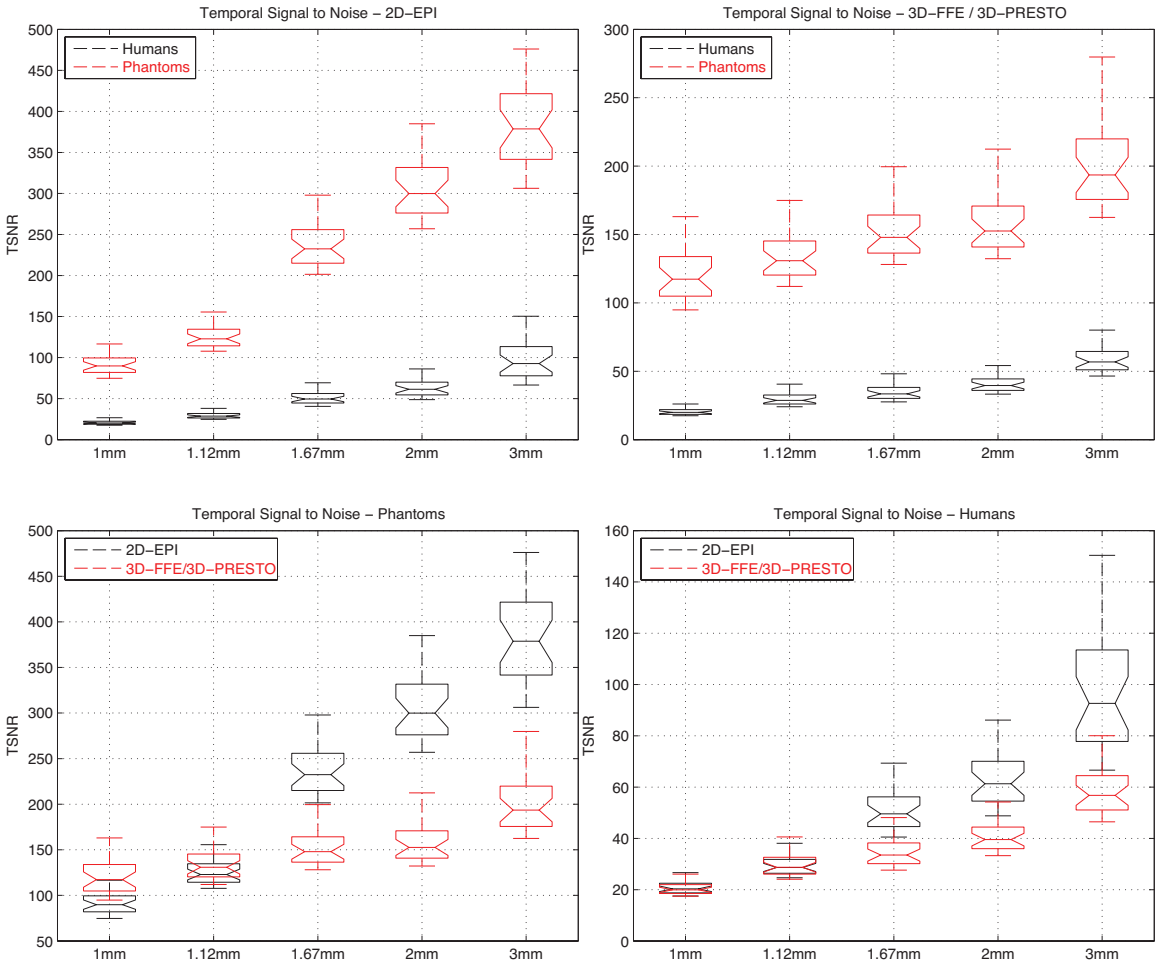

Figure 4.22: Temporal signal to noise ratios for 2D-EPI, 3D-FFE, and 3D-PRESTO in humans and phantoms. (a) Humans (black) and phantoms (red) for 2D-EPI. (b) Humans (black) and phantoms (red) for 3D-FFE (1 x 1 x 1mm^3 - 1.67 x 1.67 x 1.67mm^3) and 3D-PRESTO (2 x 2 x 2mm^3 - 3 x 3 x 3mm^3). (c) Phantoms for 2D-EPI (black), 3D-FFE (red, 1 x 1 x 1mm^3 - 1.67 x 1.67 x 1.67mm^3) and 3D-PRESTO (red, 2 x 2 x 2mm^3 - 3 x 3 x 3mm^3). (d) Humans for 2D-EPI (black), 3D-FFE (red, 1 x 1 x 1mm^3 - 1.67 x 1.67 x 1.67mm^3) and 3D-PRESTO (red, 2 x 2 x 2mm^3 - 3 x 3 x 3mm^3).

Central to achieving our aim was to determine the geometry factor distributions under a number of different conditions for our specific 7T, 16-channel head coil configuration for 2D and 3D acquisitions. We have presented six experiments designed to address this issue in a number of ways. Our findings can be summarized as follows:

1. Slice orientation, coil geometry, and field of view are all critical determinants of the volume distribution of geometry factors for a given degree of reduction.

2. Through-plane acceleration leads to complicated aliasing patterns that can lead to g-factor hotspots that depend on the object size and slice position within the FOV. The location and magnitude of these areas of high *g* can be difficult to predict in limited field of view studies.

3. It is possible to simulate reasonably accurate geometry factor volumes with arbitrary combinations of 2D acceleration through the multiplication of "component" geometry factor maps. These maps can generally be acquired within one scan session. This method could expedite determination of the optimal combination of 2D acceleration factors in 3D acquisitions.

4. Several 3D-PRESTO scans tested in Experiment 3 yielded full brain coverage with high temporal resolution, low geometry factors and high

TSNR. Therefore 3D-PRESTO appears to be a good candidate for fast, full brain fMRI at 7T.

5. For our 16 channel receiver coil array, the sagittal slice orientation allows for maximal acceleration with minimal geometry factors because it best aligns with our receiver array configuration. In Experiment 3 we showed that is possible to obtain sagittal scans with $R_{total} > 9$ yet still maintain $g < 2$ and median TSNR > 70. In some cases, it may be worthwhile acquiring sagittal 3D data and then re-slicing into other planes.

6. Experiment 4 showed that the highest value of in-plane acceleration in a 1 x 1 x 1mm^3 2D-EPI scan for which $g < 2$ throughout the imaging volume was 2.6. However, the vast majority of voxels still had $g < 1.2$. This value could be pushed significantly higher if some pixels were allowed to have $g > 2$.

7. Experiment 5 showed that the spatial distribution of geometry factor does not depend on the number of slices or slice thickness for a fixed field of view.

8. Experiment 5 also showed, in agreement with the results from Experiment 3, that sagittal scans generally have significantly lower geometry factors than axial scans, even if acceleration values and the FOV are the same.

9. The 1 x 1 x 1mm^3 acquisitions tested in Experiment 6 produced geometry factors and TSNR which were too close to our acceptable limits. Moving to 1.12 x 1.12 x 1.12mm^3 with slightly less acceleration solved the problem. It is likely that a receiver coil array with 32 channels would provide the signal-to-noise increases necessary to acquire high quality fMRI data at 1 x 1 x 1mm^3.

10. When acquisition parameters are similar, 2D-EPI tended to show slightly higher geometry factors than 3D-FFE (see Figures 4.23 and 4.24).

11. In agreement with the findings of Chapter III, this study shows that TSNR in human scans is generally 4-5 times lower than corresponding phantoms scans. This could mean the contribution of physiological noise to temporal signal variation is roughly 4-5 larger than that of thermal noise. Chapter III dealt exclusively with the case of 2D-EPI, and these results show the same pattern with 2D-EPI, 3D-FFE, and 3D-PRESTO.

12. In humans, 3D-FFE has TSNR roughly equal to or better than than of 2D-EPI at voxel volumes of 1 x 1 x 1mm^3 and 1.12 x 1.12 x 1.12mm^3. Meanwhile 2D-EPI has significantly higher TSNR than 3D-FFE or 3D-PRESTO at larger voxel volumes.

13. Measured geometry factors were stable and reproducible over time and across various scan configurations. This is expected since *g* is mostly

determined by coil geometry and sensitivity profiles which should not change appreciably over time. Thus for a given orientation, FOV, object and slice placement, one could expect *g* measurements to remain valid across the span of an experiment.

Geometry factor data are rarely described in published fMRI studies, perhaps because the process of reconstructing and exporting g-maps is not straightforward on all scanners. However, because large *g* can limit the quality of fMRI results, it is advisable to confirm that $g < 2$ in areas of functional interest before undertaking costly and time consuming studies with human subjects. Because *g* changes throughout the object, the full volume distribution of the geometry factor must be considered; that is, reporting only a mean or median value for *g* generally will not be sufficient to characterize scan performance.

While splitting the acceleration factor across both phase encoding directions in a 3D acquisition may result in lower geometry factors in some situations, our findings show it is critical to account for slice orientation, field of view, object shape and receiver coil array geometry when choosing acceleration factors, especially in limited field of view studies that are common at 7T.

Acquiring individual geometry factor maps for every combination of acceleration factors in a given field of view is impractical. Instead, collecting “component” maps and simulating other possible combinations as described in Experiment 2 is an efficient method to survey the effects of many combinations of acceleration factors before collecting fMRI data. This method can be applied to

any range of R values and could expedite optimization of 3D fMRI scans. The component maps necessary to simulate additional maps can generally be acquired within one scan session.

Though SENSE is most commonly used to decrease scan time, Weiger et al. (2002) suggest that in certain circumstances it might be beneficial to maintain constant imaging time while increasing the imaging volume. This might be particularly useful in the cases of narrow-slab, high resolution studies of the visual cortex. With 3D acquisition, larger slab sizes lead to increased SNR which can offset the $\sqrt{R}$ SNR losses due to reduced k-space sampling. The geometry factor also tends to decrease as the imaging volume increases, meaning that the net SNR penalty for using SENSE to increase the imaging volume should be very small. If scan time reduction is not required to meet the requirements of a given study, using acceleration to increase the imaging volume in a 3D acquisition could be a powerful, currently under-utilized application of SENSE.

Another study by Weiger et al. (2005) has demonstrated the potential for SENSE to enhance the SNR efficiency (SNR per unit time) of short-TR sequences, or any sequence for which increasing TR also increases the acquisition duty cycle or available transverse magnetization. This is accomplished by balancing potential scan time savings with increased TR. The 3D-FFE and 3D-PRESTO sequences tested here generally have very short TR and fall into this category. When SENSE can be applied in two dimensions, the options for this approach increase as well. An additional consideration, raised by Constable and Spencer (2001), is that short volume TR times ($TR_{vol} < 1.5s$) are

beneficial for statistical power and fMRI sensitivity even when the raw SNR of the images in the series is lower when compared to a longer volume TR time (TR_{vol} > 4s). Together these suggest that a sequence with short volume TR times and longer sequence TR times would have high SNR efficiency and and high fMRI sensitivity, even if the image SNR was somewhat low. In the following chapter, we show that accelerated 3D-PRESTO fits this description rather well.

The sequences generated in Experiment 6 are applied to a retinotopic mapping study in the next chapter. Others, such as the full-brain 3D-PRESTO scans from Experiment 4, are ready to be applied to fast, full-brain functional imaging studies.

Finally, as suggested in Chapter III, the best way to reduce geometry factors for all scan types, slice orientations and fields of view is to obtain receiver coil arrays with more elements and to ensure the elements are arranged to allow for maximum flexibility in the application of acceleration.

Table 4.1: Low-resolution axial full-brain 3D-PRESTO scans.

3D-PRESTO	Axial			
Resolution (mm^3)	3.5 x 3.5 x 3.5			
Dyn. Scan Time (s)	0.6	0.5	0.333	0.2
Field of View (mm^3)	224x182x98	224x182x105	224x182x98	224x182x98
Rec. FOV (%)	82	82	82	82
Slices	28	30	28	28
TR (ms)	15	16	15	15
TE (ms)	(8) 23	(7) 23	(8) 23	(8) 23
R_P (RL)	2.3	2.3	4	4
R_S (FH)	2	2.7	1.8	3
R_{Total}	4.6	6.1	7.2	12
Flip Angle	10	10	10	10
BW_{freq}	4186	4193	4193	4196
BW_{phase}	170	171	170	170
Echo Train	13	13	13	13

Table 4.2: Medium-resolution axial full-brain 3D-PRESTO scans.

3D-PRESTO	**Axial**		
Resolution (mm^3)	2.75 x 2.75 x 2.75	2.3 x 2.3 x 2.3	2 x 2 x 2
Dyn. Scan Time (s)	0.75	1.7	2.0
Field of View (mm^3)	220 x 176 x 110	220 x 175 x 110	224 x 176 x 100
Rec. FOV (%)	80	80	79
Slices	40	48	50
TR (ms)	15	16	16
TE (ms)	(8) 23	(8) 24	(7) 23
R_P (RL)	2.7	2.1	2.4
R_S (FH)	2.3	2.0	1.7
R_{Total}	6.21	4.2	4.08
Flip Angle	10	10	10
BW_{freq}	3209	2632	2187
BW_{phase}	146	129	101
Echo Train	13	13	13

Table 4.3: Medium-resolution sagittal full-brain 3D-PRESTO scans.

3D-PRESTO	**Sagittal**		
Resolution (mm^3)	3.5 x 3.5 x 3.5	2.75 x 2.75 x 2.75	2.3 x 2.3 x 2.3
Dyn. Scan Time (s)	0.6	1.0	1.1
Field of View (mm^3)	220 x 220 x 172	220 x 220 x 179	220 x 220 x 181
Rec. FOV (%)	100	100	100
Slices	49	65	79
TR (ms)	15	15	16
TE (ms)	(8) 23	(8) 23	(8) 24
R_P (AP)	2.8	3.4	4
R_S (RL)	3.5	2.8	3.4
R_{Total}	9.8	9.52	13.6
Flip Angle	10	10	10
BW_{freq}	5540	4470	3744
BW_{phase}	167	152	140
Echo Train	13	13	13

Table 4.4: Acquisition parameters for proposed retinotopic mapping sequences.

Res. (mm^3)	Coronal									
	1 x 1 x 1		1.12 x 1.12 x 1.12		1.67 x 1.67 x 1.67		2 x 2 x 2		3 x 3 x 3	
Seq.	2D-EPI	3D-FFE	2D-EPI	3D-FFE	2D-EPI	3D-FFE	2D-EPI	3D-PRS	2D-EPI	3D-PRS
FOV (mm^3)	144x144x30		144x144x28		160x160x40		160x160x40		192x192x60	
TE (ms)	22							(6) 26	22	(7) 22
TR (ms)	3600	39.47	2880	41.66	2880	31	2400	19.23	2400	15.38
T_{Dyn} (ms)	3600	4500	2880	4000	2880	2880	2400	1500	2400	1200
Slices	30	30	25	25	24	24	20	20	20	20
R_{RL}	2.4	2.7	2.4	2.6	2.7	2.6	2.7	2.2	2.6	1.8
BW_{phase}	17	57.5	21.2	62.7	41.3	101.3	55.2	114.1	79.7	144.7
BW_{freq}	1406	1398	1580	1571	2333	2199	2793	2610	4163	4103
ETL	63	17	55	17	37	13	31	13	27	13
Dyns	80	64	100	72	100	100	120	192	120	240
Flip	80	20	80	20	80	10	80	10	80	10

CHAPTER V

COMPARISON OF IMAGING SEQUENCES FOR FMRI AT 7T

1. Introduction

High field MRI scanners operating at 7T or above are finding increasing use in studies of brain function. In theory, increasing the main magnetic field (B_0) leads to increases in the signal-to-noise ratio (SNR) of magnetic resonance images and to increased contrast from blood oxygen level dependent (BOLD) effects in functional MRI (fMRI) experiments (Duong et al., 2003; Haacke et al, 1999). However, at present, the theoretical benefits of high field functional imaging have not been fully or widely realized. This is due in part to technical limitations on the quality of images acquired using the pulse sequence which is most commonly used for fMRI, single-shot multi-slice gradient-echo Echo Planar Imaging (EPI) (De Zwart et al., 2002; De Zwart et al., 2006). Though EPI methods have advantages over other sequences in theory, they suffer in practice from detrimental effects of susceptibility variations at high field. With the advent of parallel imaging, other fast imaging methods which are less sensitive to off-resonance effects become feasible. Here we compare the performance of 3D Fast Field Echo (3D-FFE) and 3D-PRESTO (Principles of Echo Shifting with a Train of Observations) (Liu et al., 1993; van Gelderen et al., 1995) sequences as alternatives to 2D-EPI for functional imaging in a polar angle retinotopic mapping task at 7T.

Retinotopic mapping with functional MRI allows non-invasive visualization of the topography of distinct areas in visual cortex (Engel et al., 1994; Sereno et al., 1995; DeYoe et al., 1996; Wandell et al, 2005). These experiments generally present spatially and temporally periodic stimuli designed to induce periodic activity at a known temporal frequency in the visual cortex. Usually expanding or contracting rings are used for for eccentricity mapping, while a rotating wedge is used for polar angle mapping. The neural response to these periodic stimuli creates a “traveling wave” of activity moving across the cortical surface: as the location of the stimulus varies on the retina, so too does the location of peak neural activity in the visual cortex. The phase (lag) of a response relative to location of the stimulus at a given time therefore encodes the position of an active voxel (Engel et al., 1994; Sereno et al., 1995; DeYoe et al., 1996). The ultimate aim of retinotopic mapping studies is to reveal the topographic correspondence between points on the retina and points in visual cortex.

Retinotopic mapping by fMRI has led to major advances in knowledge of the functional organization of human visual cortex in the past 15 years; a recent review counted up to 16 distinct visual areas that have been mapped using this technique (Wandell et al., 2007). Of these, most investigators generally agree upon the location and topographic organization of early visual areas V1, V2, V3, V3A, and hV4 (Wandell et al., 2005; Wandell et al., 2007). The topographic structure of higher visual areas along the dorsal, lateral, and ventral cortical surfaces has been a focus of much recent work (Wandell et al., 2005; Wandell et al., 2007; Swisher et al., 2007; Hansen et al., 2007; Hoffman et al., 2009).

However, later visual areas tend to be considerably smaller than early visual areas both in physical size and in BOLD response magnitude (Hansen et al., 2004; Hoffman et al., 2009). Thus studies of the topography of the higher visual areas may benefit greatly from higher signal-to-noise ratios and higher spatial resolutions available at field strengths of 7T and above (Hansen et al., 2004; Hoffman et al., 2009).

To date, most retinotopic mapping studies have been conducted at 3T or 1.5T. However, one recent retinotopy study compares performance of various voxel sizes at 3T and 7T (Hoffman et al., 2009). The results suggest a number of benefits for retinotopic mapping at 7T, and one significant drawback.

One potential benefit to high field retinotopy is increased sensitivity, allowing high resolution mapping with voxel volumes on the order of $1mm^3$. In addition to the obvious benefit of producing more detailed retinotopic maps (Ress et al., 2007; Schira et al., 2007; Smith et al., 2001), using smaller voxels also reduces partial volume effects and the relative contributions of physiological noise (Kruger and Glover et al., 2001; Bodurka et al., 2006; Hoffman et al., 2009; Triantafyllou et al., 2006). A major limitation of functional imaging studies at 7T is off-resonance effects due to magnetic field inhomogeneities, including geometric image distortion, T_2^*-related blurring, and signal loss. At high field, large inhomogeneities cause local spins to dephase more quickly, worsening off-resonance effects and producing artifacts in single-shot 2D-EPI images.

While distortion and blurring are problems for all functional imaging, they can be particularly troublesome for retinotopic mapping. Results of these studies

are commonly rendered on inflated or flattened reconstructions of the cortical surface and rely on accurate alignment between functional images and anatomical data. Distortion of the functional images makes registration difficult, potentially leading to topographic misrepresentation in the surface maps. In light of this high sensitivity to off-resonance effects, we chose the high resolution retinotopic mapping paradigm as a platform to test the performance of different pulse sequences.

As discussed in earlier chapters, alternate approaches that maintain the high temporal resolution and BOLD sensitivity necessary for fMRI, but show decreased sensitivity to distortion and other bulk off-resonance effects, include three-dimensional, multi-shot imaging sequences such as multi-shot 3D-FFE and 3D-PRESTO (Liu et al., 1993; van Gelderen et al., 1995; Golay et al., 2000).

Given the SNR and BOLD contrast benefits of increasing B_0, the technical issues facing single-shot 2D-EPI for high field fMRI, and the inherent benefits of 3D imaging sequences for fMRI, we consider the fMRI performance of single-shot multi-slice 2D-EPI, 3D-FFE, and 3D-PRESTO at five resolutions (1 x 1 x 1mm^3, 1.12 x 1.12 x 1.12mm^3, 1.67 x 1.67 x 1.67mm^3, 2 x 2 x 2mm^3, and 3 x 3 x 3mm^3) in a polar angle retinotopic mapping experiment at 7T.

2. Theory

2.1. Signal to Noise

3D-FFE and 3D-PRESTO were chosen as potential alternatives to 2D-EPI based on theoretical signal-to-noise (SNR) and SNR efficiency calculations for

realistic scan parameters. These are given in Table 5.1 for each of five isotropic resolutions (1 x 1 x 1mm^3, 1.12 x 1.12 x 1.12mm^3, 1.67 x 1.67 x 1.67mm^3, 2 x 2 x 2mm^3, and 3 x 3 x 3mm^3).

As seen in chapter II, the signal in gradient-echo sequences such as 2D-EPI and 3D-FFE obeys[19]:

$$S_{GE} = M_0 \cdot \sin\theta \cdot \frac{1 - e^{\frac{-TR}{T_1}}}{1 - \cos\theta \cdot e^{\frac{-TR}{T_1}}} \cdot e^{\frac{-TE}{T_2^*}} \tag{5.1}$$

In 3D-PRESTO, the *n*-TR echo-shifting mechanic introduces two modifications to the gradient-echo signal behavior:

$$S_{ES-GE} = S_{GE} \cdot \cos^{2 \cdot n}\left(\frac{\theta}{2}\right) \cdot e^{\frac{-nTR}{T_2^*}} \tag{5.2}$$

Where the cosine term represents destructive interference from RF pulses occurring between excitation and collection of a shifted gradient echo, and the exponential term represents enhanced T_2^* weighting due to the shifted echo defined by: $TE_{eff} = TE_{nominal} + n \cdot TR$ (Denolin and Metens, 2004).

Likewise in chapter II we provided expressions for the signal-to-noise ratio for 2D-EPI, 3D-FFE, and 3D-PRESTO (neglecting increased noise contributions from parallel imaging):

[19] $T_1 \approx$ 1900 ms, $T_2^* \approx$ 22 ms for grey matter at 7T (Wright et al,. 2008).

$$SNR_{EPI} = S_{GE} \cdot \Delta_x \cdot \Delta_y \cdot \Delta_z \cdot \sqrt{\left(\frac{N_y}{BW_{read}}\right)} \tag{5.3a}$$

$$SNR_{3DFFE} = S_{GE} \cdot \Delta_x \cdot \Delta_y \cdot \Delta_z \cdot \sqrt{\left(\frac{N_y \cdot N_z}{BW_{read}}\right)} \tag{5.3b}$$

$$SNR_{PRESTO} = S_{ES-GE} \cdot \Delta_x \cdot \Delta_y \cdot \Delta_z \cdot \sqrt{\left(\frac{N_y \cdot N_z}{BW_{read}}\right)} \tag{5.3c}$$

3D acquisitions enjoy an increased signal-to-noise ratio of $\sqrt{N_z}$ (the square root of the number of slices or partitions), compared to equivalent 2D scans when all else is equal. In actual fMRI experiments, the theoretical SNR benefit of 3D acquisitions is often offset by reduced signal due to the shorter TRs and smaller flip angles required to maintain the temporal resolution necessary for fMRI in the 3D scans.

Previous chapters have also shown that Sensitivity Encoding is an effective means of reducing scan time and magnetic susceptibility effects in both 2D and 3D acquisitions at a cost to SNR and TSNR that depends on the total degree of acceleration, R*,* and the local geometry factor *g*. Here we apply the sequences developed in chapter IV, which were constrained to have isotropic voxel dimensions, high TSNR, geometry factors < 2 throughout the volume, and equal coverage between 2D-EPI and the corresponding 3D sequence at each resolution. Since preliminary experiments in chapter IV showed that even slight through-plane acceleration applied to thin slabs can lead to undesirably high geometry factors, we did not apply through-plane acceleration in this experiment.

Figures 5.1a-b show theoretical SNR_{EPI}, SNR_{3DFFE}, and SNR_{PRESTO} as a function of TR at five resolutions (1 x 1 x 1mm^3, 1.12 x 1.12 x 1.12mm^3, 1.67 x 1.67 x 1.67mm^3, 2 x 2 x 2mm^3, and 3 x 3 x 3mm^3) for the scan parameters shown in Table 5.1. Figures 5.2a-b show expected SNR_{EPI}, SNR_{3DFFE}, and SNR_{PRESTO} values using the parameters in Table 5.1. We expect 3D-FFE to show 44%, 32%, and 15% larger signal-to-noise ratios than 2D-EPI at 1 x 1 x 1mm^3, 1.12 x 1.12 x 1.12mm^3, and 1.67 x 1.67 x 1.67mm^3, while we predict 22% and 13% higher SNR values for 2D-EPI than 3D-PRESTO at 2 x 2 x 2mm^3, and 3 x 3 x 3mm^3, respectively.

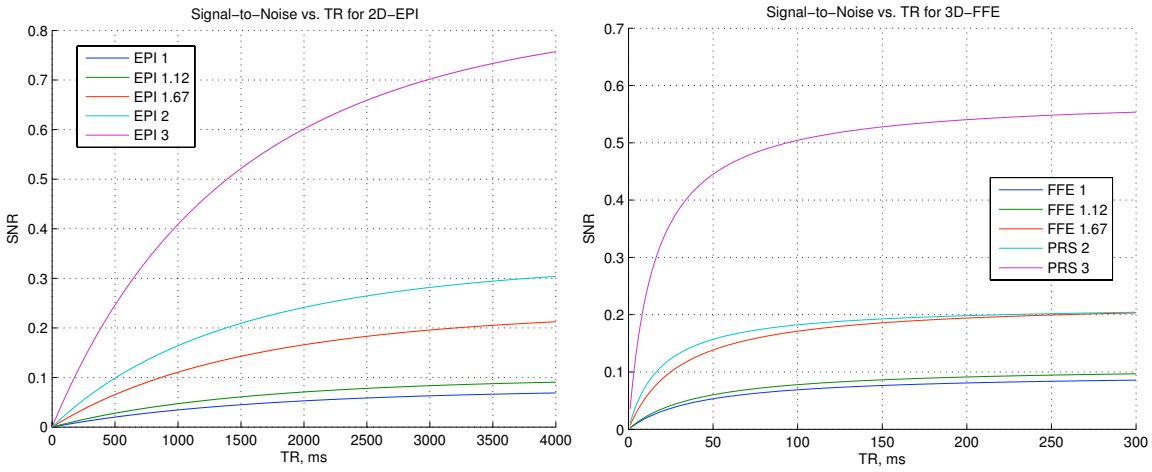

Figure 5.1: Theoretical (a) SNR_{EPI} and (b) SNR_{3DFFE} and SNR_{PRESTO} as a function of TR at five resolutions for the parameters given in Table 5.1.

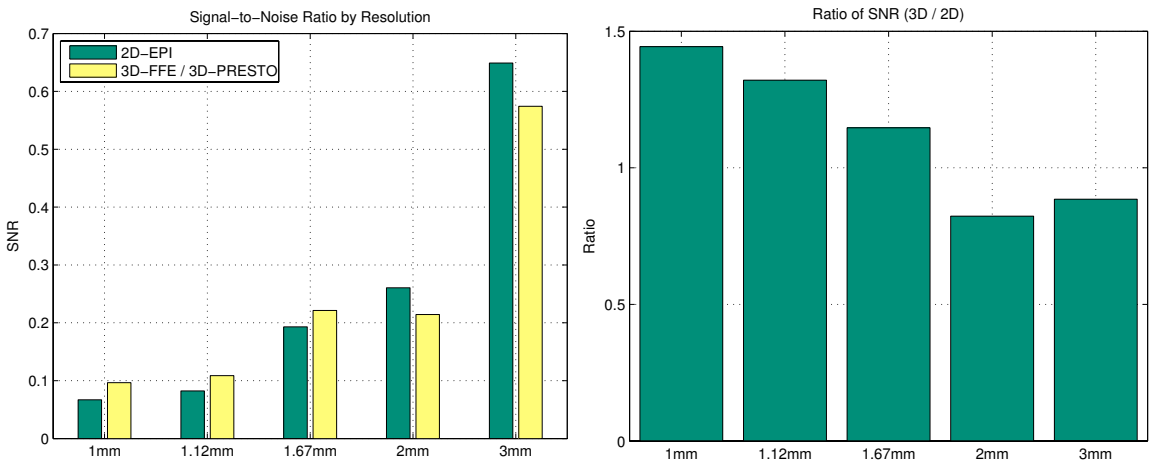

Figure 5.2: (a) Theoretical SNR_{EPI}, SNR_{3DFFE}, and SNR_{PRESTO} given the parameters in Table 5.1 at each resolution. (b) Theoretical ratio of SNR for the 3D scans to that of the corresponding 2D-EPI at each resolution for the parameters shown in Table 5.1.

2.2. Efficiency

Scan efficiency (η) is defined as signal-to-noise per unit time:

$$\eta = \frac{SNR}{\sqrt{T_{dyn}}} \tag{5.4}$$

Where *SNR* is the appropriate expression for signal-to-noise from Eqs. 5.3a-c, and T_{dyn} is the time to acquire the full data volume (dynamic scan time). Figure 5.3 shows the theoretical behavior of η_{EPI}, η_{3DFFE}, and η_{PRESTO} as a function of TR at five resolutions (1 x 1 x 1mm^3, 1.12 x 1.12 x 1.12mm^3, 1.67 x 1.67 x 1.67mm^3, 2 x 2 x 2mm^3, and 3 x 3 x 3mm^3) for the parameters in Table 5.1. Figure 5.4 shows η_{EPI}, η_{3DFFE}, and η_{PRESTO} using these parameters. Based on these values, we expect the 3D scans to be 25%, 12%, 15%, 4%, and 25% more efficient than 2D-EPI at 1 x 1 x 1mm^3, 1.12 x 1.12 x 1.12mm^3, 1.67 x

1.67 x 1.67mm^3, 2 x 2 x 2mm^3, and 3 x 3 x 3mm^3, respectively.

As seen with signal-to-noise in Figure 3, 3D-FFE theoretically outperforms 2D-EPI in terms of signal-to-noise efficiency at all resolutions, if only by a small margin. Meanwhile, 3D-PRESTO promises higher efficiency than 2D-EPI at 2 x 2 x 2mm^3 and 3 x 3 x 3mm^3, even though 3D-PRESTO has lower SNR than 2D-EPI at these resolutions as seen in Fig. 3a. The increase in efficiency comes from the time-savings (shorter T_{dyn}) related to the echo-shifted acquisition.

2.3. Off-Resonance Effects

As shown in chapter II, the amount off-resonance effects expected to occur in a given imaging direction is proportional to the data sampling bandwidth in that direction. In 2D-EPI, the phase encoding bandwidth is low, and therefore off-resonance effects such as distortion and blurring are severe.

In our experiments, the bandwidth in the frequency encoding direction was closely matched for both the 2D-EPI scan and the corresponding 3D scan at a given resolution (see Table 5.1). Thus we expected to see similar (and generally negligible) off-resonance effects in the frequency encoding direction. However, because the echo trains in the multi-shot 3D sequences are shorter than in 2D-EPI, the bandwidth in the phase encoding direction of the 3D scans is also higher, leading to reduced off-resonance effects in these 3D sequences.

Figure 5.5a shows the phase encoding bandwidth of each of our sequences at each resolution, while Figure 5.5b shows the ratio of phase encoding bandwidth in each 3D acquisition to that of its 2D-EPI counterpart.

Phase encoding bandwidth is 3.4, 3.0, and 2.5 times higher in 3D-FFE than in 2D-EPI at 1 x 1 x 1mm^3, 1.12 x 1.12 x 1.12mm^3, and 1.67 x 1.67 x 1.67mm^3, respectively, and 2.1 and 1.8 times higher in 3D-PRESTO than in 2D-EPI at 2 x 2 x 2mm^3 and 3 x 3 x 3mm^3, respectively. Therefore we expect distortion and blurring to be about 2-3 times less in our 3D data for a given resolution than in the corresponding 2D-EPI scan.

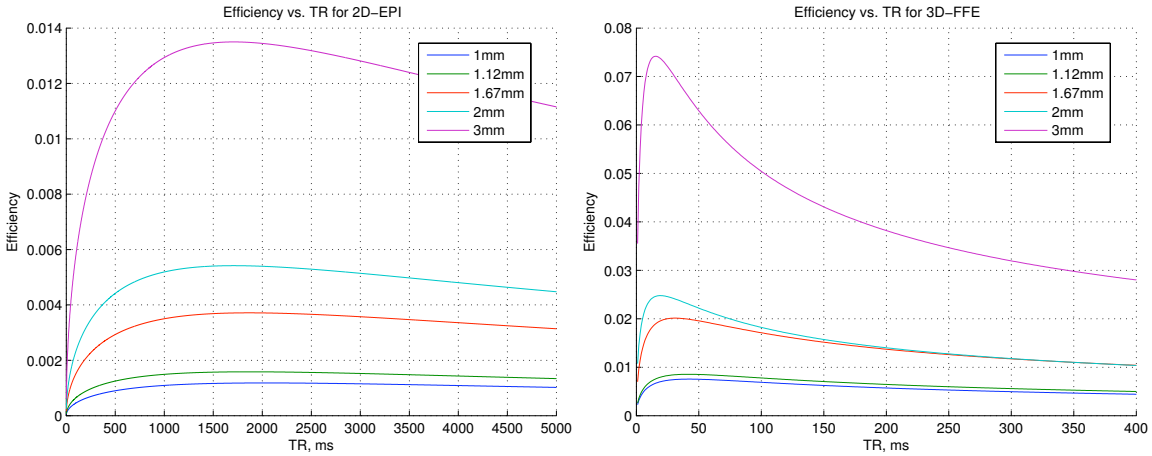

Figure 5.3: Theoretical (a) η_{EPI} and (b) η_{3DFFE} and η_{PRESTO} given the parameters in Table 5.1. The 2D-EPI scans achieve maximum efficiency around TR = 1700 ms at all resolutions, while the 3D scans peak at short TRs (42 ms, 42 ms, 31 ms, 19 ms, and 15 ms for the 1 x 1 x 1mm^3, 1.12 x 1.12 x 1.12mm^3, 1.67 x 1.67 x 1.67mm^3, 2 x 2 x 2mm^3, and 3 x 3 x 3mm^3 resolutions, respectively).

3. Methods

3.1. Subjects

Four healthy adult subjects (2 male and 2 female) were recruited from the Vanderbilt University community. Each subject provided written informed consent and was treated in a manner consistent with a protocol approved by the IRB of Vanderbilt University. Each volunteer was an experienced MRI subject who was

familiar with the retinotopic mapping stimulus. Subjects' heads were secured with padding and a bite bar to minimize movement during scanning. Scan order was randomized both within and across sessions for each subject to prevent systematic errors or habituation.

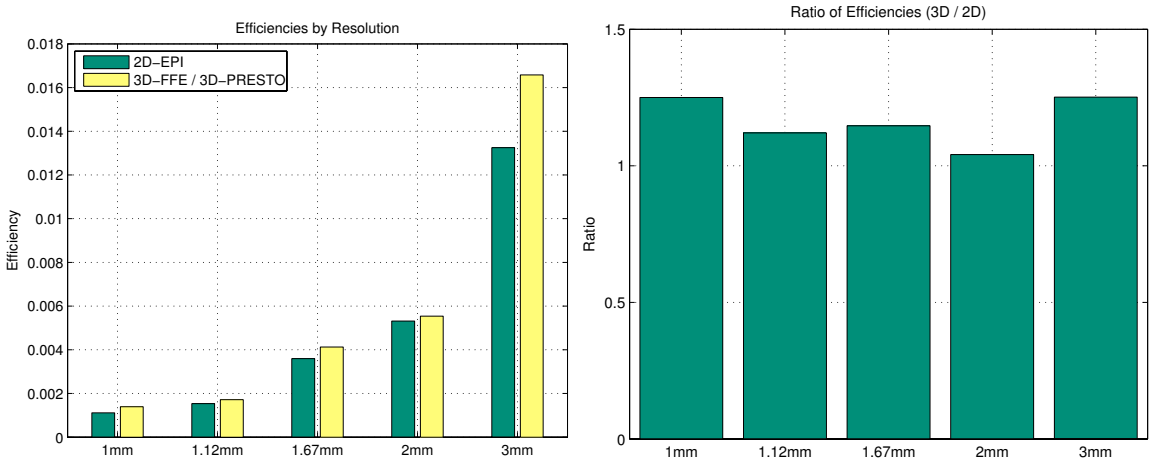

Figure 5.4: Theoretical (a) η_{EPI}, η_{3DFFE}, and η_{PRESTO} and (b) ratio of η for each 3D scan to the corresponding 2D-EPI scan at each resolution given the parameters in Table 5.1.

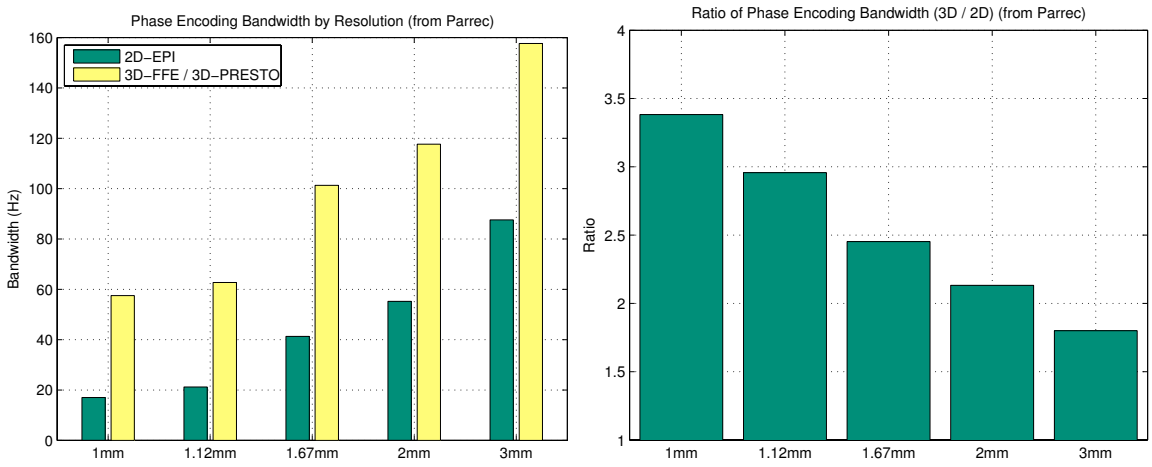

Figure 5.5: (a) Measured phase encoding bandwidth (Hz) and (b) ratio of phase encoding bandwidth (3D/2D) for 2D-EPI, 3D-FFE, and 3D-PRESTO at each resolution given the parameters in Table 5.1.

Each subject participated in two one-hour scan sessions. During each session, up to four functional data sets were acquired for each acquisition type (2D or 3D) at two of our four resolutions (2D-EPI and 3D-FFE at 1.12 x 1.12 x 1.12mm^3 and 1.67 x 1.67 x 1.67mm^3, or 2D-EPI and 3D-PRESTO at 2 x 2 x 2mm^3 and 3 x 3 x 3mm^3). We also acquired three repetitions of 3D-FFE and 2D-EPI acquisitions at 1 x 1 x 1mm^3 in one additional subject. As expected from the preliminary studies in chapter IV, geometry factors and TSNR were found to be near our limits in the 1 x 1 x 1mm^3 data. Therefore we did not acquire a complete set of retinotopic mapping data at 1 x 1 x 1mm^3.

3.2. Stimulus

Visual stimuli were presented with an MR compatible projector illuminating a screen mounted inside the bore of the 7T scanner. Subjects viewed the screen through a mirror custom fitted to the head-coil and angled at approximately 45 degrees. Subjects were presented with a black and white flashing checkerboard wedge which occupied 108 angular degrees of the visual field. 108 angular degrees was chosen as a compromise between a large stimulus optimized for mapping of smaller receptive fields such as those found in V1, V2, and V3 (~180 angular degrees), versus smaller stimuli optimized for mapping of larger receptive fields such as those found in, for example, V3A and hV4 (Dumoulin and Wandell 2008). Checkerboard luminance alternated between “light” and “dark” checks which reversed at 8Hz. The check radius scaled logarithmically in approximation of the cortical magnification function (Horton and Hoyt, 1991). The

wedge rotated counterclockwise with a period of 36 seconds (8 cycles per 288 second run).

At random intervals throughout the functional run, a random segment of the wedge would become dim for approximately one second. Figure 5.6 shows our stimulus during a dimming event. Subjects were asked to focus on a small central fixation point (~8 arc-minutes) and attend to the wedge in their peripheral vision. Attending to the periphery has been suggested to enhance activation signal in experienced subjects compared to directly attending to the wedge stimulus (Szczepanski et al., 2008; Silver et al., 2009). Subjects were instructed to respond to dimming events with a button press in order to maintain vigilance throughout the functional run.

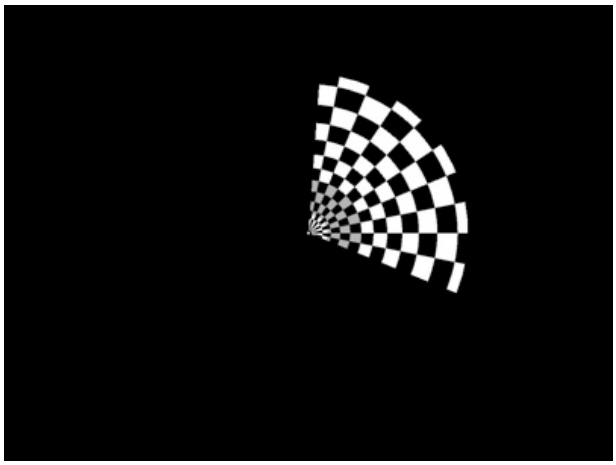

Figure 5.6: Retinotopic mapping stimulus. The checkerboard wedge occupied 108 degrees of the visual field, rotated counter-clockwise, and reversed light and dark patches at 8Hz. At random intervals throughout the scan, a random section of the checkerboard wedge would become dim (see center section here) for approximately one second.

3.3. Scan Parameters

Subjects were scanned on a Philips Achieva 7T scanner with a 16 channel SENSE receive-only head coil and an outer quadrature transmit coil. 3D-FFE and 2D-EPI data were acquired at 1x 1 x 1mm^3, 1.12 x 1.12 x 1.12mm^3 and 1.67 x 1.67 x 1.67mm^3, while 3D-PRESTO and 2D-EPI data were obtained at 2 x 2 x 2mm^3 and 3 x 3 x 3mm^3. Slices were oriented approximately perpendicular to the calcarine sulcus and positioned to fully cover the occipital pole and as many high visual areas as possible for each resolution. Representative slice geometries are shown in Figure 5.7.

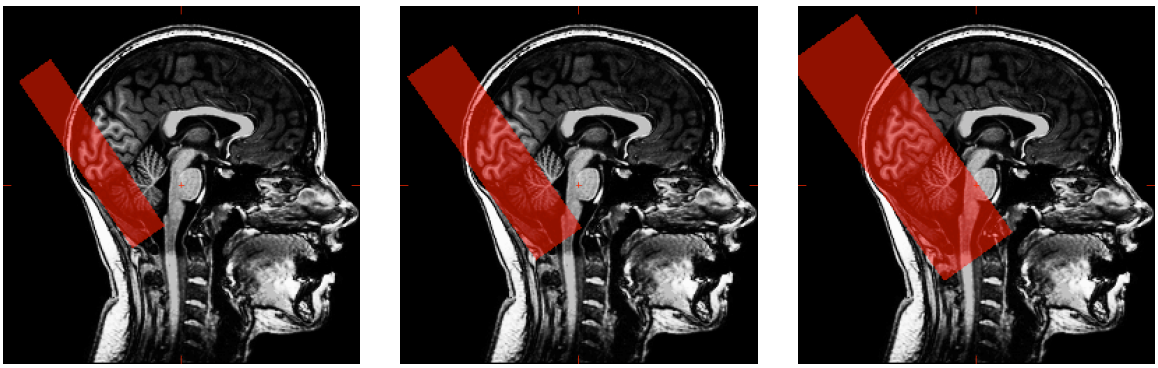

Figure 5.7: Representative Slice Geometries for the a) 1.12 x 1.12 x 1.12mm^3, b) 1.67 x 1.67 x 1.67mm^3 and 2 x 2 x 2mm^3, and c) 3 x 3 x 3mm^3 scans acquired in this study. Slices were positioned perpendicular to the calcarine sulcus and covered the occipital pole and as many higher visual areas as possible. Identical slice geometries were used for 2D-EPI and the corresponding 3D sequence at a given resolution.

As described in chapter IV, scan parameters such as SENSE acceleration factor and TR were chosen on a scan-by-scan basis in order to maintain isotropic voxel dimensions at the resolutions specified above, equal slice coverage between competing 2D and 3D acquisitions, and geometry factors less than 2 at

each resolution. TR was chosen to be as short as possible in each study. Constraining our choice of SENSE factors based on the *g* they produced determined our minimum TR for a given FOV and resolution, which in turn determined the dynamic scan time and the number of images that could be acquired within our fixed scan time of 288 seconds per run (a typical scan time for functional experiments). The flip angle was the Ernst angle for each TR. All scans had TE = 22 ms except for the 2 x 2 x 2mm^3 3D-PRESTO scan, which had a minimum TR of 19ms, which resulted in a shifted echo time of TE = 26ms. See Table 5.1 for detailed acquisition parameters.

3.4. Preprocessing

Functional data were motion corrected using FSL's "mcflirt" algorithm with six degrees of freedom (Jenkinson et al., 2002). Functional images were manually aligned by an experienced operator to T1-weighted 3D-TFE anatomical images that had previously been acquired at 3T. After the functional scans were aligned to the 3D structural images, the Freesurfer reconstruction stream was used to identify the gray/white matter borders and the pial surface. Functional voxels falling between the gray/white matter border and the pial surface were labeled as gray matter. This provided a "gray matter mask" volume with the same geometry as the functional volumes.

A second mask of the V1 visual area was obtained for each subject from previously obtained 3T retinotopy data. Each V1 mask volume was then intersected with the corresponding gray matter mask and applied to the

functional volume for each subject. The result provided coordinates for gray matter voxels which were also in V1, and therefore a simple means of accessing relevant activation information for each subject.

No smoothing was applied to the functional data at any stage of the analysis, and no distortion corrections were applied to the functional data presented here so we could compare the effects of image distortion on retinotopic map quality between sequences.

3.5. Retinotopy Analysis

Phase-encoded retinotopic mapping (Engel et al., 1994; Sereno et al., 1995; DeYoe et al., 1996) is based on the use of a periodic stimulus to induce neural activity at the same frequency in visually responsive voxels. Two components of the response are of interest: the amplitude response at the stimulus frequency relative to the background spectrum (noise) determines the significance of the modulation, whereas the phase of this response encodes the position of the voxel receptive field (Swisher et al., 2007).

Statistical maps were calculated using a fast Fourier transform on the time course of each voxel. The ratio of the signal power at the fundamental stimulus frequency and average power at all frequencies was computed, excluding the first and second harmonics and very low frequencies (1–3 cycles per scan). Under the assumption of white, temporally uncorrelated noise, the power at each frequency is an independent, identically distributed χ^2 random variable. The

resulting ratio of signal power is F-distributed; therefore activation significance was measured with an F-statistic (Tootell et al., 1998; Konen and Kastner, 2008).

The square root of the F-statistic is proportional to the ratio of the amplitude of modulation at the stimulus frequency (1/36 Hz) over the average amplitude of modulation at all other (presumably noise) frequencies. The median value of the square-root of the F-statistics therefore provides an estimate of the functional SNR in a pool of activated voxels (Warnking et al., 2002). We calculated the F-statistics and functional SNR within V1 for each subject at each resolution. We then calculated the mean and standard error of this median functional SNR across all subjects for each resolution.

3.6. Data Visualization on the Cortical Surface

The cortical surface of each hemisphere of each subject was reconstructed as a triangular mesh from the subject's anatomically segmented high-resolution anatomical volume (Dale et al., 1999; Fischl et al., 1999). Both the gray/white matter and pial surfaces were segmented using Freesurfer. The functional statistic volumes were projected by nearest neighbor search onto the vertices of an interpolated mesh located halfway between the gray/white and pial surfaces. The cortical mesh was then computationally inflated. The resulting projected statistical image was then visualized similarly to previous reports (Sereno et al., 1995). Surface vertices which exceed a $p < 0.01$ significance threshold were rendered in a color indicating the phase of the signal estimate at that point.

Table 5.1. Acquisition parameters for retinotopic mapping sequences.

Res. (mm^3)	Coronal									
	1 x 1 x 1		1.12 x 1.12 x 1.12		1.67 x 1.67 x 1.67		2 x 2 x 2		3 x 3 x 3	
	2D-EPI	3D-FFE	2D-EPI	3D-FFE	2D-EPI	3D-FFE	2D-EPI	3D-PRS	2D-EPI	3D-PRS
FOV	144x144x30		144x144x28		160x160x40		160x160x40		192x192x60	
TE (ms)	22							(6) 26	22	(7) 22
TR (ms)	3600	39.47	2880	41.66	2880	31	2400	19.23	2400	15.38
T_{Dyn} (ms)	3600	4500	2880	4000	2880	2880	2400	1500	2400	1200
Slices	30	30	25	25	24	24	20	20	20	20
R_{RL}	2.4	2.7	2.4	2.6	2.7	2.6	2.7	2.2	2.6	1.8
BW_{phase}	17	57.5	21.2	62.7	41.3	101.3	55.2	114.1	79.7	144.7
BW_{freq}	1406	1398	1580	1571	2333	2199	2793	2610	4163	4103
ETL	63	17	55	17	37	13	31	13	27	13
Dyns	80	64	100	72	100	100	120	192	120	240
Flip	80	20	80	20	80	10	80	10	80	10

The color map was defined so the contralateral horizontal meridian was rendered in blue, the upper vertical meridian was rendered in red, the lower vertical meridian was rendered in green, and the ipsilateral horizontal meridian was rendered in yellow. For display purposes, the color map was compressed slightly to overrepresent the contralateral visual field, so as to approximately match the distribution of response phase within the early retinotopic areas (Swisher et al., 2007). Surface vertices which did not exceed $p < 0.01$ were rendered in dark or light gray to reveal cortical sulci and gyri. Figure 5.8 shows visual areas labeled on an example retinotopic map.

3.7. SPM Analysis

Statistical Parametric Mapping (SPM5; Wellcome Department of Cognitive Neurology, London, UK) was used to calculate statistical activation maps for all protocols with threshold of $p < 0.01$ and a minimum cluster size of 3 voxels. Sine and cosine waves with the same period as our stimulus (36s) were entered into the SPM general linear model as regressors in an F-contrast. Low frequency fluctuations were were removed using the SPM default high-pass filter which removes frequency drifts with a period longer than 128 seconds.

A MATLAB (The Mathworks, Inc., Natick, MA) script was used to quantify the distributions of temporal signal to noise ratio (TSNR) and F-statistics in each scan from the output of the SPM GLM. TSNR was calculated for each voxel as the mean signal divided by the square root of residual variance after removal of

task-related variance. Functional signal-to-noise ratio was calculated as the median value of the square root of the F-statistics for a given pool of voxels.

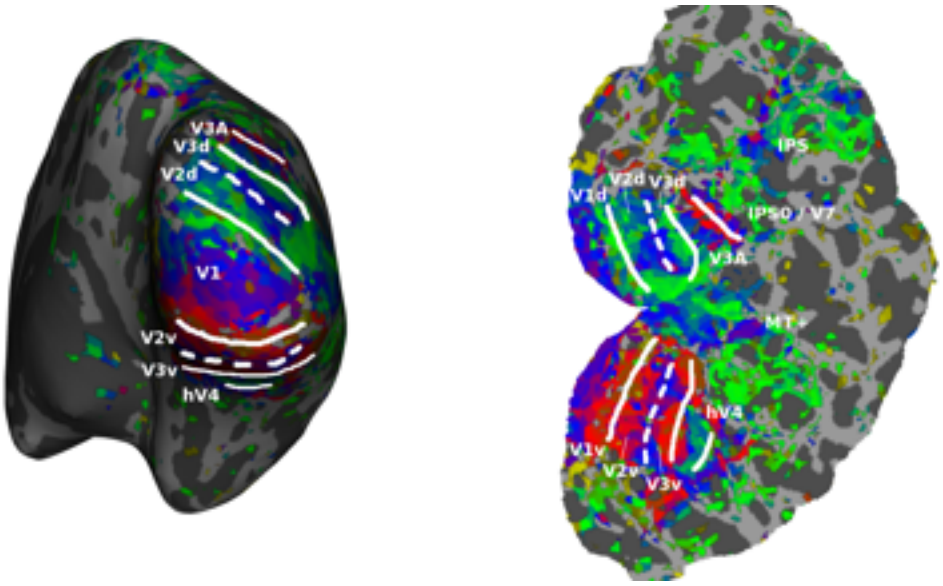

Figure 5.8: Example retinotopic map with visual areas labeled. The color map for this and all similar images was defined so that the representation of the contralateral horizontal meridian was rendered in blue, the upper vertical meridian was rendered in red, the lower vertical meridian was rendered in green, and the ipsilateral horizontal meridian was rendered in yellow.

4. Results

We tested the performance of 2D-EPI, 3D-FFE, and 3D-PRESTO at four resolutions (1.12 x 1.12 x 1.12mm^3, 1.67 x 1.67 x 1.67mm^3, 2 x 2 x 2mm^3, and 3 x 3 x 3mm^3) in a retinotopic mapping functional fMRI experiment at 7T. We also acquired 2D-EPI and 3D-FFE data at 1mm^3 for one additional subject but did not acquire full retinotopy data at this resolution because TSNR and geometry factors were generally poor. Robust brain activity was detected at all resolutions in all sequences, and all retinotopic maps were in general agreement with

previous reports (Engel et al., 1994; Sereno et al., 1995; DeYoe et al., 1996; Wandell et al., 2005; Wandell et al., 2007; Hansen et al., 2007; Swisher et al., 2007; Hoffmann et al., 2009).

Figure 5.9 shows polar angle retinotopic maps of 2D-EPI and 3D-FFE data at 1.12 x 1.12 x 1.12mm^3 and 1.67 x 1.67 x 1.67mm^3 for one representative subject, while Figure 5.10 shows the same for 2D-EPI and 3D-PRESTO at 2 x 2 x 2mm^3 and 3 x 3 x 3mm^3. Defining the cortical visual fields according to Figure 5.8, our 1.12mm^3 retinotopic maps clearly show visual areas V1, V2, V3, and parts of V3A and hV4. Meanwhile the 1.67 x 1.67 x 1.67mm^3, 2 x 2 x 2mm^3 and 3 x 3 x 3mm^3 maps show all of V3A, hV4, LO1/2, and V7 (IPS0). As expected, map clarity increased with resolution for all sequences. Note the yellow blobs in the 2D-EPI images in Figures 5.9-5.10. According to our polar angle color map (inherited from Sereno et al., 1995), the yellow color corresponds to activation in the ipsilateral visual field that has been displaced due to image distortion. Yellow distortion artifacts are present to a lesser extent at the lower resolutions, but always more in 2D-EPI than in the corresponding 3D sequences. This is consistent with distortion predictions from the phase encoding bandwidth measurements in Figures 6a and 6b.

Figures 5.11 and 5.12 compare coronal activation maps in the primary visual cortex for one representative subject across sequences and resolutions. In each of these images, blue lines represent the cortical surface, while green lines represent the gray/white matter boundary. Maps are thresholded to show similar

amounts of activation at each resolution ($F > 5$ for 1.12 x 1.12 x 1.12mm^3, $F > 20$ for 1.67 x 1.67 x 1.67mm^3, $F > 60$ for 2 x 2 x 2mm^3 and 3 x 3 x 3mm^3).

The relationship between activation and underlying cortical anatomy is reasonably clear for both 2D-EPI and 3D-FFE at 1.12 x 1.12 x 1.12mm^3 and 1.67 x 1.67 x 1.67mm^3. These relationships become less clear at 2 x 2 x 2mm^3 and 3 x 3 x 3mm^3 as voxel volumes increase. In all cases, and especially at the higher resolutions, the 2D-EPI images show significant distortion of activated voxels both across gray/white matter boundaries (green lines) and outside the cortical surface (blue lines). By contrast, 3D-FFE and 3D-PRESTO show much less distortion.

At 1.12 x 1.12 x 1.12mm^3 and 1.67 x 1.67 x 1.67mm^3, The total number of activated voxels is significantly lower in 3D-FFE compared to 2D-EPI, but those voxels are more localized to specific cortical structures. At 2 x 2 x 2mm^3 and 3 x 3 x 3mm^3 3D-PRESTO images show more activation than their 2D-EPI counterparts.

Figure 5.13a compares the distribution of temporal signal to noise within the top ten percent of activated voxels across all subjects at all resolutions. Figure 5.13b compares the median values of TSNR in the same voxels. As expected based on the relationship between SNR and voxel volume, the temporal signal to noise ratio for each sequence increases as resolution decreases. All differences between resolutions for a given sequence are significant ($p < 0.01$), and all differences between sequences at a given resolution are significant ($p < 0.01$) with the exception of 1 x 1 x 1mm^3.

Theoretical SNR predictions in Figures 5.3a and 5.3b were 44%, 32%, and 15% higher in 3D-FFE than in 2D-EPI at 1 x 1 x 1mm^3, 1.12 x 1.12 x 1.12mm^3, and 1.67 x 1.67 x 1.67mm^3. We observe nearly identical TSNR for 3D-FFE and 2D-EPI in our single subject at 1 x 1 x 1mm^3, and 6% greater TSNR in 3D-FFE compared to 2D-EPI for all subjects at 1.12 x 1.12 x 1.12mm^3. At 1.67 x 1.67 x 1.67mm^3, however, the TSNR of 2D-EPI is 44% greater than that of 3D-FFE. Figures 3a and 3b also predict that 3D-PRESTO should have 22% and 13% less SNR than 2D-EPI at 2 x 2 x 2mm^3 and 3 x 3 x 3mm^3, respectively. Our observations agree with theory in that TSNR is lower in 3D-PRESTO than in 2D-EPI at those resolutions, but the differences (37% lower at 2 x 2 x 2mm^3 and 55% lower at 3 x 3 x 3mm^3) are larger than predicted. These differences are addressed in the discussion section.

Figure 5.14a compares the distribution of F-statistics within the top ten percent of activated voxels across all subjects at all resolutions. Figure 5.14b compares the median values of the square root of the F-statistics in the same voxels. As discussed in methods, the median of the square root of the F-statistics gives an estimate of functional SNR in the activated regions. As expected from the larger signal-to-noise ratio inherent to larger voxels, the median F-statistic tended to increase for both sequences as resolution decreased. All differences are significant ($p < 0.01$).

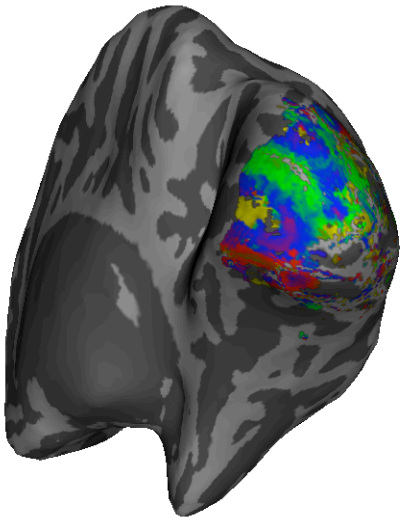

a) 2D-EPI 1.12 x 1.12 x 1.12 mm^3

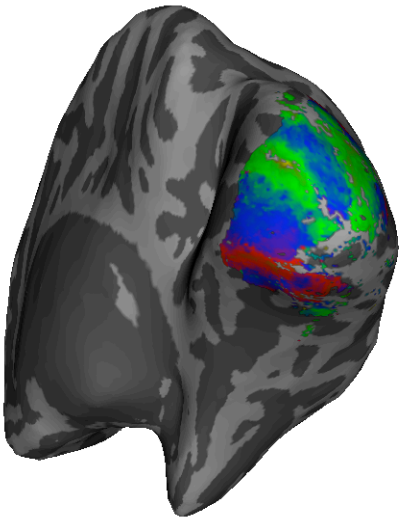

b) 3D-FFE 1.12 x 1.12 x 1.12mm^3

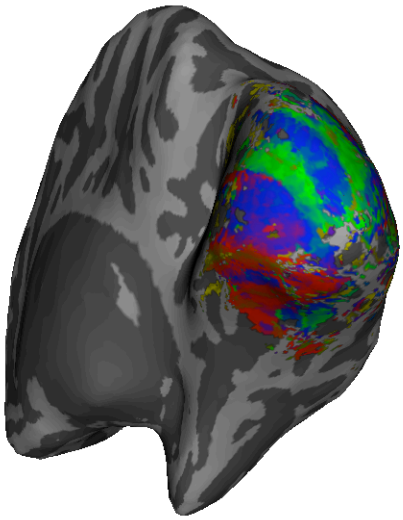

c) 2D-EPI 1.67 x 1.67 x 1.67mm^3

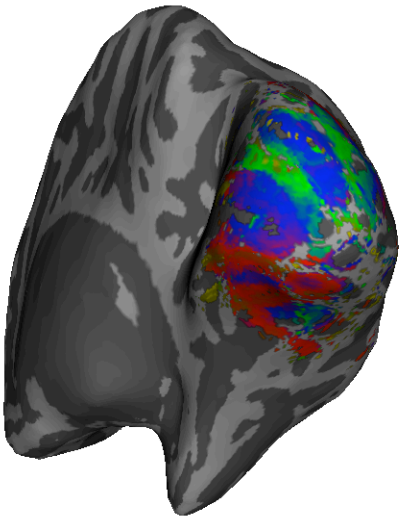

d) 3D-FFE 1.67 x 1.67 x 1.67mm^3

Figure 5.9: Retinotopic maps of a) 2D-EPI and b) 3D-FFE at 1.12 x 1.12 x 1.12mm^3 and c) 2D-EPI and d) 3D-FFE at 1.67 x 1.67 x1.67mm^3. At 1.12 x 1.12 x 1.12mm^3, the 3D-FFE map appears cleaner, more complete, and less distorted than the 2D-EPI map. Obvious yellow blobs on the 2D-EPI image indicates a large amount of activation distorted from the ipsilateral hemisphere onto these retinotopic maps.The 3D-FFE map appears free of this distortion. At 1.67 x 1.67 x 1.67mm^3, the 2D-EPI map appears slightly cleaner than 3D-FFE map.

2D-EPI showed 58%, 21%, and 43% higher median F-statistics compared to 3D-FFE at 1 x 1 x 1mm^3, 1.12 x 1.12 x 1.12mm^3, and 1.67 x 1.67 x 1.67mm^3, respectively[20]. Meanwhile, 3D-PRESTO shows 30% and 57% larger median F-statistics than 2D-EPI at 2 x 2 x 2mm^3 and 3 x 3 x 3mm^3. These differences are consistent in observation of both the distribution of F-statistics and in the median value of the square root of the F-statistics.

TSNR and F-statistics do not seem to be directly correlated except that they both increase as resolution decreases. For example, at 1.12 x 1.12 1.12mm^3 TSNR is significantly higher in 3D-FFE than in 2D-EPI, yet the F-statistics for 2D-EPI are significantly higher than for 3D-FFE. Because the voxels are quite small at this resolution and because TSNR is higher in 3D-FFE in this case, we do not expect that physiological noise dictates the F-statistic discrepancy in this case. These differences are further addressed in the discussion section.

5. Discussion

We have compared the performance of 3D-FFE and 3D-PRESTO to that of single-shot, multi-slice 2D-EPI for a polar angle retinotopic mapping study at four resolutions at 7T (1.12 x 1.12 x 1.12mm^3, 1.67 x 1.67 x 1.67mm^3, 2 x 2 x 2mm^3, 3 x 3 x 3mm^3). We find that 2D-EPI shows slightly higher functional sensitivity and comparable TSNR to 3D-FFE at 1.12 x 1.12 x 1.12mm^3, and 1.67 x 1.67 x 1.67mm^3, and that 3D-PRESTO shows significantly higher functional

[20] Note the 1 x 1 x 1mm^3 data are based on three repetitions of each function run in just one subject, and may not be as reliable as data for the other resolutions.

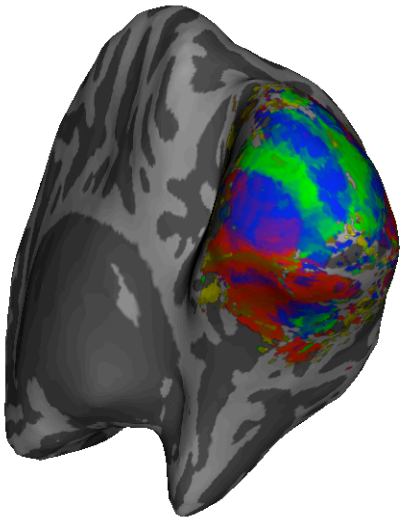

a) 2D-EPI 2 x 2 x 2mm^3

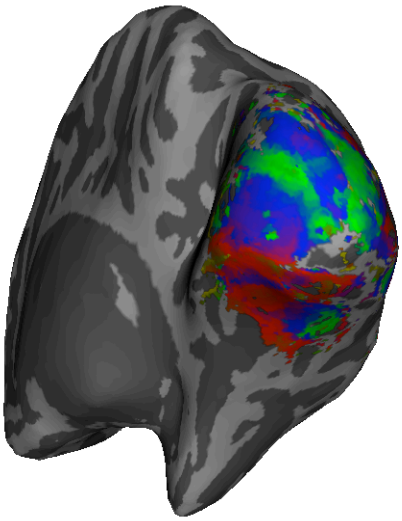

b) 3D-PRESTO 2 x 2 x 2mm^3

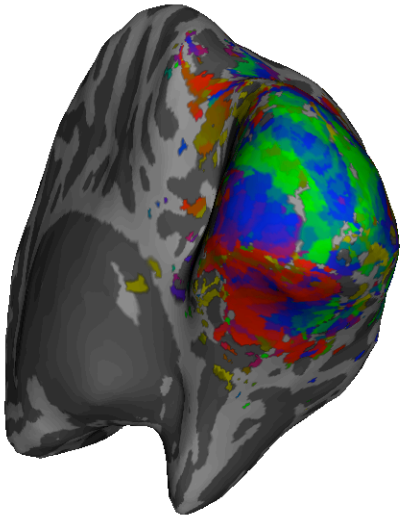

c) 2D-EPI 3 x 3 x 3mm^3

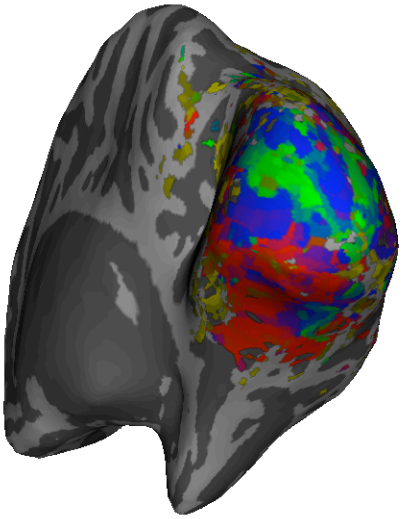

d) 3D-PRESTO 3 x 3 x 3mm^3

Figure 5.10: Retinotopic maps of a) 2D-EPI and b) 3D-PRESTO at 2 x 2 x 2mm^3 and c) 2D-EPI and d) 3D-PRESTO at 3 x 3 x 3mm^3. While the maps are qualitatively similar, the 3D-PRESTO map appears cleaner than 2D-EPI at both resolutions. Yellow blobs indicate activation distorted from the ipsilateral hemisphere. The 3D-PRESTO images appear relatively free of distortion.

sensitivity than 2D-EPI at 2 x 2 x 2mm^3 and 3 x 3 x 3mm^3 despite having lower TSNR because 3D-PRESTO has higher SNR efficiency. Activation and retinotopy maps from the 3D sequences consistently show less distortion than 2D-EPI, especially at higher resolutions.

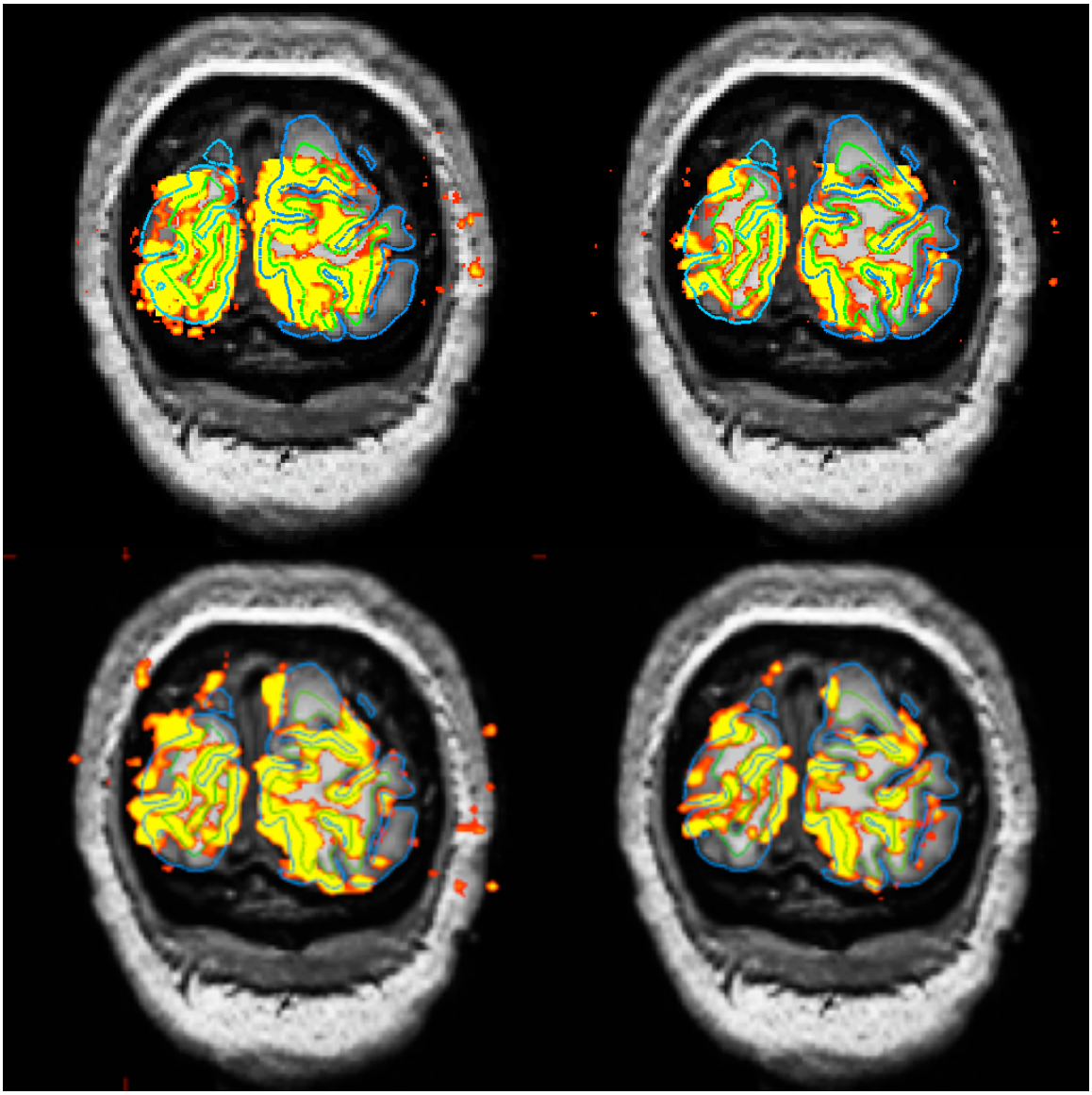

Figure 5.11: Activation maps of the primary visual cortex (V1) for 2D-EPI (left) and 3D-FFE (right) at 1.12 x 1.12 x 1.12mm^3 (top; $F > 5$) and 1.67 x 1.67 x 1.67mm^3 (bottom; $F > 20$). Blue lines represent the edges of the cortical surface, while green lines represent the gray/white matter boundary.

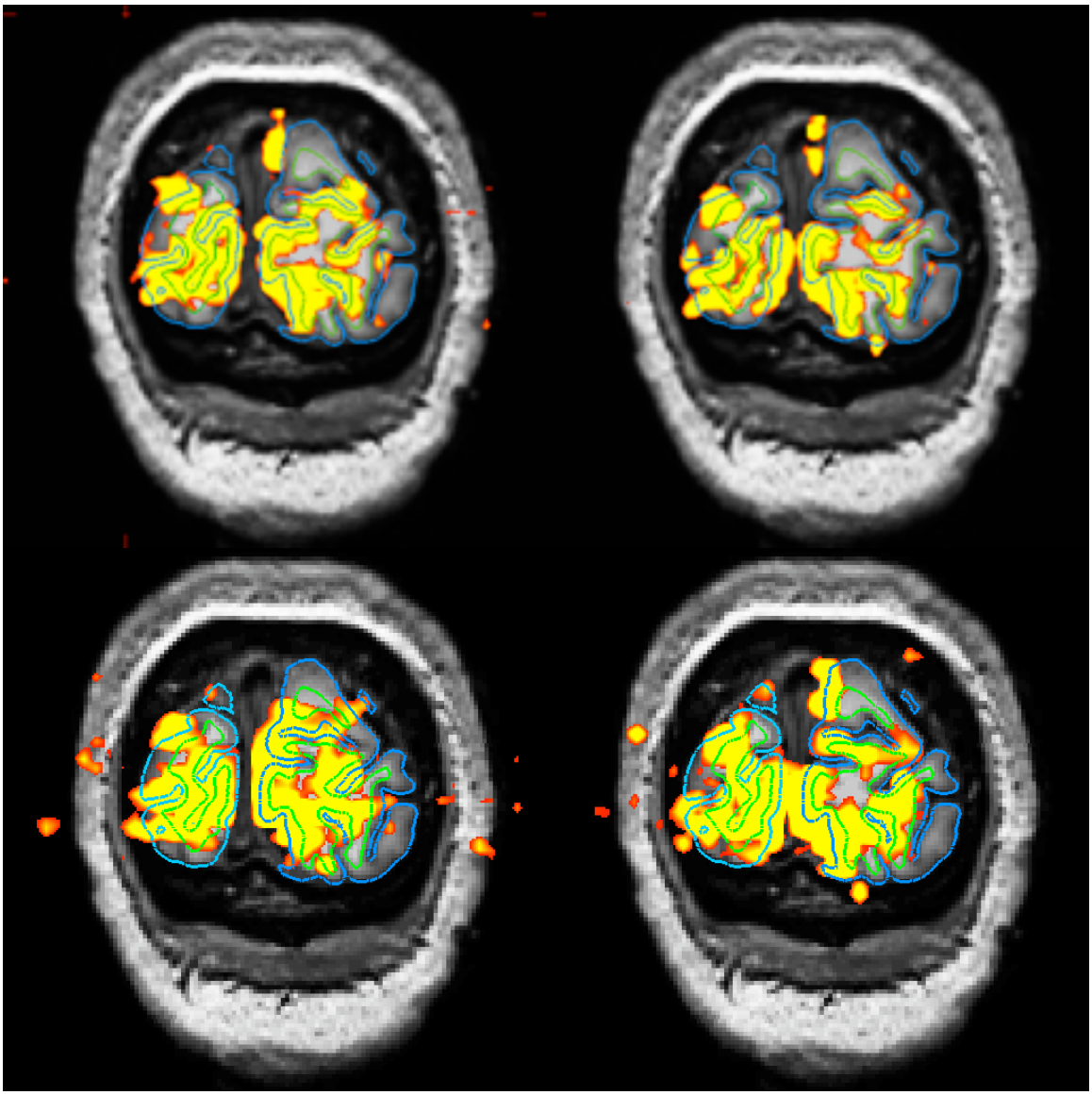

Figure 5.12: Activation maps (thresholded at F > 60) of the primary visual cortex (V1) for 2D-EPI (left) and 3D-PRESTO (right) at 2 x 2 x 2mm^3 (top) and 3 x 3 x 3mm^3 (bottom). Blue lines represent the edges of the cortical surface, while green lines represent the gray/white matter boundary.

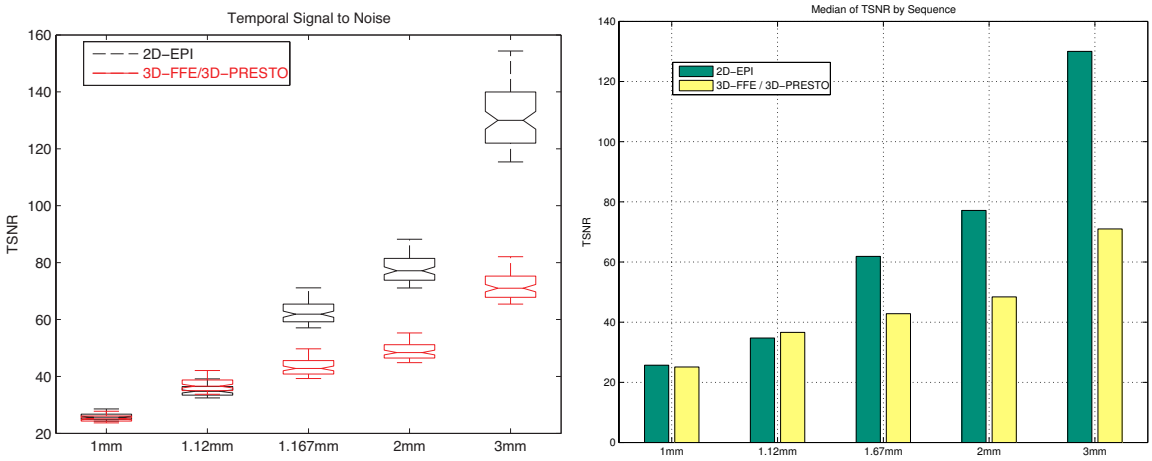

Figure 5.13: (a) Distribution of the top ten percent of TSNR values for 2D-EPI (black) and 3D-FFE/3D-PRESTO (red) across all subjects and resolutions. (b) Median of the top ten percent of TSNR values for for 2D-EPI (green), 3D-FFE (yellow - 1 x 1 x 1mm^3, 1.12 x 1.12 x 1.12mm^3, and 1.67 x 1.67 x 1.67mm^3), and 3D-PRESTO (yellow - 2 x 2 x 2mm^3, 3 x 3 x 3mm^3) across all subjects and resolutions.

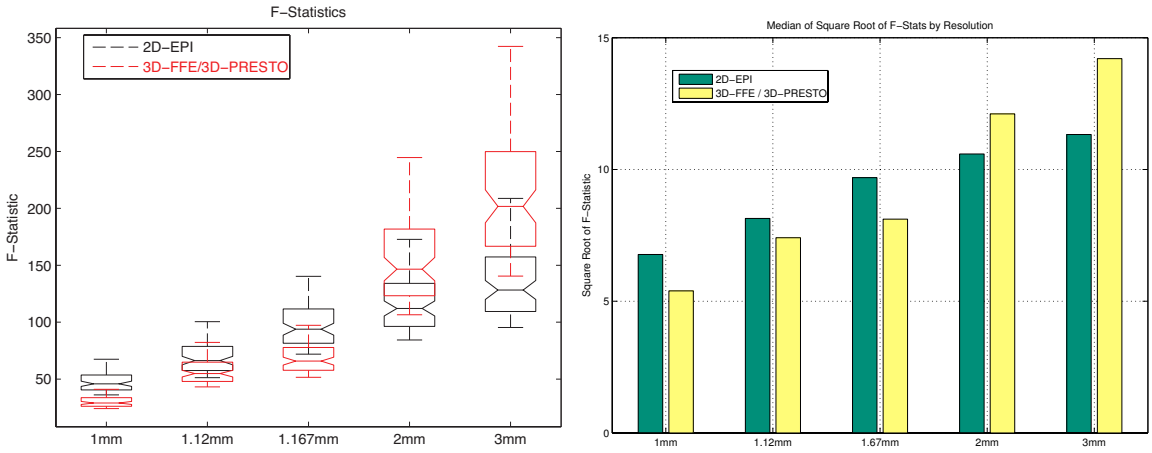

Figure 5.14: (a) Distribution of the top ten percent of F-Statistics for 2D-EPI (all resolutions - black), 3D-FFE/3D-PRESTO (red) across all subjects and resolutions. (b) Median value of the square-root of the top 10 percent of F-Statistics for 2D-EPI (green), 3D-FFE (yellow - 1 x 1 x 1mm^3, 1.12 x 1.12 x 1.12mm^3, and 1.67 x 1.67 x 1.67mm^3), and 3D-PRESTO (yellow - 2 x 2 x 2mm^3, 3 x 3 x 3mm^3) across all subjects and resolutions.

While total activated voxels in 3D-FFE are generally fewer compared to 2D-EPI at all resolutions, activity measured with 3D-FFE shows a closer correspondence to underlying cortical anatomy compared to 2D-EPI. This could be due to reduced blurring and distortion related to T2* effects as a result of shorter echo train lengths in the multi-shot sequences (Duong et al., 2003; Kim et al., 2004; Yacoub et al., 2005; Neggers et al., 2008; Lui et al., 1993; Ogawa et al., 1993). We expect this to be true for 3D-PRESTO as well because the additional gradients which perform the echo shifting also act as "crusher" gradients which destroy transverse magnetization in large blood vessels (Neggers et al., 2008; Liu et al., 1993).

Measured TSNR values for our 3D sequences tend to be below theoretical SNR predictions. However, theoretical SNR predictions do not account for temporal signal variation related to, for example, subject motion, scanner instability, or physiological noise. In this respect, theoretical SNR calculations represent an upper limit for TSNR but may predict TSNR poorly in realistic imaging scenarios. Because our 3D sequences are multi-shot, they are more susceptible to some temporal instabilities (such as motion and phase errors) than the single-shot 2D-EPI acquisition. At shown in chapter IV, physiological noise significant factor in limiting TSNR relative to SNR in both 2D and 3D sequences. Recently Goerke et al. (2008) have shown that physiological noise may in fact manifest differently in 2D-EPI and 3D-FFE-like sequences.

Despite lower TSNR compared to 2D-EPI, 3D-PRESTO showed higher F-statistics at 2 x 2 x 2mm^3 and 3 x 3 x 3mm^3. As suggested by efficiency

calculations and by Constable and Spencer (2001), statistical power to detect activation increases with the square root of the number of images collected in a functional run. Since we have fixed our acquisition time at 288 seconds, sequences with shorter TRs will acquire more images in a given functional run and thus have more statistical power. Thus the combination of higher SNR efficiency, short TRs, and more images acquired per run explain the higher F-statistics in 3D-PRESTO despite lower TSNR. This is consistent with other recent 3D-PRESTO data from Neggers et al. (2008).

As stated in Methods, our volunteers were experienced fMRI subjects and were secured with foam padding and a bite bar to reduce motion. Therefore we do not expect motion to be a significant contributor to these TSNR differences. Likewise any scanner instabilities are relatively small and should not cause such pronounced differences between predicted and measured TSNR. Physiological noise, however, is a dominant source of signal fluctuations at high field, and its effects have been shown to increase at larger voxel sizes (Kruger and Glover, 2001; Triantafyllou et al., 2005; Triantafyllou et al., 2006). Though we expect the shorter echo trains of our 3D sequences should make them resistant to bulk physiological noise effects such as image shifting due to changes in magnetic susceptibility (Raj et al., 2001), it is possible that signal changes introduced through respiratory modulation of the magnetic field may have a significant impact on the TSNR of the low resolution 3D-PRESTO sequences (Murphy et al., 2007). One future direction for this work could be an investigation of the relative contributions of respiratory power to the temporal power spectra of these

sequences. It has recently been suggested that RF spoiling in multi-shot 3D gradient echo sequences can significantly reduce temporal signal fluctuations, yielding temporal signal stability on par with 2D-EPI (Goerke et al., 2008).

Despite the differences in TSNR and F-statistics, 3D-FFE, 3D-PRESTO and 2D-EPI all produced qualitatively similar polar angle retinotopy maps that accord well with previously published reports. As seen in Figures 5.9-5.12, our 1.12 x 1.12 x 1.12mm^3 retinotopic maps clearly show visual areas V1, V2, V3, and parts of V3A and hV4, while the larger field of view associated with 1.67 x 1.67 x 1.67mm^3, 2 x 2 x 2mm^3 and 3 x 3 x 3mm^3 maps revealed V1, V2, V3, and all of V3A, hV4, LO1/2, and V7 (IPS0). (Engel et al., 1994; Sereno et al., 1995; DeYoe et al., 1996; Wandell et al., 2005; Wandell et al., 2007; Hoffman et al., 2009).

Given that the functional performance of 2D-EPI and the 3D sequences investigated here is comparable and all sequences produce reasonable retinotopic maps at all resolutions, image distortion and blurring (though the latter is more difficult to quantify) becomes critical deciding factors in which sequence is preferable for a given fMRI application. Hoffmann et al. (2009) reported distortion in their 7T EPI retinotopy maps even after applying distortion correction routines. Consistent with the observations of Hoffmann et al. and with measured values of each sequence's phase-encoding bandwidth (Figures 5.5a and b), our 3D sequences exhibit significantly less distortion than 2D-EPI at all resolutions. The distortion in 2D-EPI was worse at higher resolutions due to longer read-out

times associated with smaller voxels. This result raises concerns about the utility of single-shot, multi-slice 2D-EPI to high resolution retinotopic mapping at 7T.

Parallel imaging reduces distortion and other off-resonance effects by shortening echo train lengths (De Zwart et al., 2006; Weiger et al., 2002; Golay et al., 2000). However,the use of SENSE acceleration to reduce distortion in high resolution 2D-EPI sequences is limited for a number of reasons. First, larger distortions require larger SENSE factors to overcome, and SENSE-related noise can severely impact the already low SNR associated with small voxels. Second, 2D-EPI sequences only have one phase encoding direction, limiting acceleration options.As seen in chapter III, in-plane acceleration factors beyond R = 4 produced large geometry factors. Therefore R = 4 likely represents an upper limit on practical single-dimensional acceleration with our current coil configuration. This is consistent with predictions from Wiesinger et al. (2004) that R = 4 is a critical transition point for single-direction acceleration.

On the other hand, the shorter echo trains of multi-shot techniques like 3D-FFE and 3D-PRESTO mean they are inherently less sensitive to off-resonance effects than 2D-EPI. Multi-shot sequences also acquire data within a shorter window of T2* weighting, which helps reduce blurring compared to 2D-EPI and may account, in part, for the appearance that activation is more strictly confined to gray matter in these sequences (Liu et al., 1993; van Gelderen et al., 1995; Golay et al., 2000). In addition, SENSE acceleration may be applied to 3D scans in two directions because they make use of two phase encoding directions. Because the second phase encoding direction is analogous to the

slice-select direction in 2-D imaging, reducing the amount of data acquired in that direction can actually reduce the total time necessary to acquire the imaging volume, and thereby shorten the total scan time (Weiger et al., 2002). Shorter scan times tend to reduce the severity of motion artifacts as well.

A secondary benefit of having two phase encoding directions, as suggested by Weiger et al. (2002) and confirmed in chapter IV, is that larger total acceleration factors can be achieved with significantly smaller geometry factors than would result if the same amount of acceleration were applied in just one direction.

As shown in chapter IV, the amount of through-plane SENSE acceleration a 3D sequence can apply without incurring large g-factors strongly depends on the thickness of the imaging volume, the geometries of the coil array, and the object under examination. Specifically, narrow slabs (such as those covering only the occipital pole), should be conservative in the amount of through-plane acceleration applied because the imaging volume may have access only to a subset of coil sensitivity profiles. Applying through-plane acceleration under these conditions will quickly result in high geometry factors.

An alternate use for two-dimensional SENSE acceleration which both avoids this issue and has potential benefits for retinotopic mapping studies which aim to study many visual areas simultaneously is the ability to extend the image volume through SENSE acceleration. A larger imaging volume benefits from access to more receive coil sensitivity profiles because a larger portion of the space within the SENSE coil array is sampled during acquisition, resulting in

lower total geometry factors than in a smaller imaging volume in which the same amount of acceleration is applied in order to reduce scan time (Weiger et al., 2002). Finally, because 3D acquisitions average signal over the entire imaging volume, using SENSE to extend the imaging volume provides additional SNR from signal averaging to offset the SNR penalty due to under-sampling (Weiger et al., 2002). The performance of all SENSE applications will improve as coil arrays with more receive elements become available.

Finally, a potential alternative to the sequences presented here is EVI (echo volumar imaging, also known as 3D-EPI). Just as 2D-EPI acquires an entire slice following one excitation, 3D-EPI aims to acquire an entire 3D volume following one excitation (Mansfield et al., 1994). In theory, 3D-EPI would marry the temporal signal stability and temporal resolution of 2D-EPI with the improved SNR and other benefits inherent to 3D imaging. As with 2D-EPI, the major limiting factor of 3D-EPI at high field is magnetic susceptibility effects and T2*-related limitations on readout length. Since the data acquisition window will be N_z (the number of slice encodes) times longer in 3D-EPI compared to 2D-EPI, susceptibility effects could be N_z times worse as well. As coil arrays improve, high 2D acceleration factors may make 3D-EPI an appealing choice for high resolution, high field fMRI (Van der Zwaag et al., 2006).

6. Conclusions

We have compared the performance of 2D single-shot, multi-slice EPI, 3D-FFE and 3D-PRESTO in a polar angle retinotopic mapping experiment at four resolutions at 7T. In each sequence, and at each resolution, we observed robust brain activation and qualitatively similar retinotopic maps which were in agreement with existing literature (Engel et al., 1994; Sereno et al., 1995; DeYoe et al., 1996; Wandell et al., 2007). While BOLD sensitivity was generally comparable across resolutions, retinotopic maps associated with our 3D sequences consistently showed less distortion and clearer relationships between activated voxels and underlying anatomy than corresponding 2D-EPI maps.

Though echo planar imaging has some theoretical advantages, there are problems with the use of single-shot, multi-slice 2D-EPI at 7T. Distortion and blurring are particular concerns for high resolution functional mapping. By contrast, multi-shot 3D sequences such as 3D-FFE and 3D-PRESTO reduce distortion and blurring, enjoy SNR benefits at high resolutions due to volume signal-averaging and can apply two-dimensional SENSE acceleration to reduce off-resonance effects, to shorten total scan time, or extend the imaging volume. 3D-PRESTO in particular shows high SNR efficiency owing to time savings related to the echo shifting technique.

Although 2D-EPI shows higher TSNR than 3D-FFE and 3D-PRESTO for larger voxels, the differences in TSNR only partially explain the measured F-statistics. Instead, the number of images acquired per run and short TR times may as described by the efficiency η account for the higher F-statistics in 3D-

PRESTO compared to 2D-EPI at low resolutions. In this regard the ability of 3D sequences to reduce scan time with SENSE and acquire more images within a fixed period becomes even more relevant.

We conclude that both 3D-FFE and 3D-PRESTO provide comparable fMRI sensitivity to 2D-EPI at each resolution tested here, and that these 3D sequences generate images that are significantly less distorted and blurry than corresponding 2D-EPI scans. 3D-PRESTO achieves significantly higher F-statistics and temporal resolution than 2D-EPI due to increased efficiency at resolutions of 2 x 2 x 2mm^3 and below. These findings, coupled with increased parallel imaging flexibility from two phase encoding directions, suggest high resolution 3D imaging sequences may be well suited for retinotopic mapping and other functional MRI experiments at high field.

CHAPTER VI

SUMMARY & OUTLOOK

The technology and methods of magnetic resonance imaging are rapidly evolving. The three major topics discussed in this dissertation, functional MRI, high field human imaging, and parallel imaging, have been introduced only within the past 20 years. The last decade in particular has shown significant increases in the adoption of high field scanners and multi-channel receiver coils.

While high magnetic fields provide theoretical benefits in SNR and BOLD contrast, they also introduce technical issues such as increased bulk magnetic susceptibility effects and increased physiological noise. Parallel imaging can alleviate some of these issues, but does so at a cost to SNR that depends on the degree of reduction and the local geometry factor *g*, which is unique to given experimental circumstances. This work has attempted to address some of the issues surrounding high field fMRI, particularly in the context of parallel imaging.

Chapter III aimed to describe the interactions between SENSE acceleration factor R, physiological noise, temporal signal stability, and BOLD sensitivity in a simple fMRI task with high resolution (1 x 1 x 2mm^3) 2D-EPI. This chapter showed that the absolute contribution of physiological noise is independent of R under these conditions. At R < 5, physiological noise dominated the temporal variance in the time series, while at R >= 5 noise related to *g* and R dominated both spatial and temporal variance.

In general, physiological noise was found to contribute 3-5 times the temporal variance of thermal noise, depending on the individual and location in the brain. Though SENSE does not reduce the absolute contribution of physiological noise to an fMRI time series, SENSE can increase resolution and thereby reduce physiological noise along with voxel volume.

We conclude from chapter III that the acceleration factor R acts as an additional degree of freedom in obtaining an optimal tradeoff between acquisition time, image distortion, coverage, resolution, and physiological noise for a given fMRI application. For this experiment, R = 4 represented the optimum compromise between TSNR, BOLD sensitivity, noise enhancement, and geometric distortion.

Given the importance of parallel imaging to obtaining fMRI images with acceptable image quality at high field, and that the geometry factor *g* is a prime source of noise enhancement in SENSE data, chapter IV provided a series of experiments which characterized the geometry factor distribution under a variety of scan conditions. Using this information, this chapter aimed to determine optimal scan parameters for both fast, full-brain 3D-PRESTO scans, as well as a set of 2D-EPI, 3D-FFE, and 3D-PRESTO scans for retinotopic mapping with a limited field of view at several resolutions.

The first and second experiments showed that even small amounts of acceleration can cause unacceptably high geometry factors when applied along a narrow dimension of the field of view, and/or along an unfavorable direction relative to the coil elements. In particular, acceleration in the head-foot direction

should be avoided with our 16 channel coil if possible. The second experiment also introduced a method for simulating geometry factor volumes which may expedite selection of optimal R values for 3D imaging sequences with acceleration in two dimensions.

The third experiment introduced a number of promising 3D-PRESTO scans for fast, full brain fMRI with low geometry factors and high TSNR. In particular, the Axial 2 x 2 x 2mm^3 isotropic scan with 2s dynamic scan time performed well in tests and in the retinotopic mapping experiment in chapter V. This scan had particularly low geometry factors, so the spatial and/or temporal resolution could likely be further improved through increased acceleration without significant loss in BOLD sensitivity. Sagittal 3D-PRESTO scans also performed well, owing to alignment of the phase encoding directions with the array elements. One sagittal 3.5 x 3.5 x 3.5mm^3 3D-PRESTO acquisition with dynamic scan time 0.6s attained total acceleration of $R > 13$ while maintaining remarkably low geometry factors and high TSNR.

The fourth experiment showed that, for a given field of view, the geometry factor does not depend on the number of slices or slice thickness in a significant way. Though not especially surprising, knowing that changing the slice thickness (which may be useful to increase SNR at high resolutions) or the number of slices for a fixed field of view will not require g to be measured again could offer some time savings during the optimization process.

The fifth experiment showed that the highest value of in-plane acceleration that would maintain $g < 2$ throughout the imaging volume in a 1 x 1 x 1mm^3 axial

2D-EPI scan was R = 2.6, but that significantly higher R values were achievable if some areas of $g > 2$ were tolerable. Similar acquisitions from chapter III suggest that R = 4 is a reasonable cut-off point to maintain $g < 2$ throughout the majority of the volume, with an area of potentially higher *g* in the center. So long as areas of high *g* do not coincide with areas of functional interest, there should be little relevant penalty to TSNR or BOLD sensitivity when hotspots occur elsewhere in the imaging volume.

The sixth experiment provided preliminary tests for ten retinotopic mapping sequences (one each of 2D-EPI and a corresponding 3D scan at 1 x 1 x $1mm^3$, 1.12 x 1.12 x $1.12mm^3$, 1.67 x 1.67 x $1.67mm^3$, 2 x 2 x $2mm^3$, 3 x 3 x $3mm^3$) which had been developed based on previous findings. Except for the 1 x 1 x $1mm^3$ scans, which had geometry factors close to 2 and relatively low TSNR, the eight remaining sequences performed well in preliminary tests and were successfully applied to a retinotopic mapping task in chapter V.

In agreement with findings from Chapter, III, the sixth experiment of Chapter IV showed TSNR reduced by 3-5 times in humans compared to phantoms (due to physiological noise) across sequences and resolutions. This chapter also discussed the possibility of using SENSE to increase the imaging volume, or to increase SNR efficiency by increasing TR in the short TR regime (as in 3D-FFE and 3D-PRESTO).

Though Weiger et al. (2002) have suggested that distributing the total acceleration factor across both phase encoding directions may serve to reduce the geometry factor at a given degree of acceleration, this approach can also

cause large geometry factors if acceleration directions are not chosen carefully with respect to the field of view and receive coil elements. The findings from this chapter emphasize the importance of preliminary studies to verify that *g* and TSNR are within acceptable levels prior to fMRI data acquisition, especially in limited field of view and/or 3D acquisitions with 2D acceleration.

One current need is a fast and efficient way to monitor geometry factor data on the scanner console. At present, geometry factor maps must be acquired, reconstructed, and exported separately from other data. This process is time consuming, and with many scan slots already pressed for time, some may be deterred from taking these important steps.

Chapter V compared the performance of 2D-EPI, 3D-FFE and 3D-PRESTO in a polar angle retinotopic mapping experiment at 1.12 x 1.12 x 1.12mm^3, 1.67 x 1.67 x 1.67mm^3, 2 x 2 x 2mm^3, and 3 x 3 x 3mm^3 at 7T. Each sequence produced robust activation maps at each resolution, but the 3D sequences showed significantly less distortion, blurring, and signal loss compared to 2D-EPI, especially at higher resolutions. Distortion and blurring in particular are critically limiting factors for high resolution fMRI with single-shot 2D-EPI, so reduced sensitivity to these effects is a significant advantage for multi-shot 3D imaging at high field.

At 1.12 x 1.12 x 1.12mm^3 and 1.67 x 1.67 x 1.67mm^3, 2D-EPI and 3D-FFE showed comparable BOLD sensitivity, with 2D-EPI having slightly higher F-statistics and significantly higher TSNR. At 2 x 2 x 2mm^3 and 3 x 3 x 3mm^3, 3D-PRESTO showed higher F-statistics than 2D-EPI despite having lower TSNR.

This difference most likely owes to a combination of (a) more observations within the fixed scan period (288s), (b) short TRs as suggested by Constable and Spencer (2001), and (c) SNR efficiency gains due to echo shifting. These findings, coupled with capabilities of 3D sequences to apply parallel imaging in both phase encoding directions, suggests that multi-shot 3D gradient echo sequences generally perform either on par with or better than 2D-EPI for many 7T fMRI applications while also providing significantly reduced magnetic susceptibility effects.

Importantly, there were areas of brain activity detected with 2D-EPI that were not detected with 3D-FFE and 3D-PRESTO in these studies. On the contrary, the 3D activation maps appeared smoother and more precisely localized to underlying gray matter than the corresponding 2D-EPI maps. Therefore the slightly higher F-statistics observed in 2D-EPI at high resolutions may be readily traded for the reduced magnetic susceptibility effects and greater parallel imaging flexibility in 3D-FFE without significant loss in functional brain information.

The role of parallel imaging in fMRI is expected to increase with field strength. The most effective way to improve parallel imaging performance at a given field strength is to increase the number of receiver coils in the array. This increases the baseline SNR, which can be used to acquire images at higher spatial or temporal resolutions or to further reduce MSE through shorter acquisition times. In general, adding more coils is always beneficial; however, as coil elements and individual sensitivity profiles become smaller, coil calibration

and coil array geometry become more relevant and will require extra attention. Finally, parallel imaging generates large amounts of data and requires significant computational resources for image reconstruction, so infrastructure must grow along with array size (Pruessmann et al., 2006).

Proposed Method for Optimizing Parallel fMRI Sequences at High Field

Based on the preceding results and discussion, we propose the following process for optimizing accelerated fMRI acquisitions at high field:

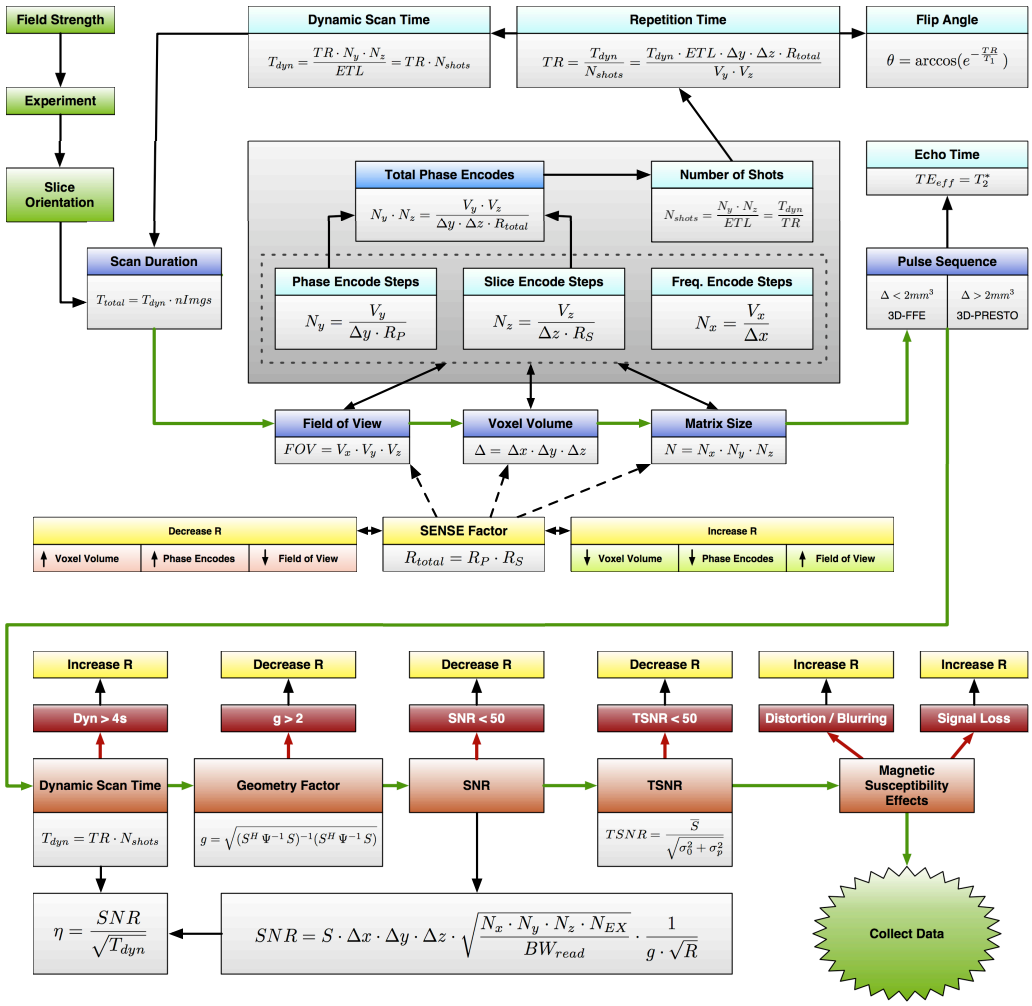

Figure 6.1: Process for optimizing accelerated fMRI acquisitions at 7T.

I. Determine a field of view and slice orientation based on experimental goals. If full brain coverage is required or if the experiment allows, consider using sagittal orientation to take full advantage of the 16 channel headcoil. 3D data with isotropic voxel sizes can be re-sliced into other orientations.

II. Choose a starting resolution. High resolutions create more precise maps of brain structure and function, reduce partial volume effects and reduce physiological noise. As a starting point, consider a voxel volume at which the contributions of physiological and thermal noise are equal (Bodurka et al., 2007).

Isotropic voxel dimensions should be chosen if possible, though increasing the voxel size in the slice (slab) direction is one option for improving SNR. According to the findings in chapter IV and V, voxel volumes of 1 x 1 x 1mm^3 or smaller may not reliably produce robust fMRI data under current conditions. However we have demonstrated robust activation at both 1 x 1 x 2mm^3 (chapter III) and 1.12 x 1.12 x 1.12mm^3 (chapter V) with both 2D-EPI and 3D-FFE.

III. Choose a pulse sequence. If voxels < 2 x 2 x 2mm^3 are required for a high resolution, limited field of view application, choose 3D-FFE to minimize magnetic susceptibility effects while retaining reasonable BOLD sensitivity. If high temporal resolution and/or full brain coverage with voxels > 2 x 2 x

$2mm^3$ is required, use 3D-PRESTO for high temporal resolution, high SNR efficiency, and relatively low sensitivity to bulk magnetic susceptibility effects.

IV. Choose TE ~ T_2^*. If using 3D-PRESTO, choose the shifted echo to be ~ T_2^*. Typically TE ~ 22ms at 7T.

V. Choose an initial value for SENSE acceleration. Based on existing literature and on our findings, axial and coronal scans may safely begin with in-plane acceleration of R_P = 2.5 for a standard ~200 mm FOV in the in-plane phase encoding direction. SENSE factors will likely change as the optimization process continues. If a 3D acquisition is chosen in axial or coronal slice orientation, set through-plane acceleration R_S = 1 initially. Depending on other parameters, R_S may be increased later.

   At this point it may be worthwhile simulating geometry factor volumes for a variety of acceleration factor combinations as suggested in chapter IV.

VI. Choose TR to be as short as possible. Short TRs increase statistical power by allowing more observations in a fixed imaging time (typically about 5 minutes), and improve fMRI sensitivity (Constable and Spencer, 2001). High temporal resolution also improves the sampling rate of physiological processes which can improve the quality of correction techniques.

VII. Choose the flip angle (FA) based on the Ernst angle at the specified TR.

VIII. Check the dynamic scan time. Dynamic scan times longer than 4 seconds should be avoided for fMRI, while those shorter than 2 seconds are preferred. If the dynamic scan time is too long, increase R to reduce acquisition time. If necessary, reduce the number of slices in 2D-EPI. In 3D imaging, reducing the number of phase encoding steps will automatically reduce the scan time. Alternatively, reduce the voxel volume to shorten scan time, then return to step 2. If dynamic scan time is acceptable, proceed.

IX. Check the geometry factor distribution. If $g > 2$ in areas of functional interest, reduce the SENSE acceleration factor and then return to step 2.

If using a 3D acquisition with a large field of view in both phase encoding directions, apply SENSE acceleration symmetrically. Since the geometry factor tends to increase more sharply as acceleration in single direction increases, symmetric increase of R in both phase encoding directions should minimize *g* assuming the field of view is sufficiently large. For limited field of view, high resolution imaging, symmetric acceleration will not be possible because through-plane acceleration should be kept to a minimum. If $g < 2$ in areas of functional interest, proceed.

X. Check Image SNR. If image SNR < 50, either increase the voxel volume or reduce R to improve SNR.

XI. Check TSNR. If the median value of TSNR > 200 in a phantom, consider further increasing R to reduce acquisition time, increase spatial resolution, or increase coverage as desired, then return to step 2. If the median TSNR < 50 in a phantom, but *g* is within acceptable levels, consider increasing voxel volume or further decreasing R to increase TSNR, then return to step 2.

According to de Zwart et al. (2002), scans in which the SNR is significantly higher than the TSNR are prime candidates for further acceleration. If image SNR is high, but *g* and TSNR are low, physiological noise is probably limiting TSNR and increasing voxel volumes will not improve TSNR. On the other hand, if all of image SNR, *g*, and TSNR are low, then increasing voxel volumes may improve both SNR and TSNR while also shortening scan time.

Expect an average 4x reduction in TSNR from phantoms to humans due to physiological noise. If TSNR acceptable, proceed.

XII. Check distortion, blurring, and signal dropout. If necessary, and if TSNR is high enough, increase R to reduce these magnetic susceptibility effects, then return to step 2. If TSNR is not high enough to increase R, consider

increasing the voxel volume to increase TSNR and shorten readout times (thereby also shortening MSE).

XIII. If dynamic scan time, *g*, SNR, TSNR and MSE are acceptable, proceed with fMRI data collection.

Though this procedure is not exhaustive and may not apply in every situation, it represents a systematic method for choosing parameters which are likely to provide good performance for most fMRI experiments using parallel imaging. These steps are a starting point from which we hope to build a more complete optimization framework.

Next Steps

In light of the work presented here, we suggest the following next steps:

- Obtain a coil array with 32 or more carefully arranged receive elements.
- Use the new coil to conduct fMRI studies at 1 x 1 x 1mm^3 or higher with 2D-EPI and 3D-FFE.
- Use the new coil to achieve a 1.5 x 1.5 x 1.5mm^3 3D-PRESTO protocol with high temporal resolution, short TR, full brain coverage, and low sensitivity to bulk MSE.
- Continue to improve methods for simulating and/or monitoring geometry factor volumes as a tool for further expediting the optimization process.

The ultimate aim of improving MRI hardware is to achieve more precise understanding of the structure and function of the human brain. Scanners with higher magnetic field strengths provide increased signal and contrast, but these "raw materials" do not automatically translate into more useful images. Methods must also improve to realize the theoretical benefits of improved hardware. In this work we have attempted to address a number of issues related to the acquisition of functional MRI data at high field strengths, particularly in the context of parallel imaging. We hope our work will contribute to the improvement of future experiments.

REFERENCES

Bandettini P.A., Wong E.C., Hinks R.S., Tikofsky R.S., Hyde J.S. (1992) Time course EPI of human brain function during task activation. *Magn Reson Med*, **25**, 390-398.

Bandettini P.A. (2007) Functional MRI today. *Int J Physchophys*, **63**(2), 138-145.

Bernstein MA, King KF, Zhou XJ. (2004) Handbook of MRI Pulse Sequences., Elsevier Academic Press, Burlington, MA.

Bloch F, Hansen WW, Packard ME. (1946) Nuclear induction. *Phys Rev*, **69**, 127.

Bloch F, Hansen WW, Packard ME. (1946) The nuclear induction experiment. *Phys Rev*, **70**, 474-485.

Bodurka, J., Ye, F., Petridou, N., Murphy, K. (2007) Mapping the MRI voxel volume in which thermal noise matches physiological noise—Implications for fMRI. *NeuroImage*,**34**, 542-549.

Cheng K, Waggoner RA, Tanaka K. (2001) Human ocular dominance columns as revealed by high-field functional magnetic resonance imaging. *Neuron*, **32**, 359-374.

Constable R.T. and Spencer D.D. (2001) Repetition time in echo planar functional MRI. *Magn Reson Med*, **46**(4), 748-755.

Damadian R. (1971) Tumor detection by nuclear magnetic resonance. *Science*, **171**, 1151-1153.

De Panfilis, C., and Schwarzbauer, C. (2005) Positive or negative blips? The effect of phase encoding on susceptibility-induced signal losses in EPI. *NeuroImage,* **25**, 112-121.

DeYoe EA, Carman GJ, Bandettini P, Glickman S, Wieser J, Cox R, Miller D, Neitz J. (1996) Mapping striate and extrastriate visual areas in human cerebral cortex. *Proc Natl Acad Sci U.S.A.*, **93(6)**, 2382-2386.

De Zwart JA, Ledden PJ, van Gelderen P, Bodurka J, Chu R, Duyn JH. (2004) Signal-to-noise ratio and parallel imaging performance of a 16-channel receive-only brain coil array at 3.0 Tesla. *Magn Reson Med,* **51(1)**, 22-26.

De Zwart JA, Van Gelderen P, Fukunaga M, Duyn JH. (2008) Reducing correlated noise in fMRI data. *Magn Reson Med*, **59**, 939-945.

De Zwart JA, Van Gelderen P, Golay X, Ikonomidou VN, Duyn JH. (2006) Accelerated parallel imaging for functional imaging of the human brain. *NMR Biomed,* **19(3)**, 342-351.

De Zwart JA, Van Gelderen P, Kellman P, Duyn JH. (2002) Application of sensitivity-encoded echo-planar imaging for blood oxygen level-dependent functional brain imaging. *Magn Reson Med*, **48(6)**, 1011-1020.

Dougherty RF, Koch VM, Brewer AA, Fischer B, Modersitzki J, Wandell BA (2003) Visual field representations and locations of visual areas V1/2/3 in human visual cortex. *J Vis,* **3**, 586-598.

Duong TQ, Yacoub E, Adriany G, Hu X, Ugurbil K, Kim SG. (2003) Microvascular BOLD contribution at 4 and 7T in the human brain: gradient-echo and spin-echo fMRI with suppression of blood effects. *Magn Reson Med*, **49**, 1019-1027.

Engel SA, Rumelhart DE, Wandell BA, Lee AT, Glover GH, Chichilnisky EJ, Shadlen MN. (1994) fMRI of human visual cortex. *Nature*, **369(6481)**, 525.

Engel SA, Glover GH, Wandell BA. (1997) Retinotopic organization in human visual cortex and the spatial precision of functional MRI. *Cereb Cortex*, **7(2)**, 181-192.

Edelstein W.A., Glover G.H., Hardy C.J., Redington R.W. (1986) The intrinsic signal-to-noise ratio in NMR imaging. *Magn Reson Med*, **3**, 604-618.

Ernst RR, Anderson WA. (1966) Application of Fourier transform spectroscopy to magnetic resonance. *Rev Sri Instr*, **37**, 93-102.

Friston KJ, P. J, R. T. (1994) Analysis of functional MRI time-series. *Hum Brain Mapp,* **1(2)**, 153-171.

Friston KJ, Holmes AP, Worsley KJ, Poline JP, Frith CD, Frackowiak RSJ. (1994) Statistical parametric maps in functional imaging: A general linear approach. *Hum Brain Mapp,* **2(4)**, 189-210.

Friston KJ, Holmes AP, Poline JB, Grasby PJ, Williams SC, Frackowiak RS, Turner R. (1995) Analysis of fMRI time-series revisited. *NeuroImage,* **2(1)**, 45-53.

Friston KJ, Frith CD, Turner R, Frackowiak RS. (1995) Characterizing evoked hemodynamics with fMRI. *NeuroImage,* **2(2)**, 157-65.

Friston KJ, Williams S, Howard R, Frackowiak RS, Turner R. (1996) Movement-related effects in fMRI time-series. *Magn Reson Med,* **35(3)**, 346-55.

Friston KJ, Josephs O, Rees G, Turner R. (1998) Nonlinear event-related responses in fMRI. *Magn Reson Med*, **39(1)**, 41-52.

Garroway AN, Grannell PK, Mansfield P. (1974) Image formation in NMR by a selective irradiation process. *J Phys C Solid State Phys*, **7**, L457-L462.

Glover, G.H., Li, T.Q., Ress, D. (2000) Image-based method for retrospective correction of physiological motion effects in fMRI: RETROICOR. *Magn Reson Med*, **44**, 163-167.

Goerke U., Moller H.E., Norris D.G., Schwarzbauer C. (2005) A comparison of signal instability in 2D and 3D EPI resting-state fMRI. *NMR Biomed*, **18**, 534-542.

Golay X, Pruessmann KP, Weiger M, Crelier GR, Folkers PJ, Kollias SS, Boesiger P. (2000) PRESTO-SENSE: an ultrafast whole-brain fMRI technique. *Magn Reson Med,* **43(6)**, 779-786.

Gerlach W, Stern O. (1924) On the position of the quantum lines in a magnetic field. Ann Phys, **74**, 675-699.

Haacke EM, Brown RW, Thompson MR, Venkatesan R. (1999) Magnetic Resonance Imaging: Physical Principles and Sequence Design. John Wiley and Sons, Inc., New York.

Hansen KA, Kay KN, Gallant JL. (2007) Topographic organization in and near human visual area V4. *J Neurosci*, **27**, 11896-11911.

Hoffmann MB, Stadler J, Kanowski M, Speck O. (2009) Retinotopic mapping of the human visual cortex at a magnetic field strength of 7T. *Clin Neurophysiol* **120**, 108-116.

Hu, X., Le, T.H., Parish, T., Erhard, P. (1995) Retrospective estimation and correction of physiological fluctuation in Functional MRI. *Magn Reson Med*, **34**, 201-212.

Hyde, J.S., Biswal, B.B., Jesmanowicz, A. (2001) High-resolution fMRI using multislice partial k-space GR-EPI with cubic voxels. *Magn Reson Med,* **46**, 114-125.

Jenkinson M, Bannister P, Brady M, Smith S. (2002) Improved optimization for the robust and accurate linear registration and motion correction of brain images. *NeuroImage*, **17**, 825-41.

Jonsson T., Lindholm T., Vestman P., Kristofferson Wiberg M., Bodurka J., Li T-Q. (2009) B0 Dependence of physiological noise in BOLD fMRI. *Proc Intl Soc Mag Reson Med,* **17**, 1589.

Kim DS, Ronen I, Olman C, Kim SG, Ugurbil K, Toth LJ. (2004) Spatial relationship between neuronal activity and BOLD functional MRI. *NeuroImage*, **21**, 876-885.

Kirson D, Huk AC, Cormack LK. (2008) Quantifying spatial uncertainty of visual area boundaries in neuroimaging data. *J Vis*, **8**, 1-15.

Klarhofer M, Dilharreguy B, Van Gelderen P, Moonen CT. (2003) A PRESTO-SENSE sequence with alternating partial-Fourier encoding for rapid susceptibility-weighted 3D MRI time series. *Magn Reson Med*, **50(4)**, 830-838.

Konen CS, Kastner S. (2008) Representation of Eye Movements and Stimulus Motion in Topographically Organized Areas of Human Posterior Parietal Cortex. *J Neurosci*, **28**, 8361-8375.

Kruger, G., Kastrup A., Glover G.H. (2001) Neuroimaging at 1.5 T and 3.0 T: Comparison of oxygenation-sensitive magnetic resonance imaging. *Magn Reson Med*, **45**, 595-604.

Kruger, G., and Glover G.H. (2001) Physiological noise in oxidative-sensitive magnetic resonance imaging. *Magn Reson Med*, **46**, 631-637.

Kumar A, Welti D, Ernst RR. (1975) Imaging of macroscopic objects by NMR fourier zeugmatography. *Naturwissenschaften,* **62**, 34.

Larmor J. (1897) The influence of a magnetic field on radiation frequency. *Proc R Soc*,**60**, 514-515.

Larsson J, Heeger DJ. (2006) Two retinotopic visual areas in human lateral occipital cortex. *J Neurosci*, **26**, 13128-13142.

Lauterbur PC. (1973) Image formation by induced local interactions: examples employing nuclear magnetic resonance. *Nature*, **242**, 190-191.

Lauterbur PC. (1986) Cancer detection by nuclear magnetic resonance zeugmatographic imaging. *Cancer*, **57**, 1899-1904.

Liu G, Sobering G, Duyn J, Moonen CT. (1993) A functional MRI technique combining principles of echo-shifting with a train of observations (PRESTO). *Magn Reson Med*, **30(6)**, 764-768.

Lutcke H., Merboldt K., Frahm, J. (2006) The cost of parallel imaging in functional MRI of the brain. *Magn Reson Imag*, **24**, 1-5.

Mansfield P. and Grannell, P.K. (1973) NMR 'diffraction' in solids? *J Phys C Solid State Phys,* **6**, L422-L426.

Mansfield P., Harvey P.R., Stehling M.K. (1994) Echo-volumar imaging. *Magma*, **2**, 291-294.

Moeller, S., Van de Moortele, P., Goerke, U., Adriany, G., Ugurbil, K. (2006) Application of parallel imaging to fMRI at 7 Tesla using a high 1D reduction factor. *Magn Reson Med,* **56**, 118-129.

Mourino, M. (2001) From Thales to Lauterbur, or from the lodestone to MR imaging: magnetism and medicine. *Radiology*, **180**, 593-612.

Murphy K., Bodurka J., Bandettini P.A. (2007) How long to scan? The relationship between fMRI temporal signal to noise ratio and necessary scan duration. *NeuroImage*, **34**, 565-574.

Neggers SFW, Hermans EJ, Ramsey NF. (2008) Enhanced sensitivity with fast three-dimensional blood-oxygen-level-dependent functional MRI: comparison of SENSE-PRESTO and 2D-EPI at 3T. *NMR Biomed,* **21**, 663-676.

Nitz WR. (2002) Fast and ultrafast non-echo-planar MR imaging techniques. *Eur Radiol,***12**, 2866-2882.

Ogawa S., Lee T-M., Nayak A.S., Glynn P. (1990) Oxygenation-sensitive contrast in magnetic resonance imaging of rodent brain at high magnetic fields. *Magn Reson Med*, **14**, 68-78.

Ogawa S., Menon R.S., Tank D.W., Kim S.G., Merkle H., Ellermann J.M., Ugurbil K. (1993) Functional brain mapping by blood oxygenation level-dependent contrast magnetic resonance imaging. A comparison of signal characteristics with a biophysical model. *Biophys J*, **64(3)**, 803-812.

Ohliger, M.A., Grant, A.K., Sodickson, D.K. (2003). Ultimate intrinsic signal-to-noise ratio for parallel MRI: electromagnetic field considerations. *Magn Reson Med*, **50**, 1018-1030.

Parrish T.B., Gitelman D.R., LaBar K.S., Mesulam M-M. (2000) Impact of signal-to-noise on functional MRI. *Magn Reson Med*, **44**, 925-932.

Preibisch, C., Pilatus, U., Bunke, J., Hoogenraad, F., Zanella, F., Lanfermann, H. (2003) Functional MRI using sensitivity-encoding echo planar imaging (SENSE-EPI). *NeuroImage,* **19**, 412-421.

Pruessmann, K.P. (2006) Encoding and reconstruction in parallel MRI. *NMR Biomed*, **19**, 288-299.

Pruessmann KP, Weiger M, Scheidegger MB, Boesiger P. (1999) SENSE: sensitivity encoding for fast MRI. *Magn Reson Med*, **42(5)**, 952-962.

Rabi II, Miliman S, Kusch P, ZachariasJR. (1939) The molecular beam resonance method for measuring nuclear magnetic moments. *Phys Rev*, **55**, 526-535.

Raemaekers M, Lankheet MJM, Moorman S, Kourtzi Z, van Wezel RJA. (2009) Directional anisotropy of motion responses in retinotopic cortex. *Hum Brain Mapp*, **00**:000-000 (E-publication).

Raj, D., Paley, D.P., Anderson, A.W., Kennan, R.P., Gore, J.C. (2000) A model for susceptibility artefacts from respiration in functional echo-planar magnetic resonance imaging. *Phys Med Biol*, **45**, 3809-3820.

Raj, D., Anderson, A.W., Gore, J.C. (2001) Respiratory effects in human functional magnetic resonance imaging due to bulk susceptibility changes. *Phys Med Biol*, **46**, 3331-3340.

Sereno MI, Dale AM, Reppas JB, Kwong KK, Belliveau JW, Brady TJ, Rosen BR, Tootell RB. (1995) Borders of multiple visual areas in humans revealed by functional magnetic resonance imaging. *Science*, **268(5212)**, 889-93.

Shmuel A, Yacoub E, Chaimow D, Logothetis NK, Ugurbil K. (2007) Spatio-temporal point-spread function of fMRI signal in human gray matter at 7 Tesla. *NeuroImage*, **35**, 539-552.

Silver MA, Kastner S. (2009) Topographic maps in human frontal and parietal cortex. *Trends Cogn Sci*, **13**, 488-495.

Swisher JD, Halko MA, Merabet LB, McMains SA, Somers DC. (2007) Visual topography of human intraparietal sulcus. *J Neurosci*, **27(20)**, 5326-5337.

Thulborn K, Waterton J, Matthews P, Radda G. (1986) Oxygenation dependence of the transverse relatation time of water protons in whole blood at high field. *Biochem. Biophys. Acta.* **714**, 265-270 (1982).

Tootell RB, Hadjikhani N, Hall EK, Marrett S, Vanduffel W, Vaughan JT, Dale AM. (1998) The retinotopy of visual spatial attention. *Neuron,* **21**, 1409-22.

Triantafyllou, C., Hoge, R.D., Krueger, G., Wiggins, C.J., Potthast, A., Wiggins, G.C., Wald, L.L. (2005) Comparison of physiological noise at 1.5T, 3T and 7T, and optimization of fMRI acquisition parameters. *NeuroImage*, **26**, 243-250.

Triantafyllou, C., Hoge, R.D., Wald, L.L. (2006) Effect of spatial smoothing on physiological noise in high-resolution fMRI. *NeuroImage,* **32**, 551-557.

Triantafyllou C., Elschot M., Polimeni J.R., Wald L. L. (2009) Physiological noise in GRAPPA fMRI time-series. *Proc Intl Soc Mag Reson* Med, **17**, 1584.

Van De Moortele PF, Pfeuffer J, Glover GH, Ugurbil K, Hu X. (2002) Respiration-induced B0 fluctuations and their spatial distribution in the human brain at 7 Tesla. *Magn Reson Med*, **47**, 888-895.

Van der Zwaag W., Francis S., Bowtell R. (2006) Improved echo volumar imaging (EVI) for functional MRI. *Magn Reson Med*, **56**, 1320-1327.

Vanni S, Dojat M, Warnking J, Delon-Martin C, Segebarth C, Bullier J. (2004) Timing of interactions across the visual field in the human cortex. *NeuroImage*, **21**, 818-828.

Vaughan, J.T., Garwood, M., Collins, C.M., Liu, W., DelaBarre, L., Adriany, G., Andersen, P., Merkle, H., Goebel, R., Smith, M.B., Ugurbil, K. (2001) 7T vs. 4T: RF power, homogeneity, and signal-to-noise comparison in head images. *Magn Reson Med*, **46**, 24-30.

Wandell BA, Brewer AA, Dougherty RF. (2005) Visual field map clusters in human cortex. *Philos Trans R Soc Lond B Biol Sci*, **360**, 693–707.

Wandell BA, Dumoulin SO, Brewer AA. (2007) Visual field maps in human cortex. *Neuron,* **56**, 366-383.

Warnking J, Dojat M, Guerin-Dugue A, Delon-Martin C, Olympieff S, Richard N, Chehikian A, Segebarth C. (2002) fMRI retinotopic mapping -- step by step. *NeuroImage,* **17**, 1665-1683.

Weiger, W., Boesiger, P., Hilfiker, P.R., Weishaupt, D., Pruessmann K.P. (2005) Sensitivity encoding as a means of enhancing the SNR efficiency in steady-state MRI. *Magn Reson Med*, **53**, 177-185.

Weiger M, Pruessmann KP, Boesiger P. (2002) 2D SENSE for faster 3D MRI. *Magma*,**14(1)**, 10-19.

Wiesinger, F., Van de Moortele, P., Adriany, G., De Zanche, N., Ugurbil, K., Pruessmann, K.P. (2006) Potential and feasibility of parallel MRI at high field. *NMR Biomed,* **19**, 368-378.

Wiesinger F., Boesiger P., Pruessmann, K.P. (2004) Electrodynamics and ultimate SNR in parallel MR imaging. *Magn Reson Med*, **52**, 376-390.

Wiesinger, F., Van de Moortele, P., Adriany, G., De Zanche, N., Ugurbil, K., Pruessmann, K.P. (2004) Parallel imaging performance as a function of field strength - An experimental investigation using electrodynamic scaling. *Magn Reson Med*, **52**, 953-964.

Wright P.J., et al. (2008) Water proton T1 measurements in brain tissue at 7, 3, and 1.5T using IR-EPI, IR-TSE, and MPRAGE: results and optimization. *Magma*, **21**, 121-30.

Yacoub E., Shmuel A., Pfeuffer J., Van De Moortele P.F., Adriany G., Anderson P., Vaughan J.T., Merkle H., Ugurbil K., Hu X. Imaging brain function in humans at 7 Tesla. *Magn Reson Med*, **45**, 588-594.

Yacoub E, Van De Moortele PFV, Shmuel A, Ugurbil K. (2005) Signal and noise characteristics of Hahn SE and GE BOLD fMRI at 7T in humans. *NeuroImage*, **24**, 738-750.